CHAPTER FOUR

Advanced Methods of Electron Microscopy in Catalysis Research

Miguel José-Yacamán[*], **Arturo Ponce**[*], **Sergio Mejía-Rosales**[†], **Francis Leonard Deepak**[‡]

[*]Department of Physics and Astronomy, University of Texas at San Antonio, One UTSA Circle, San Antonio, Texas 78249, USA.
[†]Center for Innovation and Research in Engineering and Technology, and CICFIM-Facultad de Ciencias Físico-Matemáticas, Universidad Autónoma de Nuevo León, San Nicolás de los Garza, NL 66450, México
[‡]The International Iberian Nanotechnology Laboratory, Av. Mestre José Veiga-4715-310, Braga, Portugal

Contents

1. Introduction 280
2. STEM and TEM 280
    2.1. The Principles of TEM and STEM Imaging 282
    2.2. HAADF-STEM 285
    2.3. Aberrations 287
    2.4. Practical Guide for STEM Imaging 291
3. Examples of Applications to Catalyst Characterization 294
    3.1. Metal Catalysts on a Crystalline Substrate 294
    3.2. Metals on a Noncrystalline Substrate 299
    3.3. Metals on γ-Al_2O_2 301
    3.4. Bimetallic Nanoparticles and Clusters 304
    3.5. Understanding the Structure of Bimetallic Nanoparticles and Clusters Using Advanced Electron Microscopic Techniques 305
    3.6. *In Situ* Heating Experiments of Bimetallic Nanoparticles and Clusters 316
    3.7. Multimetallic Systems 318
    3.8. Conclusions 318
4. Electron Microscopy of Layered Materials 319
    4.1. Introduction 319
    4.2. MoS_2 Nanowire Catalysts 320
    4.3. Co-Doped MoS_2/WS_2 Nanowire Catalysts 326
    4.4. MoS_2 Nanoplates 334
    4.5. Conclusions 337
Acknowledgments 338
References 338

Advances in Imaging and Electron Physics, Volume 177
ISSN 1076-5670,
http://dx.doi.org/10.1016/B978-0-12-407702-7.00004-8

© 2013 Elsevier Inc.
All rights reserved.

1. INTRODUCTION

The study of catalytic systems has been one of the most active areas of application of electron microscopy. Indeed, a typical catalyst is made of small particles—in the size interval of nanometers to even single atoms—and a substrate that is usually polycrystalline or, in a few cases, amorphous. The catalytic particles are made either of noble or transition metals, or oxides that strongly scatter electrons and therefore produce a high contrast in the micrograph.

Most of the commercially interesting supports are also oxides or semi-graphitic carbon, which also produce high contrast; therefore, the problem of the observation of a catalytic nanoparticle through an electron microscope is reduced to separate its contrast from that of the substrate. In a few important cases, the catalysts are not even nanoparticles but are *nanoribbons*, such as those made of MoS_2, that in principle are expected to behave as semiconductors.

2. STEM AND TEM

Conventional transmission electron microscopy (TEM) is a beam characterization technique with almost 80 years since the development of the first microscope. In TEM, a large area of the specimen is illuminated, the magnification is performed by the lens system underneath the specimen, and subsequently the whole image is registered instantaneously. Conventional scanning electron microscopy (SEM) was designed after the TEM and has been widely used for surface analyses in biological and materials sciences. Scanning transmission electron microscopy (STEM) combines both operational modes. In STEM mode, a convergent electron beam is focused to a small area of the sample. To register an image, the electron probe is raster-scanned and subsequently propagated through the sample. Due to the electron-matter interaction, the trajectory of the electrons is scattered and different kinds of signals are registered in sync with the electron probe scanning. STEM resolution is determined primarily by the size of the probe. One of the main advantages of STEM over TEM is that the images generated by the electrons scattered out to high angles on a high-angle annular dark-field (HAADF) detector are chemically sensitive, and a sample with a definite crystalline arrangement is not necessarily a requirement. The capacity of STEM to generate these different levels of contrast is commonly known as *Z-contrast*; the contrast dependence goes approximately as $Z^{\sim 2}$, with Z corresponding to the atomic weight of the element that caused the scattering of the electrons (Pennycook, 1989).

TEM and STEM operational modes are necessary for the study of nanoparticles. The appropriate generation and interpretation of electron micrographs is crucial for this purpose. The interpretation of the electron micrographs is not always straightforward because the intensity signal that correlates with the atomic positions depends not just on the length of the atomic columns parallel to the direction of the electron beam, but also on the chemical species and the microscope's parameters at which the micrograph was obtained. In this way, the problem of extracting a third dimension from the information contained in a strictly two-dimensional (2D) image requires the comparison of the observed images against simple models acquired by previous experience or inherited, and in many cases a theoretical model of the structure is necessary.

In TEM, the information transfer in phase-contrast imaging is determined by the objective lens and the size of its aperture, which are directly related to the temporal and spatial coherence of the electrons. In Figure 4.1, a conventional high-resolution transmission electron microscopy (HR-TEM) micrograph of a bimetallic nanoparticle 2 nm in diameter shows the interatomic distances; however, the contrast is not directly related with the different atomic positions in the bimetallic nanoparticle (Corthey *et al.*, 2010) proposed by the theoretical model shown in Figure 4.1b.

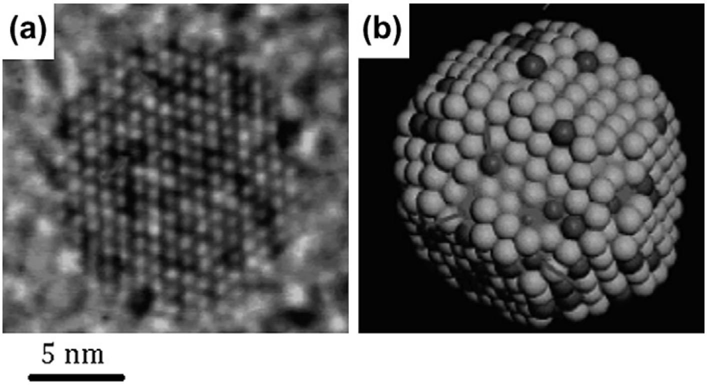

Figure 4.1 (a) HR-TEM image of a bimetallic gold-palladium nanoparticle. (b) Theoretical model of the bimetallic nanoparticle.

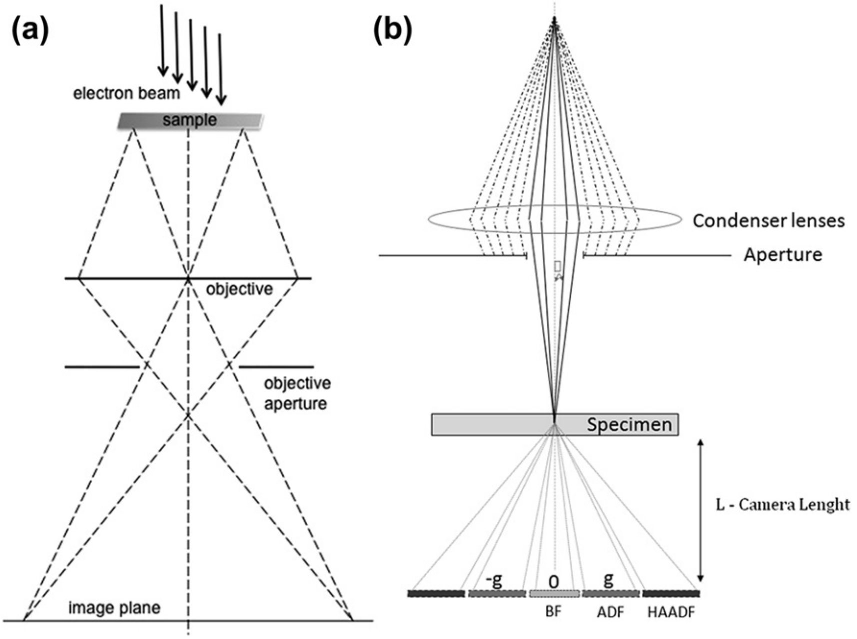
(a)
electron beam
sample
objective
objective aperture
image plane
(b)
Condenser lenses
Aperture
Specimen
L - Camera Lenght
-g
0
g
BF
ADF
HAADF

Figure 4.2 Simplified diagram of the (a) TEM and (b) STEM operational modes.

The optical arrangement of a conventional TEM compared with the STEM configuration is illustrated in the schematic diagram shown in Figure 4.2.

2.1. The Principles of TEM and STEM Imaging

Unlike macroscopic objects, whose structural properties can be inferred directly by investigating how a *beam of light* interacts with the object, the study of matter at the nanoscale requires investigating how a *beam of electrons* interacts with the sample, since wavelengths on the order of Ångstroms (or even smaller) are required to reach this level of resolution. This electron beam is produced by accelerating the electrons by applying a potential difference of several kilovolts to an emitter, usually a field emission cold cathode; other electron sources use thermionic emission to overcome the work function of the cathode. Originally, the beam is not monochromatic but an energy-selecting spectrometer can be added to the electron gun, at the price of diminishing the beam current. A first electrostatic lens called Wehnelt makes the beam reaching the anode more convergent (Rose, 1990). An aperture on the anode plate allows the beam to actually get into the microscope. A field emission gun (FEG) actually has two anodes: the first one in charge of producing the beam, the second one in charge of accelerating the electrons (Reimer and Kohl, 2008).

When the beam produced by the electron gun interacts with a sample, different signals are generated. Most of the electrons are transmitted through the sample with just a small deviation from the optic axis (the original trajectory of the electron beam); when collected, this signal is used to produce bright-field (BF) images. Signals transmitted at higher angles can be collected using an angular detector to produce dark-field (annular dark-field [ADF], HAADF) images or the energy of the electrons can be measured to generate electron energy-loss spectroscopy (EELS) maps. The chemical composition of the sample can be investigated by analyzing the X-rays generated when the electrons in the sample are excited by the beam—what is called *energy-dispersive X-ray* (EDX) spectroscopy. Auger electrons can be generated by a somewhat complex process: The beam causes the ejection of an inner-shell electron of the specimen; the formed vacancy is filled by an electron of a higher level and the excess energy liberates a third electron, called an Auger electron.

TEM is a powerful technique to characterize the structure and chemical composition of condensed matter. Conventional TEM (CTEM) includes basically three operation modes: diffraction contrast (BF and dark-field [DF]), phase-contrast (HR-TEM), and electron diffraction (ED). These three operating modes provide information about the crystalline structure in the materials, morphology, structural defects, and even chemical composition. Complementing CTEM, it is also possible to use STEM. Figure 4.2 shows the trajectory of the electrons in a TEM for both the TEM and STEM modes. Both modes are based on the interaction of an electron beam, generated by an electron gun at the top of the microscope, with the lenses and the specimen.

BF-CTEM is the simplest and most frequently used mode of operation of a TEM. In this mode, the images are formed by the direct (nondiffracted) electron beam, while an aperture blocks the diffracted beam. In these images, regions with no particles (and maybe just the carbon grid) appear as bright. DF images are generated by a detector that collects only the diffracted electrons. The regions with no particles appear dark—hence the name *dark field*. While in DF micrographs contrast is enhanced, BF images require a less-intense beam; thus this technique is less intrusive.

In high-resolution electron microscopy, the image can be considered the result of the interference of the transmitted and the diffracted beams after the interaction with the sample. Thus, the sample must be thin enough to transmit the electrons. When nanoparticles are being prepared for analysis by TEM or STEM, it is common to prepare the specimen by placing the nanoparticles on holey carbon copper grids. In some synthesis procedures, the nanoparticles are covered with a layer of organic ligands (Corthey *et al.*, 2010); if required, this organic layer can be removed by exposing the specimen to a beam shower for a few minutes before placing it in the microscope.

At the range of operating voltages of modern electron microscopes, the electron's momentum is very large—large enough that it is necessary to take into account relativistic corrections to describe correctly the interactions (Carter and Williams, 2009). The equation that considers the interaction of the electrons with the specimen and lenses requires some adjustments on the values of mass and wavelength. In a strict formalism, the equation that governs these interactions is the relativistic Dirac equation, but it is customary to use instead the approximated, easier-to-manipulate Schrödinger equation since the Dirac equation is very difficult to deal with, even in the simplest cases. In its most basic version, the role of the specimen is represented in the Schrödinger equation by its projected electrostatic potential. For sake of simplicity in this brief description, we can assume a periodicity condition in this potential (as if being produced by a periodic crystal). Let this potential be represented by $\Phi(r)$. The specific details of $\Phi(r)$ depend mainly on the chemical composition and structural features of the specimen, but a better description would also include thermal effects. The Schrödinger equation that describes the interaction of this potential with an electron of mass m and charge e coming from the source is

$$\left[-\frac{h^2}{8\pi^2 m}\nabla^2 - e\phi(r)\right]\Psi(r) = E\Psi(r),$$

and the wave function of the electron wave *before* interacting with the specimen can be described by using a simple plane wave:

$$\Psi_0(r) = \exp\{i(\omega t - 2\pi k_0 \cdot r)\}.$$

The solution to Eq. (1) describes the electron wave function *after* the interaction of the beam with the specimen. In practice, the task of finding a solution requires a set of approximations in addition to the periodicity assumption and the plane wave nature of the incoming beam, such as assuming that the specimen is not very thick.

The objective lens is positioned just after the sample in a TEM and it focuses the electron beam; the role of the objective lens can be described mathematically by the Fourier transform of the electron beam wave at the exit of the sample. Unlike the lenses used in visible light microscopes, both the objective and corrector lenses in the electron microscope are made of a magnetic field generated by an electric current circulating a coil, which affects the trajectory of the electron beam. In an ideal microscope with no aberrations, the image observed will be directly related to the squared modulus of the image-plane wave function (Reimer and Kohl, 2008). But in the real world, the objective lens is not perfect and introduces aberrations in the image-plane wave function. The most recent models of high-resolution microscopes include in their design additional coils that act as aberration correctors that make sub-Ångstrom resolution possible.

2.2. HAADF-STEM

From the standpoint of the electron beam, a STEM is an inverted TEM in the sense that the trajectory followed by the beam through the optical components of the STEM is the same as in the TEM but in the opposite direction. The reciprocity theorem states that the propagation of the beam is time reversible, and thus if in the TEM the detector is exchanged with the FEG, the system becomes basically a BF-STEM. A consequence of this equivalence is that, unlike with CTEM, the electron beam interacts with only a small section of the sample at a time (a pixel in the image), and so a scan process, made by deflecting the beam using a set of coils, must be used to generate the image of the entire specimen. The width of the beam (the *probe*) greatly determines the resolution of the STEM, and C_s correction is mandatory to obtain sub-Ångstrom resolution.

The scattered electrons in STEM mode can be registered by three different detectors. The BF detector collects the electrons transmitted in the path of the beam close to the optical axis, the BF electrons containing the total beam current. The annular dark-field (ADF) and the HAADF detectors are used to record the electrons scattered out of the path of the beam. In the STEM, the objective lens—and all the relevant optics—are positioned before the specimen. The scattered angle of the ADF detector is set around ~40 mrad and the outer angle is set around 60–200 mrad (see Figure 4.2). STEM differs from CTEM in that the electron beam interacts with only a small section of the sample; the scanning process is the one in charge of generating the image as a whole, whereas in TEM, a broad beam is interacting instantaneously with the sample. X-ray energy-dispersive spectroscopy (EDS) attached to the STEM mode provides an elemental analysis directly from the point or line raster-scanned in the sample. Therefore, the imaging using the BF or HAADF detectors in a complementary way can be matched to the EDS information, and the elemental mapping at atomic resolution is obtained. Figure 4.3 shows the setup of the STEM mode including the detectors previously mentioned. HAADF and BF images are indicated on the right side of Figure 4.3, and both can be acquired simultaneously. *L* corresponds to the camera length, which is the effective distance or magnification between the specimen and the detector plane position. The X-ray detector is included in Figure 4.3; the spectra can be collected at the same they are line scanned to register the STEM images.

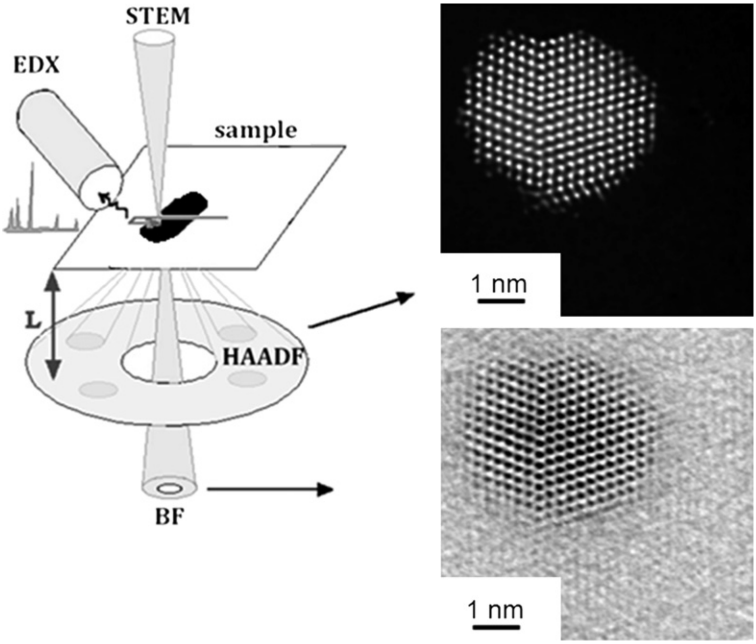

Figure 4.3 STEM setup, including the EDS spectrum detector. *L* corresponds to the camera length.

2.3. Aberrations

Aberrations are artifacts produced by the imperfections on the equipment. We have already described correction of chromatic aberration before the interaction of the electron beam with the specimen. Astigmatism and coma can be easily corrected using magnetic quadrupoles (Koch, 2002). Spherical aberrations, denoted C_s, are far harder to correct, but the corrections are necessary to produce images of atomic resolution. The objective lens, located behind the specimen in a TEM, focuses the electron beam, which mathematically can be described by the Fourier transform of the wave at the exit of the sample. Imperfections in the objective lens are the source of C_s, and additional optics is needed after this element to make the appropriate corrections.

The effect of C_s can be appropriately explained in terms of the contrast transfer function (CTF). In short, the CTF is used to determine how the different spatial frequencies will be represented in a TEM image. The electron wave function at the image plane will be related to the CTF applied to the wave function only at the exit of the sample. In a spatial frequency range where the CTF is approximately constant, the distances and sizes of objects will be represented directly on the micrograph, while in a range of spatial frequencies where the CTF varies greatly, it would be quite difficult to determine whether a bright spot in the micrograph corresponds to the presence or absence of an atom. Objective apertures, the spatial coherence of the electron beam, and its wavelength will affect the CTF. Its definition is

$$CTF(k) = -\sin\left[\frac{\pi}{2} C_s \lambda^3 k^4 + \pi \Delta z \lambda k^2\right].$$

Here, C_s is the spherical aberration of the objective lens and Δz is its defocus. A setting of particular interest is

$$\Delta z = -\sqrt{4/3 C_s \lambda}.$$

called the *Scherzer condition.* At the Scherzer defocus, the CTF does not change its sign in a large spatial frequency range; hence all distances in this range can be interpreted directly as they appear in the image (Reimer and Kohl, 2008; Carter and Williams, 2009).

Figure 4.4 shows the results of conventional HR-TEM simulations of a section of a gold lattice at different values of defocus, Scherzer included (–50 Å). The voltage was 200 kV in all cases, and a small aberration of

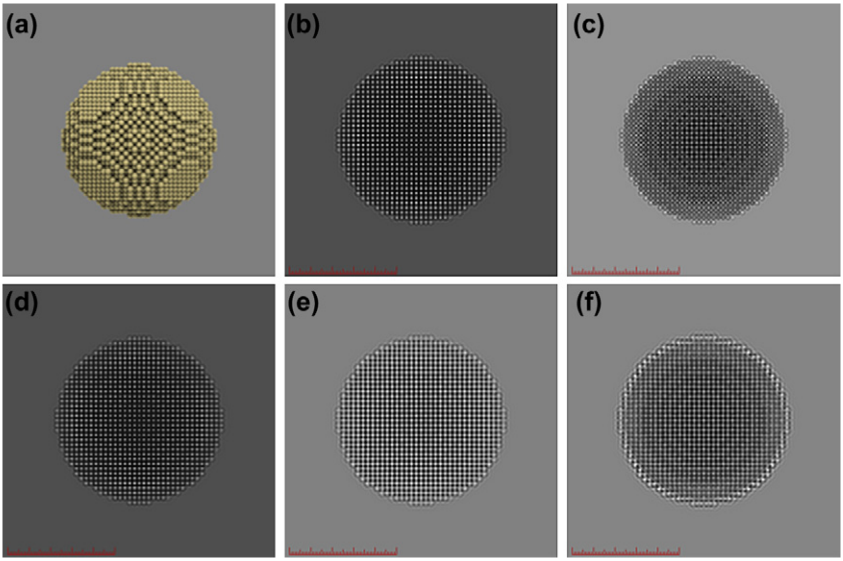

Figure 4.4 HR-TEM simulations of a spherical fcc gold nanostructure, calculated at different defocus values. (a) Model of the particle; (b) $\Delta z = -100\text{Å}$; (c) $\Delta z = -50\text{Å}$; (d) $\Delta z = 0\text{Å}$; (e) $\Delta z = 50\text{Å}$; (f) $\Delta z = 100\text{Å}$; The image labeled as (c) corresponds to the Scherzer defocus. (See the color plate).

0.01 mm was used with zero astigmatism. At Scherzer defocus, the atomic columns are completely resolved, even at the surface of the structure.

Aberration correction in TEM highly enhances the spatial resolution to such a degree that it is even possible to reach sub-Ångstrom level. The implementation of multipole corrector lenses in the electron optics system was developed in the 1990s, when the first correctors of the spherical and chromatic aberrations appeared. Probably the best way to acquire a sense of the neefor C_s correction to reach sub-Ångstrom resolution is by comparing micrographs obtained under the same conditions except for the spherical aberration. This is, of course, impossible to do in practice, but it is possible instead to compare the results of TEM simulations at different values of C_s. Figure 4.5 shows a comparison that illustrates this.

The Z-contrast technique works remarkably well in metal nanoparticles because the intensity dependence on atomic number is close to $Z^{3/2}$, with minimum dependence on microscope defocus (Wall, 1974). This is definitely different from what is expected of BF imaging, where the signal varies

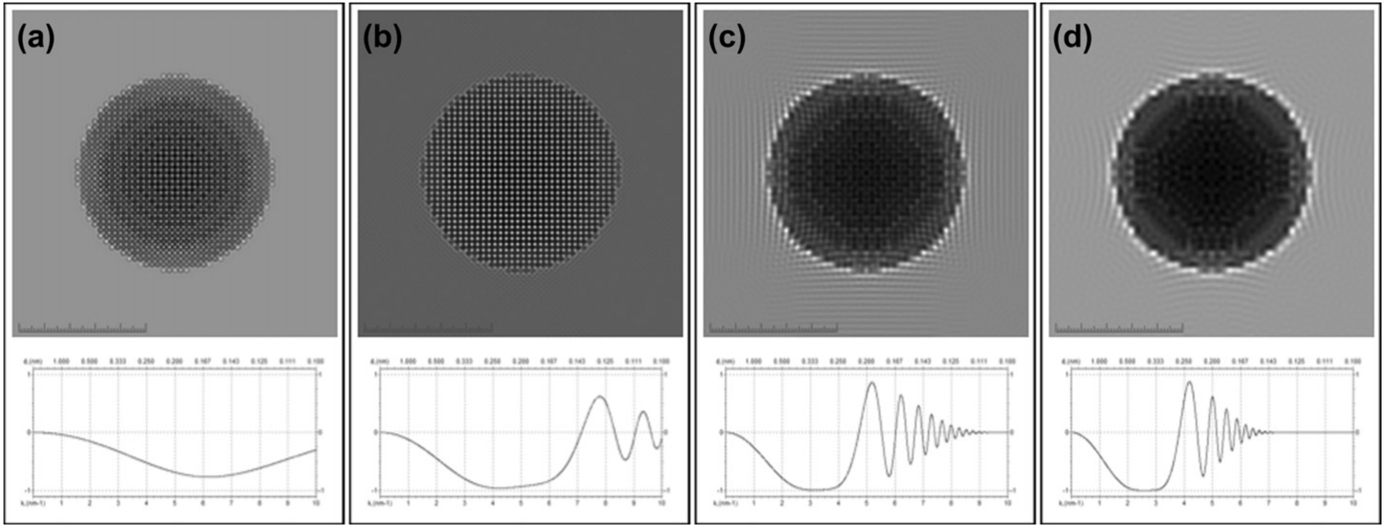

Figure 4.5 Simulated TEM micrographs calculated at several values of C_s and their corresponding contrast transfers functions. (a) 0.01 mm; (b) 0.1 mm; (c) 0.5 mm; (d) 1.2 mm.

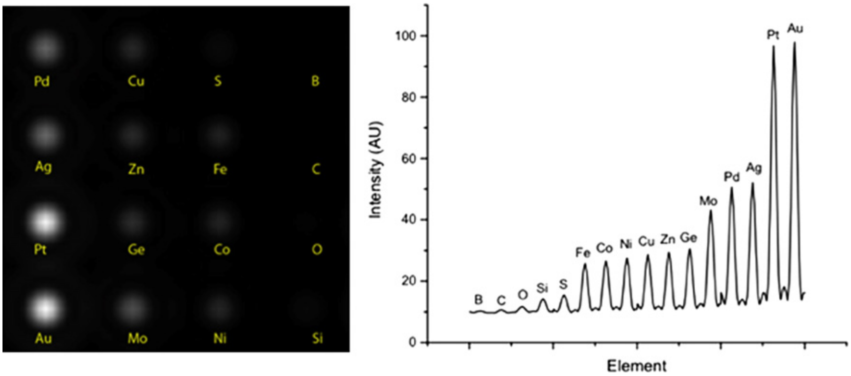

Figure 4.6 Profiles of intensity obtained from a series of HR-TEM simulated images (at a defocus of −41 nm). Note the intensity variation with the different elements. In each case, the columns of elements have the same number of atoms. (For color version of this figure, the reader is referred to the online version of this book).

weakly and nonmonotonically with Z. In HAADF-STEM, the differences among metals are evident. Figure 4.6 shows a Z-contrast STEM simulation of single atoms of different elements arranged in a 4 × 4 matrix. The line scan through the center of the atomic positions is shown at the right of the simulated image. The trend follows approximately a $Z^{1.46}$ relation, very close to the dependence expected by Pennycook and Boatner (Pennycook, 1998).

When used to image metal nanoparticles, 200 kV is a common operation voltage in an HAADF-STEM, although lower voltages would allow investigation of the presence of molecules on the nanoparticle surface and a deeper understanding of the structure of the support matrix surrounding the nanoparticle. The HAADF detector is set normally at an inner angle ~50 mrad, and the outer angle is set ~100–200 mrad.

STEM-HAADF is extremely useful for size determinations in catalysts. This is exemplified in Figure 4.7. Several STEM micrographs of gold nanoparticles were used to generate a histogram of sizes. Figure 4.7a shows one of these micrographs. The particles, well distributed on the substrate, are easily recognized by the software once a threshold value of intensity and a minimum particle size are defined; Figure 4.7b shows the histogram. In this example, the statistics gave a mean size of 2.3 nm, with a standard deviation of 0.49 nm. Several factors may affect the confidence on the size measurements, such as out-of-focus regions in the image or a low contrast level. This kind of procedure is extremely useful in catalytic research.

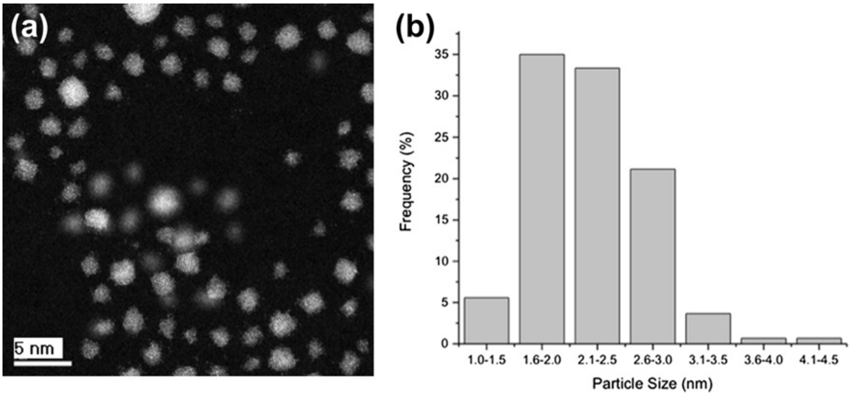

Figure 4.7 Histogram of sizes of gold particles obtained using STEM-HAADF images. Since no delocalization is produced on the image, the size distribution is more accurate.

2.4. Practical Guide for STEM Imaging

The basic parameters described in this section are used to register high-resolution STEM images. The process must be started in TEM mode for the selection of the field of view and to adjust the crystal orientation, if needed. The eucentric focus must be adjusted with the *z*-control. By following the TEM initial setup, the system can be switched to STEM. The illumination focused on the sample must be adjusted by varying the size of the condensed aperture, the spot size, and the camera length (*L*). Camera length is the effective distance or magnification between the specimen and the detector plane position. The collection angle depends on microscope camera length. Typical collection angle values for ADF and HAADF detectors are close to 40 and 200 mrad, respectively.

The resolution in STEM depends on the spot size of the electron beam. Spot size and the aperture of the condenser lens influence the beam current density in the sample and, as a consequence, on the resolution of the instrument. The beam current density in the sample can be increased either by a large aperture of the condenser lens or by using a lower spot size. Figure 4.8 shows two sketches for the rays under two different settings for STEM. Increasing the spot size (spot number) leads to increased demagnification of the source and a decreased current in the beam. Increasing the spot number leads to a reduction of the beam current.

Changing the size of the condenser lenses CL1 and CL2 also changes the beam current. Figure 4.9 sketches the rays corresponding to two

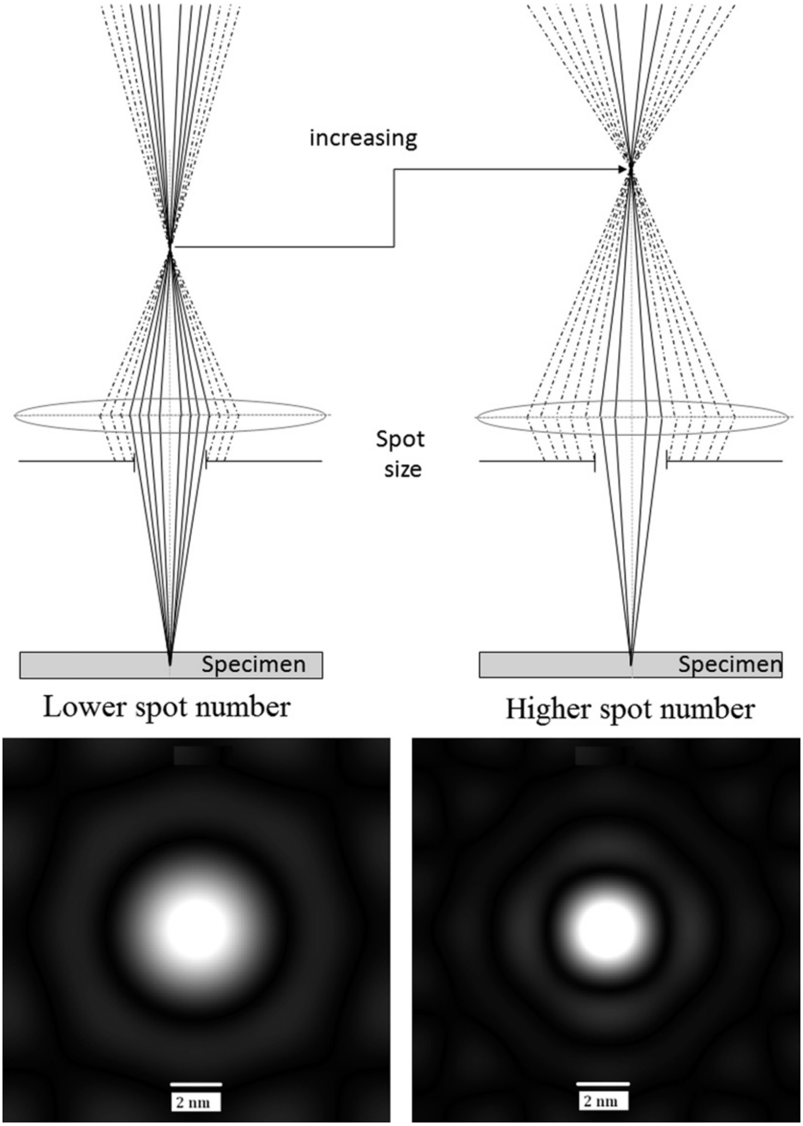
increasing
Spot
size
Specimen
Specimen
Lower spot number
Higher spot number
2 nm
2 nm

Figure 4.8 Electron beam sketches varying the spot size and the potential projected simulated depending on the spot size.

different sizes of the condenser apertures. The selected aperture must be centered in the ronchigram (described in next section) as shown in Figure 4.9.

Spot size and aperture of the condenser lens determine the resolution of the microscope in STEM mode. The spot size, measured in

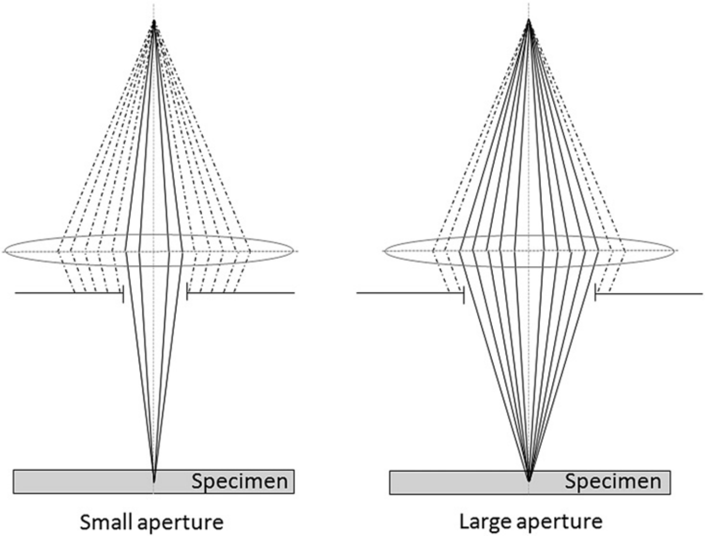

Figure 4.9 Electron beam trajectories by varying the condenser lens apertures.

nanometers, can be simulated as a function of the parameters of the microscope (Zuo, 2008).

A very useful tool is the ronchigram, which is a shadow image formed by a focused and stationary electron probe on amorphous material. The quality and resolution of the STEM images depend directly on the proper alignment of the ronchigram. It is easily observable in FEG microscopes, but it might be difficult to obtain when lanthanum hexaboride (LaB_6) filament sources are used because the effective probe size is too large; therefore both the spatial resolution and the brightness decrease dramatically even with microscopes with voltages exceeding 200 kV. All the parameters that affect contrast and spatial resolution also affect the ronchigram. The ronchigram can be registered in a charge-coupled device camera. The ronchigram is also known as the Gabor hologram, or as the central zero-order disk of the convergent beam electron diffraction (CBED) pattern. The ronchigram from an amorphous region should look as in Figures 4.10a and 4.10c. The shape of the ronchigram can be simulated using the parameters of the microscope (Zuo, 2008).

In the ronchigram, the focus spot must be represented in the center of the shadow image as a region of infinite magnification. Overfocus, in-focus, and underfocus ronchigrams and the beam incident on the sample are illustrated in Figure 4.11.

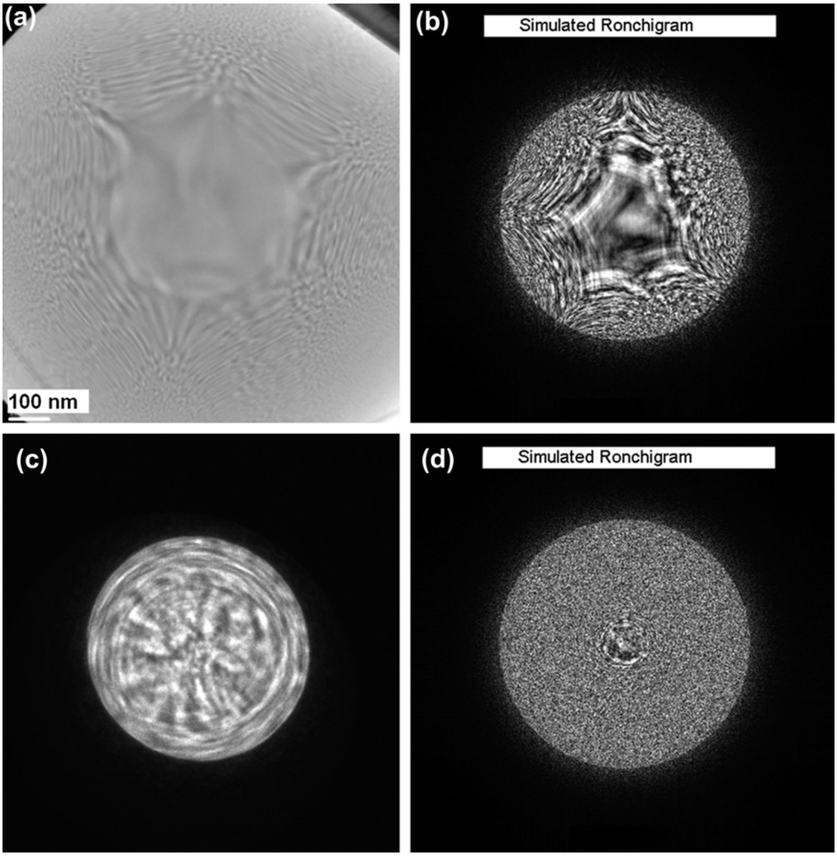

Figure 4.10 Aberration-corrected (a) experimental ronchigram from an amorphous material. (b) Calculated ronchigram. (c) aberration-uncorrected experimental ronchigram from an amorphous material. (d) Calculated ronchigram.

3. EXAMPLES OF APPLICATIONS TO CATALYST CHARACTERIZATION

3.1. Metal Catalysts on a Crystalline Substrate

For metal catalysts supported on a crystalline substrate, the best technique to observe the nanoparticles is STEM–HAADF, because with this technique the reflections of the metal and the substrate are clearly separated on the reciprocal space and it is straightforward to visualize the nanoparticles. A very common support for metal nanocatalysts is TiO_2, which is very easy to grow and has been used extensively (Diebol, 2003). Figure 4.13a shows an example from the laboratory of Dr. Gabriela Diaz at the Institute of

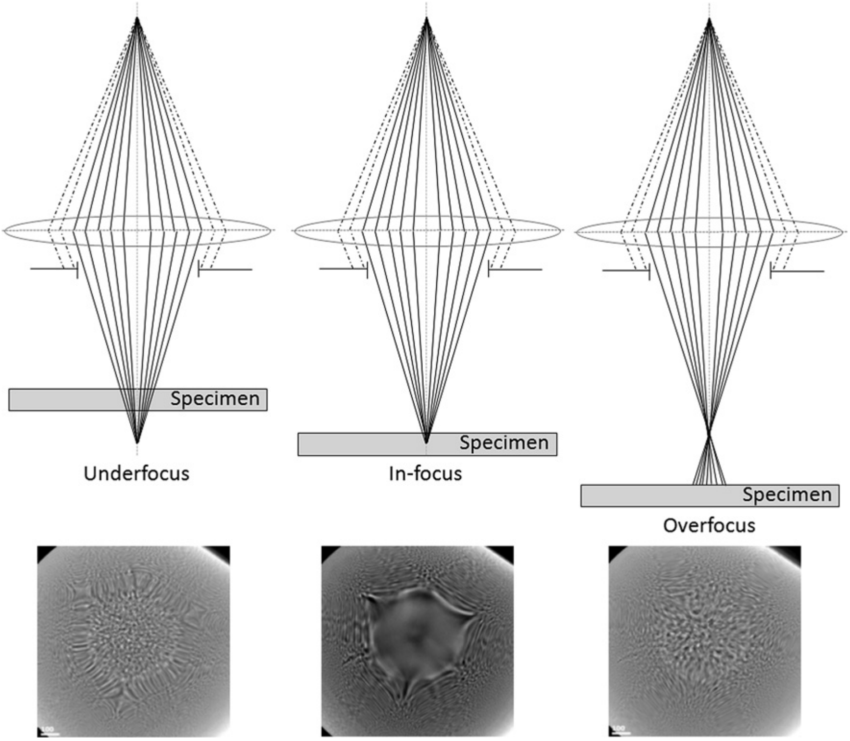

Figure 4.11 Ronchigram for different focus conditions.

Physics at the National Autonomous University of Mexico (UNAM). The micrograph corresponds to an iridium metal supported on a TiO_2 (anatase) substrate. The metal clusters are clearly seen as formed white spots, each representing an atomic column. To further demonstrate the potential of the technique we can measure the intensity profile of the spots, and since there is only one metal on the sample, the intensity should be proportional to the number of atoms on the column. Figure 4.12b shows the intensity profile for the cluster marked with an arrow in Figure 4.12a. The profile indicates that the four columns have the same number of atoms indicating a flat or “raft” shape (Jang *et al.*, 2009). A further calibration of the intensity is required if the exact number of atoms is to be determined. In this case, we must first filter the substrate contribution and find a suitable region with isolated atoms. In any case, the relevant information for catalysis is that the atoms will expose a (100) facet to the reactant species. A cube-shaped iridium metal (Figure 4.12c) is not expected to be stable by itself but the presence of the crystalline surface makes it stable.

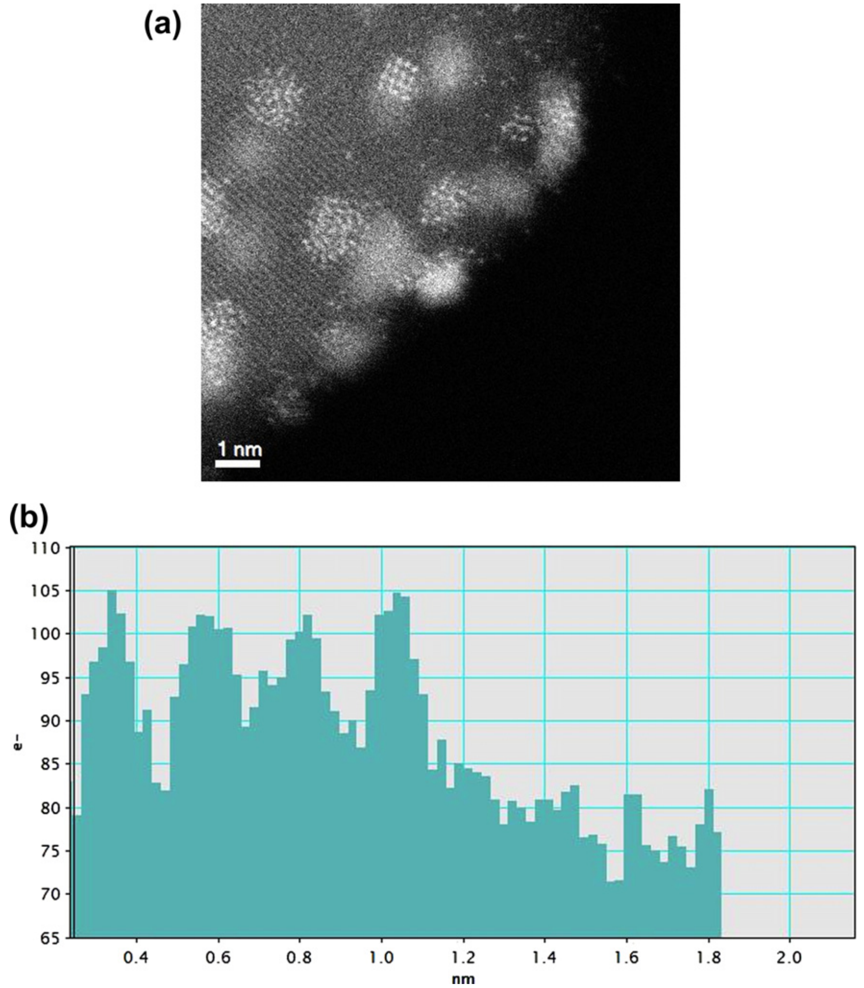

Figure 4.12 (a) STEM-HAADF image of an iridium supported on a TiO_2 crystalline substrate. The clusters of metal are apparent. (b) Intensity profile of the atomic columns of the cluster marked with an arrow in (a). (See the color plate).

Figure 4.13 shows the dramatic difference between bright (STEM) and HAADF-STEM for an Au/TiO_2 catalyst. In the BF mode only the crystal structure of the catalyst can be observed. However, in the DF image not only clusters but also single atoms can be observed. Clearly, STEM-HAADF should be used when possible. The question that now arises is: Can some chemical information be obtained about clusters this size? The first point that should be very clear in this chapter is that while X-ray EDS and EELS

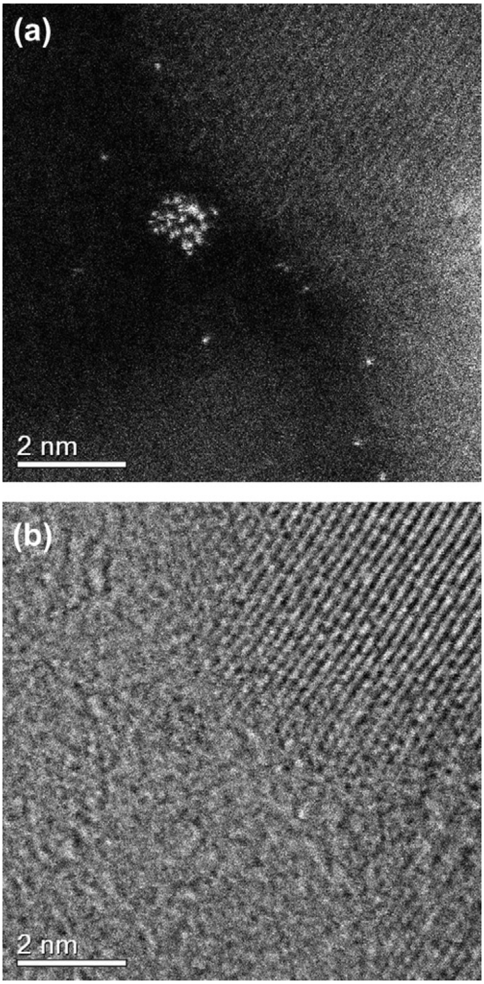

Figure 4.13 Images of an Au/TiO_2 catalyst showing the contrast of the two techniques: (a) HAADF and (b) BF-STEM of the same area.

(Friel and Lyman, 2006; Stroppa *et al.*, 2012) are great techniques to accomplish chemical mapping and can be used in catalysis, as shown in other sections of this work, they are very limited for small clusters. Indeed, in many relevant cases the catalysts will be ultra-dispersed—that is, they will contain a few atoms or their size will be a few nanometers. This allows the catalyst to have a large number of atoms at the surface (or even in an ideal case, all the atoms in the surface). However, the number of X-rays emitted by the clusters during a microanalysis study will be low and the signal-to-noise ratio will be unacceptable. Often a catalyst researcher not fully familiar with the

TEM technique expects the chemical composition of its clusters to be determined atom by atom. This certainly can be done in larger samples such as thin films or grain boundaries and even in nanoparticles larger than ~ 5 nm. However, it is not possible for particles <5 nm.

The same situation applies to EELS analysis. Is this the end of the road for chemical identification in very small clusters? The answer is no. STEM-HAADF can yield important information. Figure 4.14 shows an

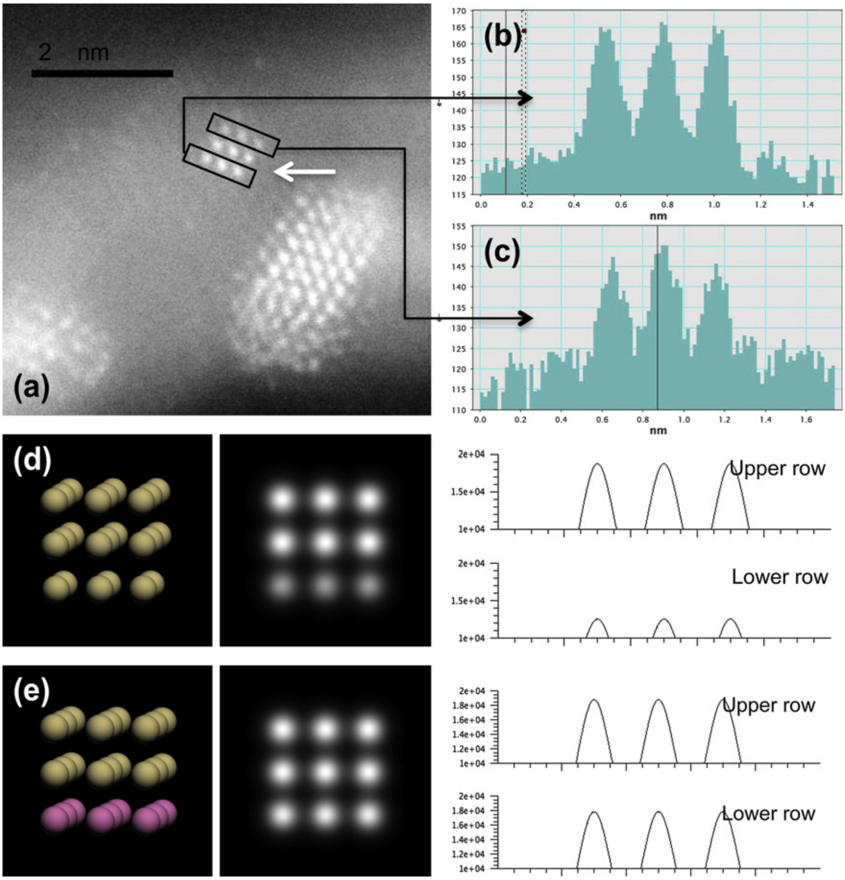

Figure 4.14 (a) STEM-HAADF Image of a Au/Ir alloy supported in TiO_2. The cluster marked with an arrow formed by 3 × 3 columns of atoms is analyzed. (b) Intensity profile of the first (bottom) row. (c) Profile of the third (top) row. Two possible models that are consistent with the data: (d) a stepped structure and (e) the Janus or "eutectic" type of structure. On the right, the simulated STEM micrographs and intensity profiles (arbitrary units) for the models in (d) and (e) are also shown. (See the color plate).

example of a gold-iridium alloy supported on TiO_2. Figure 4.14a shows the HAADF–STEM image of these clusters. If we analyze the rectangular cluster marked by a white arrow, we can obtain the signal intensity for each column of atoms. Figure 4.14b shows the profile for the row of atoms at the bottom. The profile for the next row is similar to the one of Figure 4.14b. However, the row at the top has the same profile but with a lower value of the intensity shown in Figure 4.14c. There are two possible explanations. The first is that all the atomic columns are thicker than one monolayer and all atoms have the same atomic number. In that case, the decrease in intensity would have to be explained as a step on the structure (as shown in Figure 4.14d). The other situation can be obtained by noting that the ratio of the intensities is 0.94 and if we assume that the last column is iridium and the first two are gold, then the ratio of the STEM signals according equations described before is 0.94. Therefore, a very plausible model is the one shown in Figure 4.14e in which one row corresponds to iridium atoms and two rows correspond to gold atoms. This is the Janus-type particle. Of course, this is not a definite proof and additional data are required. A careful calibration of intensities for a more involved model can be made to obtain intensities using the methods described in Kotaka (2010) and Recnik (2005).

3.2. Metals on a Noncrystalline Substrate

A second relevant case concerns particles supported in an amorphous or semi-amorphous substrate. In this case, the contrast is more complicated since the substrate also has incoherent electrons scattered at high angles, thus increasing the signal-to-noise ratio. Therefore, a more careful interpretation is needed. A typical case is that of the metals supported on Vulcan carbon. Figure 4.15 shows such an example for iridium. Clearly, the HAADF-STEM image can be used to very accurately determine the particle size in large areas (and the particle size distribution). The fact that no delocalization effect, which is very pronounced on field emission microscopes, is present on this type of images (Carter and Williams, 2009) makes the size determination very accurate.

In some special cases, the Z-contrast can be nicely combined with BF images to complete the picture. Figure 4.16 shows an example in which a platinum nanoparticle is supported in a carbon fullerene onion (CNO). The images, both BF and DF, allow the location of particle on the graphitic structure. It is clear that the particle is located in the interlayer zone of the

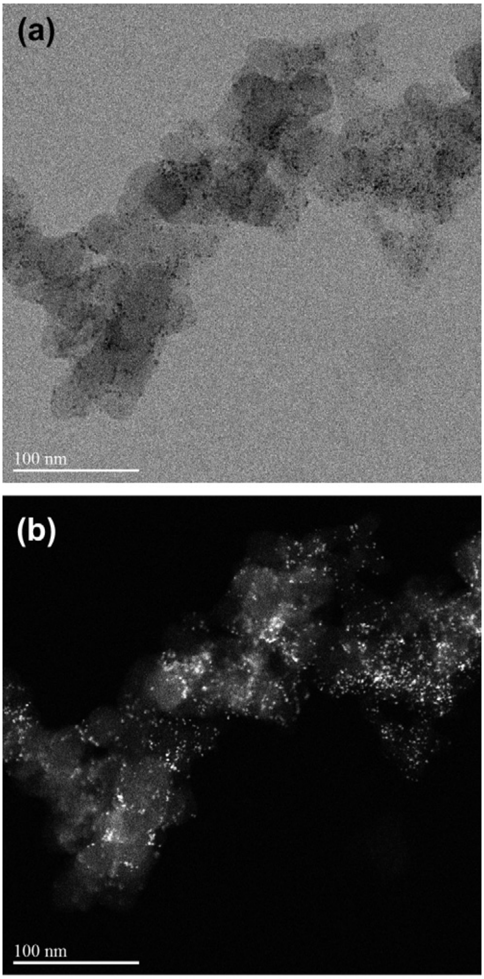

Figure 4.15 Example of contrast of iridium supported on Vulcan carbon. The images of the particles in STEM-HAADF are ideal for size distribution determination. (a) DF- and (b) BF-STEM bright field.

onion (Figure 4.16b). In this case, the background from the substrate acted in favor of a more complete characterization.

In some cases, amorphous carbon produces too much noise on the Z-contrast images, and often it is better to use HREM TEM in the transmission mode. This is more important when the catalysts are ultra-dispersed and the nanoparticles contain very few atoms. Figure 4.17 shows an example for a palladium catalyst supported on Vulcan carbon.

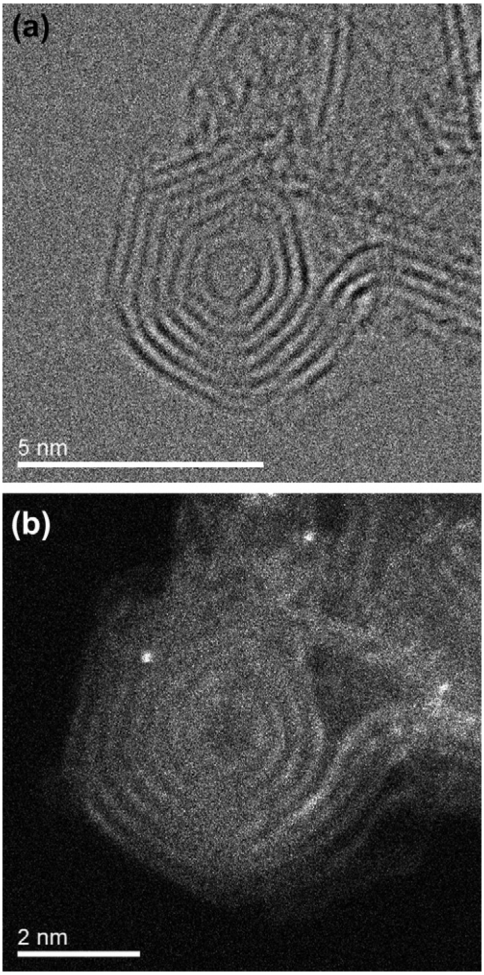

Figure 4.16 Pair of STEM-HAADF images. (a) DF and (b) BF of a CNO onion structure with a platinum particle.

In this case, the aberration-corrected image show clusters consisting of a few atoms. There is no doubt that BF-TEM works much better for this particular case.

3.3. Metals on γ-Al_2O_2

Some of the most important catalysts on petroleum refining are noble metals such as platinum, palladium, ruthenium, rhodium, and recently even gold supported on γ-Al_2O_3 (Frenkel *et al.*, 2001; Rioux, 2006; Ahmed *et al.*, 2009). The alumina is a porous support with a face-centered cubic (FCC)

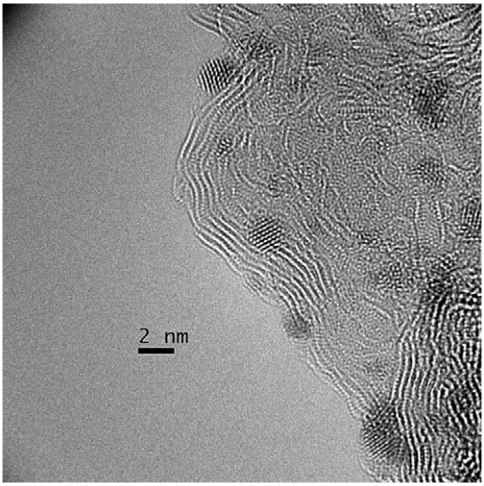

Figure 4.17 HR-TEM image using an aberration corrected TEM of palladium nanoparticles supported on Vulcan carbon. Atomic resolution of the clusters can be clearly observed. In this case, the signal-to-noise ratio is very good to distinguish nanoparticles from the support.

structure $a = 7.90$ Å. The structure of the metal has been the subject of vast investigation (Ahmed *et al.*, 2009). The point is whether the cluster is flat (rafts or 3D in shape). Aberration-corrected STEM-HAADF can offer clues. Figure 4.18a shows an image of a Pt/γ-Al_2O_3 catalyst. The profile of the cluster marked with A is shown in Figure 4.18b. The particle is clearly 3D because of the Gaussian shape, and its size is about 1 nm. One structure consistent with this size and shape is the on 13-atom icosahedron. The diffraction from these planes falls in reciprocal space very close to the high-angle scattering of the metal. Therefore, it is possible to see single atoms intercalated on the planes. If we calibrate the intensity of a single atom in the same figure and consider the ratio with the maximum intensity of the cluster, we find that N (the number of atoms in the cluster) is ~2.8 for the maximum value of intensity; this is again consistent with the icosahedral shape. So it appears that the idea of rafts is not valid in this case, but the catalyst seems to have most of the atoms on the surface. A 13-atom icosahedron is a possibility. However, a new important possibility for metals was recently found by Longo and Gallego (2006), who reported that for platinum a buckled planar structure is more stable than the icosahedron. This structure, which also has 13 atoms, is shown in Figure 18c and will have all its atoms on the surface. This appears quite consistent with the experimental

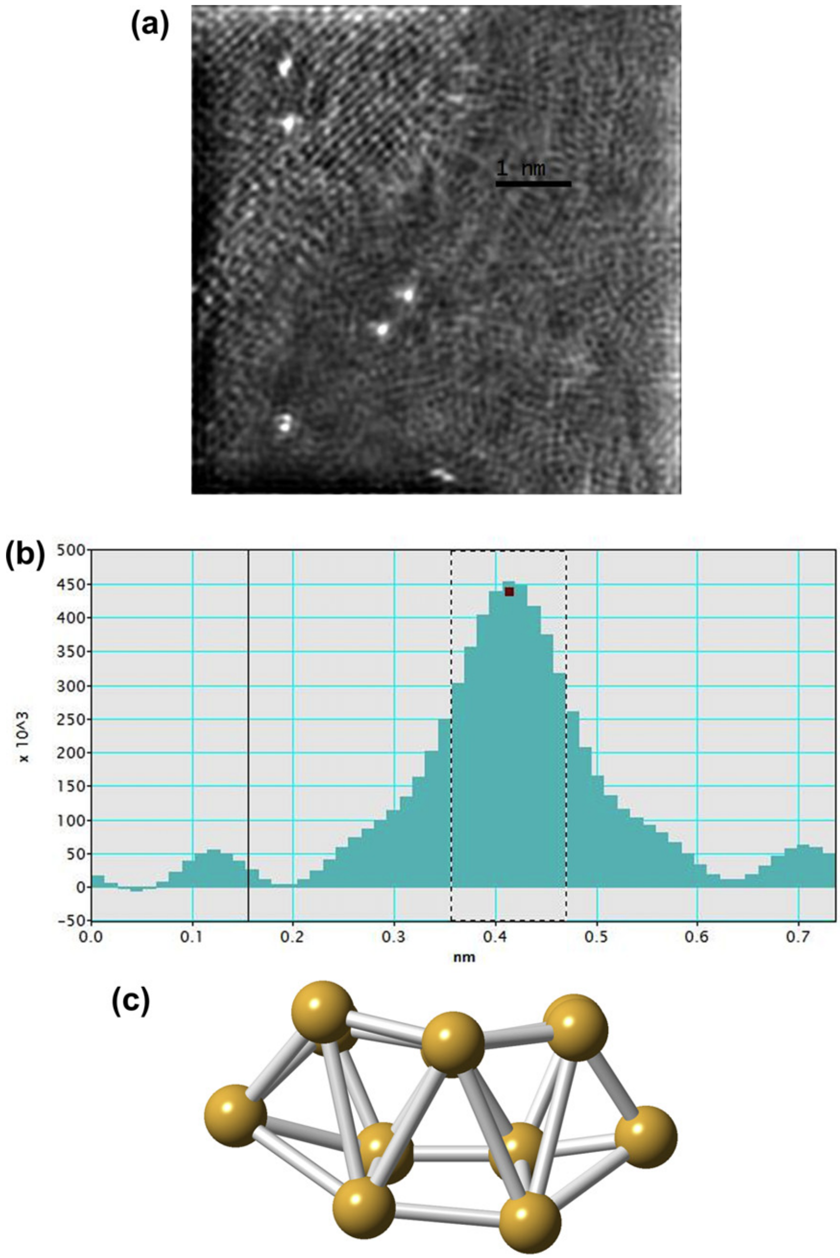

Figure 4.18 (a) TEM-HAADF image of a Pt/γ-Al_2O_3 catalyst. The (444) lattice lines of the alumina can be observed. The bright dots correspond to clusters and to single atoms. (b) Intensity profile of the cluster marked with an arrow in a 3D shape is not consistent with the structure of a raft. (c) A 13-atom optimized cluster is shown that might correspond to the shape observed. (For color version of this figure, the reader is referred to the online version of this book).

observations since the intensity profile will be consistent with two layers. The other platinum metal on the catalysts will be present as individual atoms.

A conclusion from the previous discussion is that flat or raft types of structures seem to be stable only when there is a strong metal-substrate interaction as in the case of metal-TiO_2. In the case of weakly interacting substrates such as γ-Al_2O_3, pseudo-spherical shapes are preferred.

3.4. Bimetallic Nanoparticles and Clusters

Bimetallic nanoparticles are a combination of two individual metallic systems that come together to form an alloy. This combination serves as a platform to enhance both their individual and collective properties. Thus, compared with monometallic systems, bimetallic systems have greatly improved properties; a typical case, for example, is their improved reactivity in catalysis for many varied reactions. For bimetallic nanoparticle alloys, the synergy in the hybrid material can presumably be attributed to the electronic coupling of the individual metals and in addition to the geometric effects that may be caused by the different lattice constants (Stamenkovic *et al.*, 2007). The concept of bimetallic nanoparticles goes back to the 1970s where it was used in catalysis of two different metals such as gold and palladium in the same nanoparticle (Sinfelt, 1983). This idea was developed by Toshima's group, (Harada *et al.*, 1993) who used polyvinylpyrrolidone (PVP) to stabilize core-shell bimetallic gold-palladium nanoparticles—for instance, nanoparticles in which the core is gold but palladium atoms are located on the shell (He *et al.*, 2003). Subsequent to coreduction, this structure is controlled by the order of reduction potentials of both ions and the coordination abilities of both atoms to PVP. The location of gold in the core and palladium on the shell was demonstrated by extended X-ray absorption fine structure, and it was shown that such heterobimetallic gold-core palladium nanoparticles are more active in catalysis than simple PVP-stabilized palladium nanoparticles. Thus, the gold core enhances the catalytic properties of palladium nanoparticles at the palladium nanoparticle surface (Toshima, 1996). Conversely, design strategies can lead to the opposite core-shell structure (palladium core, gold shell), and specific catalytic properties were obtained for methylacrylate hydrogenation (He *et al.*, 2003). Thus, with the observation of a remarkable enhancement in the properties of bimetallic nanoparticles, they have continued to evoke vigorous scientific interest.

3.5. Understanding the Structure of Bimetallic Nanoparticles and Clusters Using Advanced Electron Microscopic Techniques

Direct microscopic studies of various bimetallic nanoparticles have been performed using HR-TEM (Perez-Tijerina *et al.*, 2008; Perez-Tijerinam *et al.*, 2010; Mejia-Rosales *et al.*, 2006). However, this method is limited because of the small difference in the lattice constant involved. TEM can produce chemical contrast due to different electron beam extinction distances. This has been applied successfully to image bimetallic nanoparticles down to 10 nm in diameter. Since the particles need to be in a low-index zone orientation, this method is not easy to use in practice (Srnová-Šloufová *et al.*, 2000). A novel approach to study this type of particles is based on the use of an HAADF technique in a TEM, which allows the observation of the interfaces between layers of different elements due to differences in atomic number, densities, or the presence of strain fields due to differences in lattice parameters. However, in recent times the study of bimetallic nanoparticles has been greatly improved with the use of aberration-corrected scanning/transmission electron microscopy (S/TEM), which yields a new level of understanding of the behavior of these systems at the atomic scale. A combination of the HAADF imaging mode in an aberration-corrected STEM/TEM reveals a wealth of information about these systems. It is well established that, when recorded under appropriate illumination and collection geometries, incoherent HAADF-STEM images are compositionally sensitive and provide direct information on atomic positions, which is crucial in the differentiation of variation in the atomic compositions while imaging.

The conventional understanding of bimetallic nanoparticles is that they have one of four fundamental structures: (1) alloys, (2) core-shell, (c) onion, or (d) Janus (Figure 4.19).

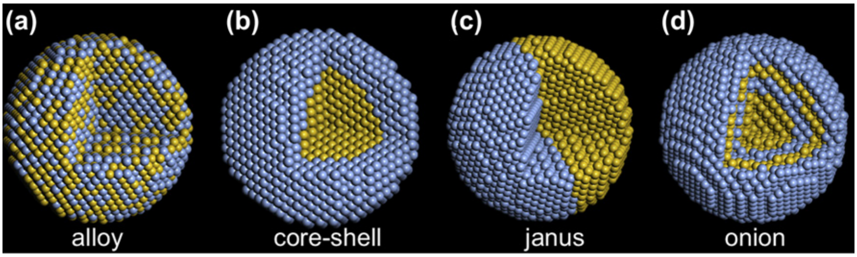

Figure 4.19 The four main types of structures on bimetallic nanoparticles: (a) alloys, (b) core-shell, (c) Janus structure, or (d) onion structure. (See the color plate).

Several factors play a role in determining which of the four alternatives is more likely to occur. These factors include the solubility of the metals, the relative surface energy, the kinetics of the synthesis, and several others. In the case of gold-palladium nanoparticles, both types of structures can be formed. Gold-palladium is a particularly interesting system because of its applications as hydrogenation catalysts and the two metals are fully soluble in bulk. Hence, both alloy nanoparticles, as well as core-shell gold-palladium nanoparticles, can be obtained depending on how the individual metal ions themselves are reduced (Mizukoshi *et al.*, 2000). Figure 4.20 shows the probe aberration HAADF images of nanoparticles of $AuPd_3$ with the alloyed structure. It is clear that some atomic columns are significantly brighter that adjacent columns, as shown by the contrast of the atom row with arrows in the inset of Figure 4.20b. The top of Figure 4.20c shows intensity traces over two single atoms labeled atom 1 and atom 2. These are typical of several such traces in Figure 4.20b and suggest that the higher-intensity atom is gold and the lower one is palladium. Since the intensity is proportional to $Z^{1.6}$, the relative single-atom intensities should be $791.6/461.6 = 1087/458 = 2.37$. It is very reasonable to assume that the more-intense atoms correspond to gold and the less intense atoms correspond to palladium since the intensity ratio is 1.8, a reasonable approximation of the expected ratio of 2.37, given the low sampling and low signal above background. With regard to the bright central column, if it is all palladium, then it represents an unreasonable number (at least three) of the palladium atoms extending above the general

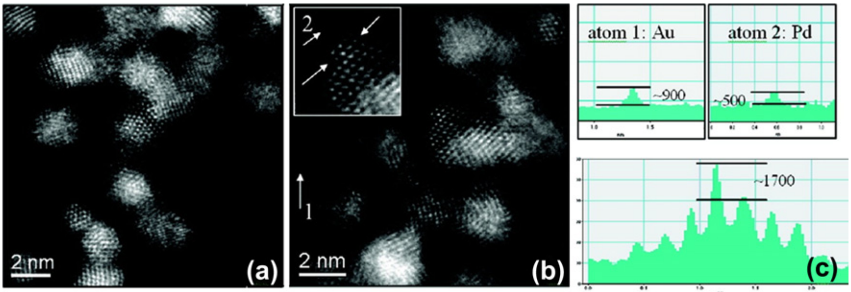

Figure 4.20 (a) and (b) HAADF images of typical $AuPd_3$ nanoparticles. Single-atom traces (top of (c)) suggest a palladium intensity of 500 counts versus a gold intensity of 900 counts. The profile of the atom row indicated on the inset (c, bottom) shows a central column roughly triple the intensity of the adjacent column, presuming all palladium atoms. This suggests the presence of one or more gold atoms in the central column. *(Reprinted with permission from Mejia-Rosales* et al. *(2006). Copyright (2007) American Chemical Society).* (See the color plate).

surface. This is not favored energetically; it is likely therefore that one or more gold atoms contribute to the intensity of this column. The roughness of the surface, due to the presence of extended point defects, can also be seen clearly.

A different situation can be seen for gold-palladium nanoparticles which were obtained by successive reduction of metal ions. In this case it was found that when particles (with different gold and palladium compositions) were synthesized by chemical methods, a much more complex situation arises, in which the nanoparticles show a structure with three alloyed layers and with different compositions (Ferrer *et al.*, 2008). Figure 4.21 shows the ultra-high-resolution HAADF images of the gold-palladium nanoparticles obtained in a probe aberration-corrected STEM. From Figure 4.21a it can be seen that the three layers in the nanoparticle are clearly evident. The diameter of the nanoparticles is ~8 nm. This consists of a palladium core (A ~ 2 nm), gold-rich first shell (B ~ 3 nm), and palladium-rich outer shell (C ~ 3 nm) (shown from the contrasts in the HAADF images in Figure 4.21a). The HAADF intensity is considered to be proportional to $Z^{1.6}$ and hence the difference in atomic number (Z) that exists between gold and palladium is clearly revealed in the three-layer nanoparticles (gold, $Z = 79$; palladium, $Z = 46$. The shape of this particle corresponds to

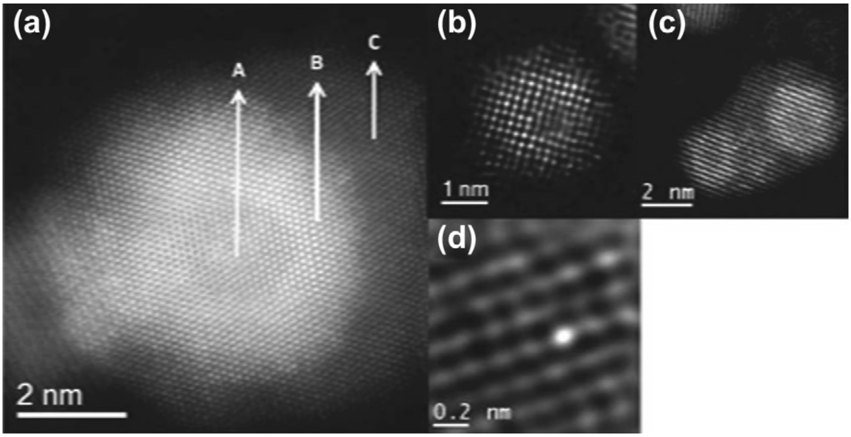

Figure 4.21 Aberration-corrected STEM images of the three-layer Au/Pd nanoparticles. (a) Atomic-resolution HAADF-STEM image of a truncated cuboctahedral Au/Pd nanoparticle. The contrast of the three distinct regions (marked A (palladium), B (gold), and C (palladium)) can be clearly identified. (b) Nanoparticles with rough surface and distortions at the core. (c) and (d) Gold intercalation into the palladium layer. *(Reprinted with permission from Deepak* et al. *(2011a). Copyright (2011) Elsevier).*

a truncated octahedron, which has (111) and (100) facets. Figure 21b shows a three-layer particle with the (100) orientation where roughness on the surface and distortion in the core of the nanoparticle can be seen. In some nanoparticles, it may also be seen that the gold atoms are indeed diffused into the palladium-rich outermost shell as seen from the bright atom contrast in the palladium layer. Figures 21c and 21d show the atom-by-atom intercalation of gold in the palladium layer. This shows how gold can be present in the palladium layers and is not entirely rigid. So the layers indeed are alloys of different concentrations (Deepak *et al.*, 2011a).

The energy dispersive analysis of X-ray (EDAX) for the three-layer gold-palladium-gold nanoparticles reveals the following interesting features (Figure 4.22a). The palladium L-shell and the gold L- and M-shell signals can be clearly be used to identify the individual palladium and gold layers (Figure 4.22b). Figure 4.23 shows the chemical maps of the gold-palladium nanoparticles. It can be seen from the figure that the maps for the palladium (K and L shells) and gold (L and M shells) clearly reveal the presence of the individual elemental contrasts in the three-layer core-shell structure of the nanoparticles. With the information obtained from the EDAX line scans and elemental maps of the individual nanoparticles, the presence of the palladium core, gold first shell, and palladium outer shell is clearly confirmed without any ambiguity.

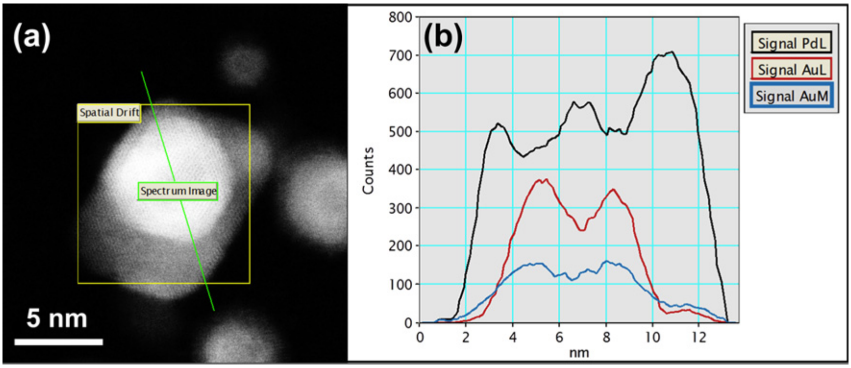

Figure 4.22 (a) and (b) Characterization of the gold and palladium elemental distribution across the nanoparticle by STEM-EDAX line-scanning technique across the individual three-layer nanoparticle. The Pd-L and the Au-L,M line scan signals (b) can be clearly seen varying in intensity along the different regions of the nanoparticles. (a) The analyzed area and the direction of analysis. *(Reprinted with permission from Deepak* et al. *(2011a). Copyright (2011) Elsevier).* (See the color plate).

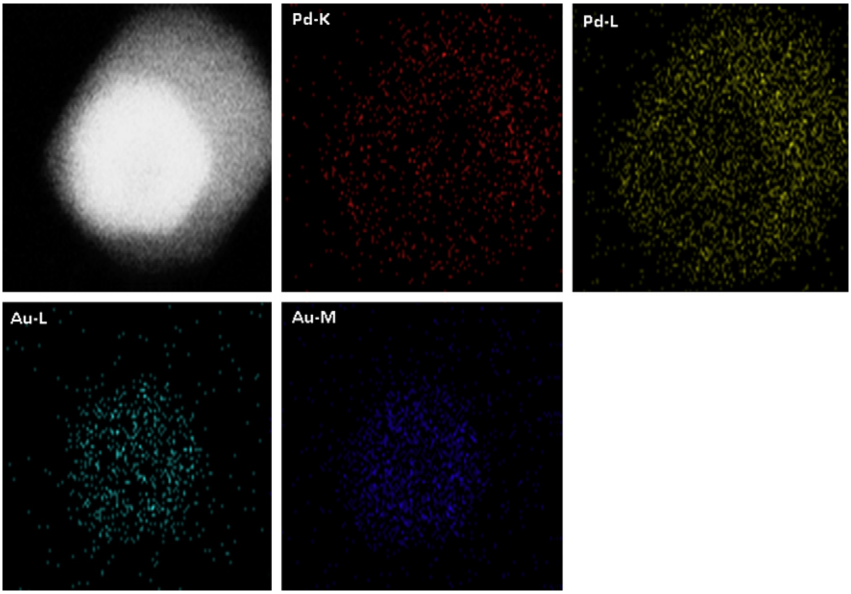

Figure 4.23 Elemental maps of the nanoparticles for Pd-K and Pd-L (top) and Au-L and Au-M (bottom). *(Reprinted with permission from Deepak et al. (2011a). Copyright (2011) Elsevier).* (See the color plate).

The distribution of the chemical elements of the three-layer nanoparticle (Figure 4.24a) was investigated by EELS; Figure 4.25b shows the result for the EELS line profile of Pd-$M_{4,5}$. For purposes of comparison, the figure also shows the HAADF intensity line profile of the same particle (Figure 4.24d). From the EELS profile (Figure 4.24c) it can be noted that the distribution of palladium appears to be in accordance with the presence of palladium in the core and in the outermost shell as is the case for a trilayer particle. However, the EELS Au-$M_{4,5}$ signal at 2206 eV turns out to be weak, as expected for a heavy element, but high enough to show the presence of gold in the particle.

From the comparison between the palladium EELS profile and the HAADF profile, it can be inferred that a palladium-rich region exists close to the center of the particle, and another in the outermost shell. The corresponding EELS map of palladium clearly reveals the presence of palladium in the core and the outermost shell of the tri-layered nanoparticles (Figure 4.25).

It is important to note that in case of these nanoparticles a four-layered structure is seen occasionally. Figure 4.26 shows such a four-layer structure

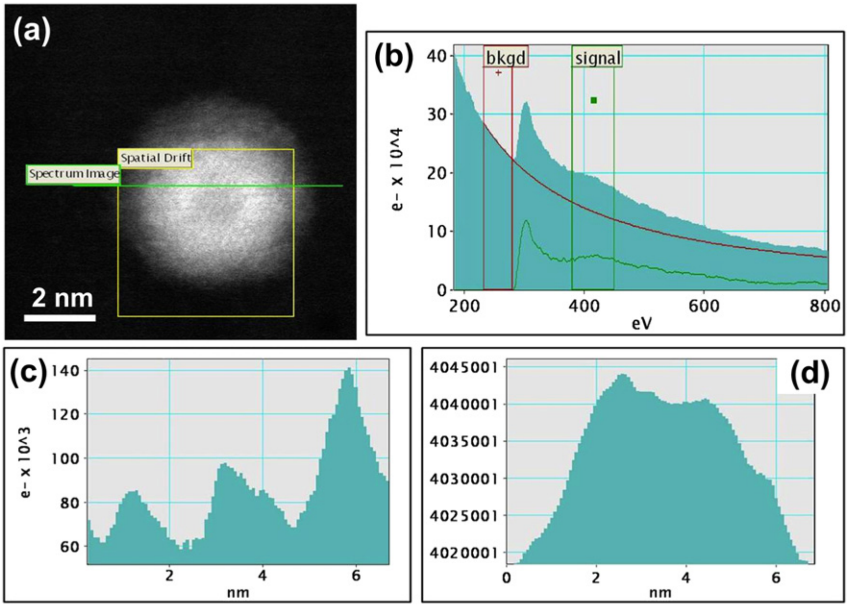

Figure 4.24 The distribution of the chemical elements of the three-layer nanoparticles. (a) Investigated by EELS; (b) the result for the EELS line profile of Pd-$M_{4,5}$. (c) Linear palladium EELS profile performed on the particles; (d) its corresponding HAADF intensity profile. *(Reprinted with permission from* Deepak et al. *(2011a). Copyright (2011) Elsevier).* (See the color plate).

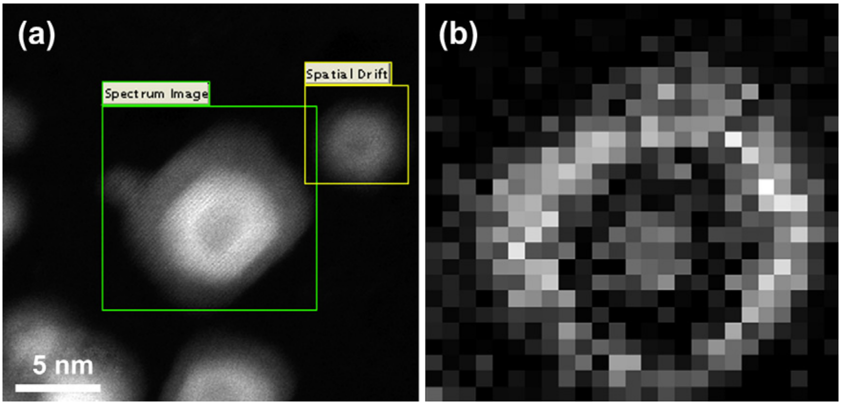

Figure 4.25 EELS map of palladium clearly reveals its presence in the core and in the outermost shell of the trilayered nanoparticles. *(Reprinted with permission from* Deepak et al. *(2011a). Copyright (2011) Elsevier).* (For color version of this figure, the reader is referred to the online version of this book).

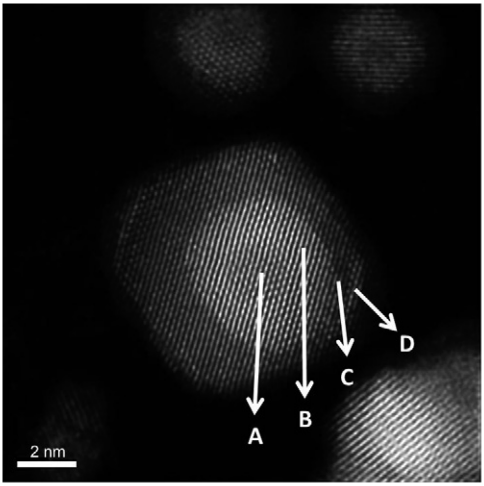

Figure 4.26 Aberration-corrected STEM images of the four-layer Au/Pd nanoparticles. The contrast of the four distinct regions (marked A, B, C, and D) can be clearly seen. *(Reprinted with permission from Deepak* et al. *(2011a). Copyright (2011) Elsevier).*

where an extra layer of gold atoms can be seen tnear the surface, which suggests the four layers. This is a different case from the previously mentioned three-layered nanoparticles and has not previously been reported.

The three-layered nanoparticles were investigated individually using nanobeam electron diffraction (NBD). This technique allows investigating the crystal structure in an area down to the nano scale by using a concentrated yet still nearly parallel electron beam with the probe size as small as a few nanometers or less (Ferrer *et al.*, 2009). The analysis of the crystal structure using TEM NBD and a typical NBD pattern from a nanoparticle are shown in Figure 4.27a. This NBD pattern can be indexed using the hexagonal close-packed (HCP) structure. The NBD is oriented in the zone axis [21.1]. The experimentally (and theoretically) calculated values of the diffraction spots along with their respective angles are shown in Tables 1 and 2. The lattice parameters calculated using the HCP structure are $a = \mathrm{b} = 0.4105$ nm and $c = 0.6647$ nm ($c/a = 1.619$). The palladium-gold-palladium nanoparticles were analyzed by using weak-beam dark-field (WBDF) technique, which allowed obtaining topological information of the nanoparticles. Figure 4.27b shows a WBDF image of a palladium-gold-palladium nanoparticle. The width and separation of thickness fringes is directly related to the angle of incidence between the electron beam and the sample. The thickness fringes produced by the stacking fault can be observed, which can be interpreted as a band of HCP stacked material produced at the interface. The sequence of

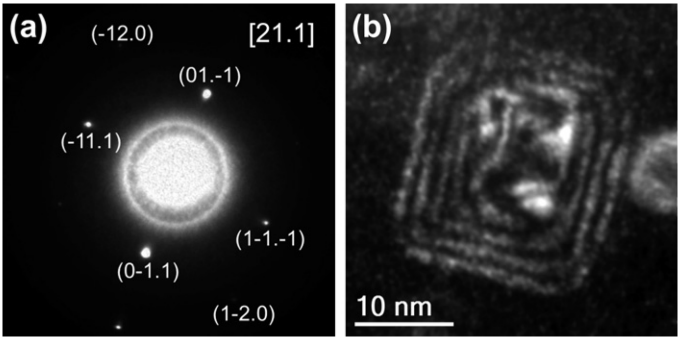

Figure 4.27 (a) Nanodiffraction pattern of an individual Au/Pd nanoparticle. (b) High-resolution weak-beam Dark-Field images of the nanoparticles. *(Reprinted with permission from Deepak* et al. *(2011a). Copyright (2011) Elsevier).*

the thickness fringes is not homogeneous, which is due to the presence of lattice defects (Mayoral *et al.*, 2010).

Figures 4.28a and 4.28b show a three-layered gold-palladium particle in its <110> orientation in the HAADF and BF-STEM modes, respectively. Profiles of the first and second layers of the particle are shown in Figures 4.28c and 4.28d, respectively. The profiles show a very rough surface; this can only be explained if we consider two factors. First, atoms of gold migrated to the surface, causing an increase in signal in those particular columns. Second, there are incomplete columns of atoms (e.g., steps) on the surface.

The BF-STEM images of the three-layer nanoparticle (Au_1Pd_3) are shown in Figures 4.29a and 4.29b; the corresponding HAADF images are shown in Figure 4.29c. The incident electron beam direction is along [110]. The side surfaces of the particles can be indexed as {111} and {100} planes (labeled in Figures 4.29a and 4.29d). The center of the nanoparticles is round, but the exterior surface is square-shaped. The real shape of these particles can be associated with a truncated octahedron. This is extremely interesting since the individual metals themselves will tend to form icosahedral or decahedral shapes. Thus, the structure can be changed with the chemical composition. The nanoparticles have defects at the {111} surface in all directions (Figure 4.29a). A higher magnification of the BF-STEM image in Figure 4.29b shows the defects clearly, and along with the HAADF image shown in Figure 4.29c, gives a clear indication of the variation in the stacking sequence that leads to the stacking faults. Although the standard stacking sequence is ABCABC in FCC structures, in the regions marked in the images (see Figures 4.29b and c), this sequence is not followed. Instead, the sequence becomes ABCAB… (FCC-HCP structure, as seen in

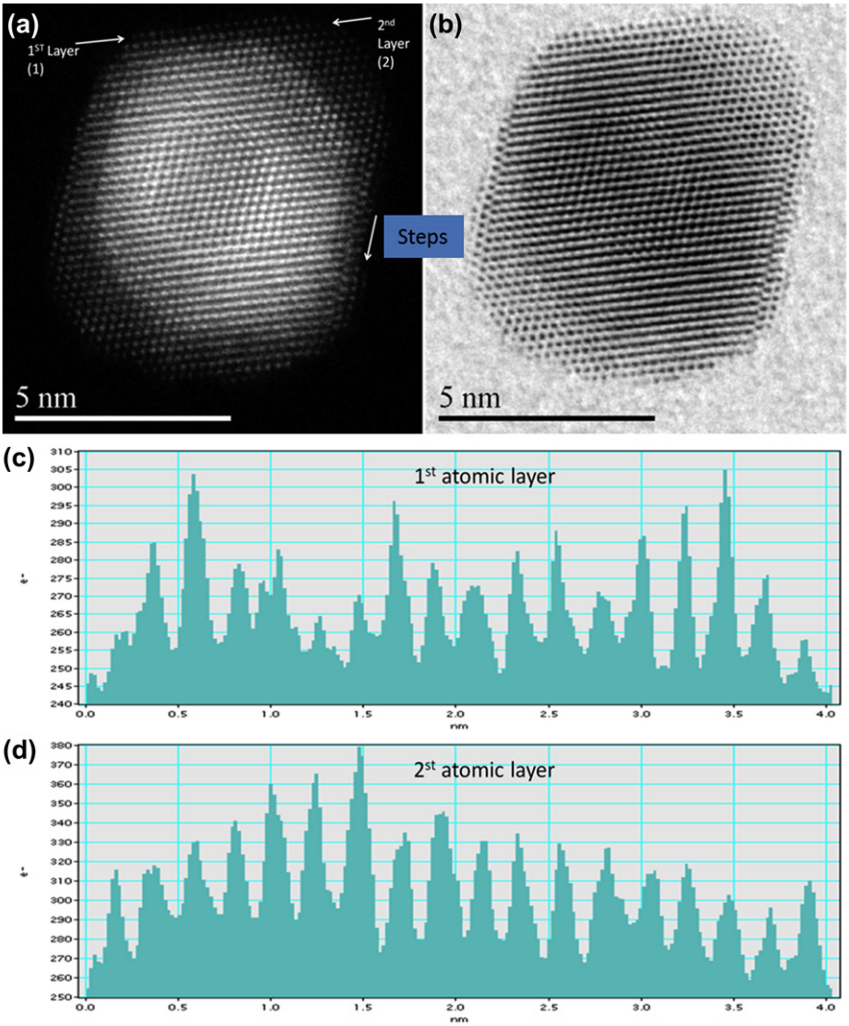

Figure 4.28 (a) HAADF- and (b) BF-STEM images of a Au_1Pd_4 nanoparticle; the images in (c) and (d) show the intensity of the first two atomic layers of the nanoparticle. *(Reprinted with permission from Deepak* et al.*, (2011a). Copyright (2011) Elsevier).* (See the color plate).

Figure 4.29b) and ABCAB… (Figure 4.29c). This corresponds to stacking faults. In addition, the presence of Shockley partial dislocations (SPDs) can be observed (see Figure 4.29a). The formation of stacking faults in gold–pallidium core-shell structures has been shown to be linked to SPDs (Ding *et al.*, 2010). A partial dislocation is accompanied by the presence of a stacking fault. It may be noted here that the large strain involved in the

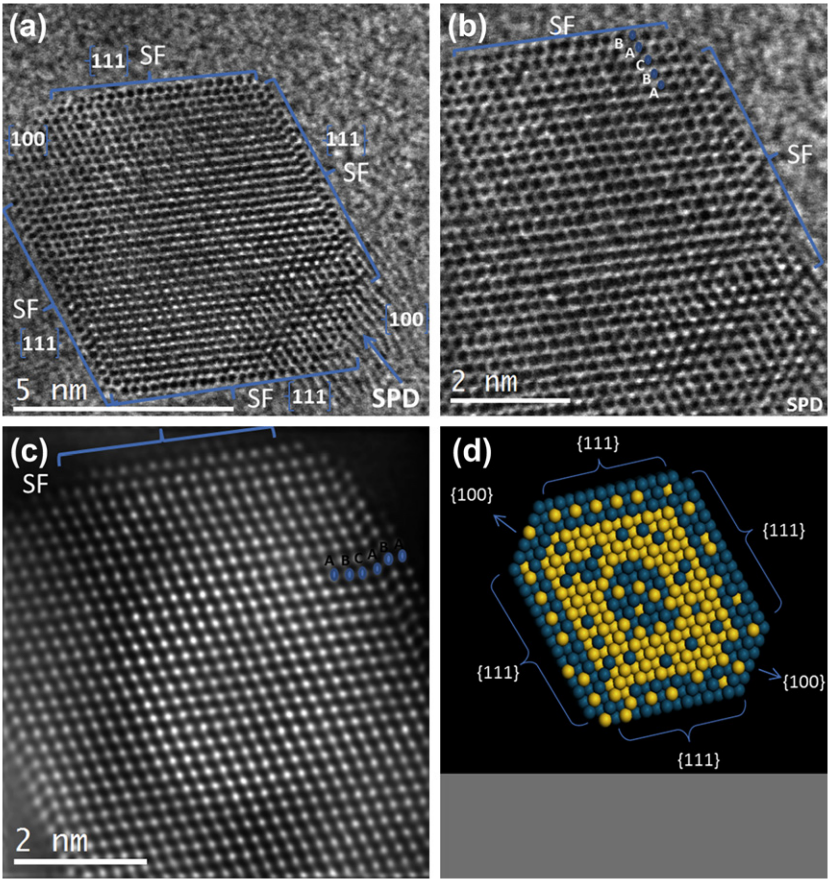

Figure 4.29 The BF-STEM images of the three-layer nanoparticle (a) and (b) and (c) the HAADF image. A higher magnification of the BF-STEM image of (a) is shown in (b) and the HAADF image shown in (c) clearly indicates the variation in the stacking sequence leading to the stacking faults, which is in combination with Shockley partial dislocations. (d) Atomistic model of Au/Pd modified cuboctahedron with the three layers and showing the {100} and {111} facets: a palladium-rich inner core, a gold-rich intermediate shell, and a palladium-rich exterior shell. *(Reprinted with permission from Deepak* et al. *(2011a). Copyright (2011) Elsevier).* (See the color plate).

formation of the three-layer structures may be alleviated to some extent by the formation of such stacking faults and related defects. The stacking faults are also evident for the Au$_1$Pd$_4$ trilayer particles.

Figures 4.30a and 4.30b are the HAADF-STEM and the BF-STEM images, which show a variation in the stacking sequence from the previously mentioned case. Here the stacking sequence of ABCBA is produced by twinning and layer C corresponds to the twinning mirror plane.

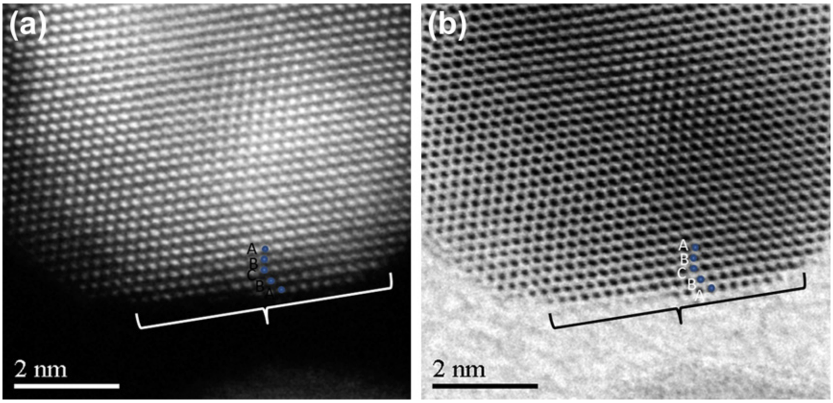

Figure 4.30 HAADF and BF-STEM images of Au_1Pd_4 nanoparticle showing the presence of twinning. *(Reprinted with permission from Deepak* et al. *(2011a). Copyright (2011) Elsevier).* (For color version of this figure, the reader is referred to the online version of this book).

It is indeed interesting to note that the ultimate resolution of observing individual atoms/small clusters has been achieved using probe aberration-corrected STEM. Figure 4.31 shows the very small bimetallic clusters of palladium-iridium (inside the circle). The size of the cluster is just about ~2 nm. It is interesting to note that based on the Z-contrast, the two different atoms can be distinguished very clearly (palladium, $Z = 46$; iridium $Z = 77$). In addition, it is also possible to locate individual atoms of iridium

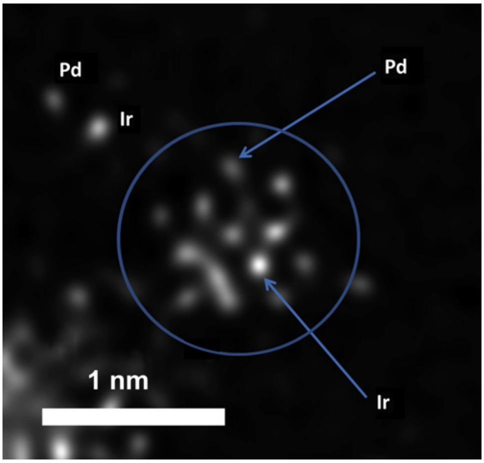

Figure 4.31 Clusters palladium-iridium are shown (inside the circle). It is possible to distinguish each element based on the Z-contrast (palladium = 46, iridium = 77). Notice also the presence of individual atoms (outside and close to the circle). (For color version of this figure, the reader is referred to the online version of this book).

and palladium in the vicinity of these small clusters (outside the circle) (Mayoral *et al.*, 2011).

3.6. *In Situ* Heating Experiments of Bimetallic Nanoparticles and Clusters

One of the most exciting experiments performed in an electron microscope uses the *in situ* heating method. This method provides a great deal of information on the behavior of catalysts and other nanomaterials. With the advent of aberration-corrected electron microscopes that provide sub-Ångstrom image resolution, it is of great interest to study the behavior of materials at high temperatures while maintaining the resolution capabilities of the microscope. The *in situ* heating experiments help overcome several performance problems usually associated with standard heating stage technologies.

A typical example of the heating stage experiments is shown for the three-layered palladium-gold-palladium nanoparticles. Figure 4.32 shows a series of HAADF and BF images recorded at magnifications from 500 kx to 8 Mx as temperatures gradually increased from 350 °C to 900 °C in steps of 50 °C. Figures 4.32a–c show the behavior of a cluster of gold-palladium particles during this heating sequence. The core-shell structure is clear in Figure 4.32a at 350 °C but has disappeared in Figure 4.32b at a temperature of 550 °C as the particles homogenize by diffusion. Particle A shows little change in size, whereas particle B shows a suggestion of growth; however, these effects are small and may simply result from a small rearrangement in shape at this temperature. Two small clusters of gold-pallidium atoms appear at the positions marked with arrows; these are probably a result of the migration of atomically dispersed species not seen at this magnification. Figure 4.32c shows the particle grouping at 700 °C. Remarkably, the center particle diminishes greatly in size, with the growth of a new grain on the adjacent surface of the larger particle. The two particles did not sinter together, even though they were apparently in contact at the higher temperature. New particle 1 grew also, but new particle 2 did not change appreciably after its initial formation at the lower temperature. The core-shell structure was not apparent in any particle, suggesting full alloying occurred after time at the higher temperature. The set of BF images in Figures 4.32d–f, corresponding to the above HAADF set, provides additional information to the characterization of the behavior. Crystal lattice can be resolved in BF images at orientations somewhat farther away from the precise orientation required for HAADF images. In Figure 4.32b the

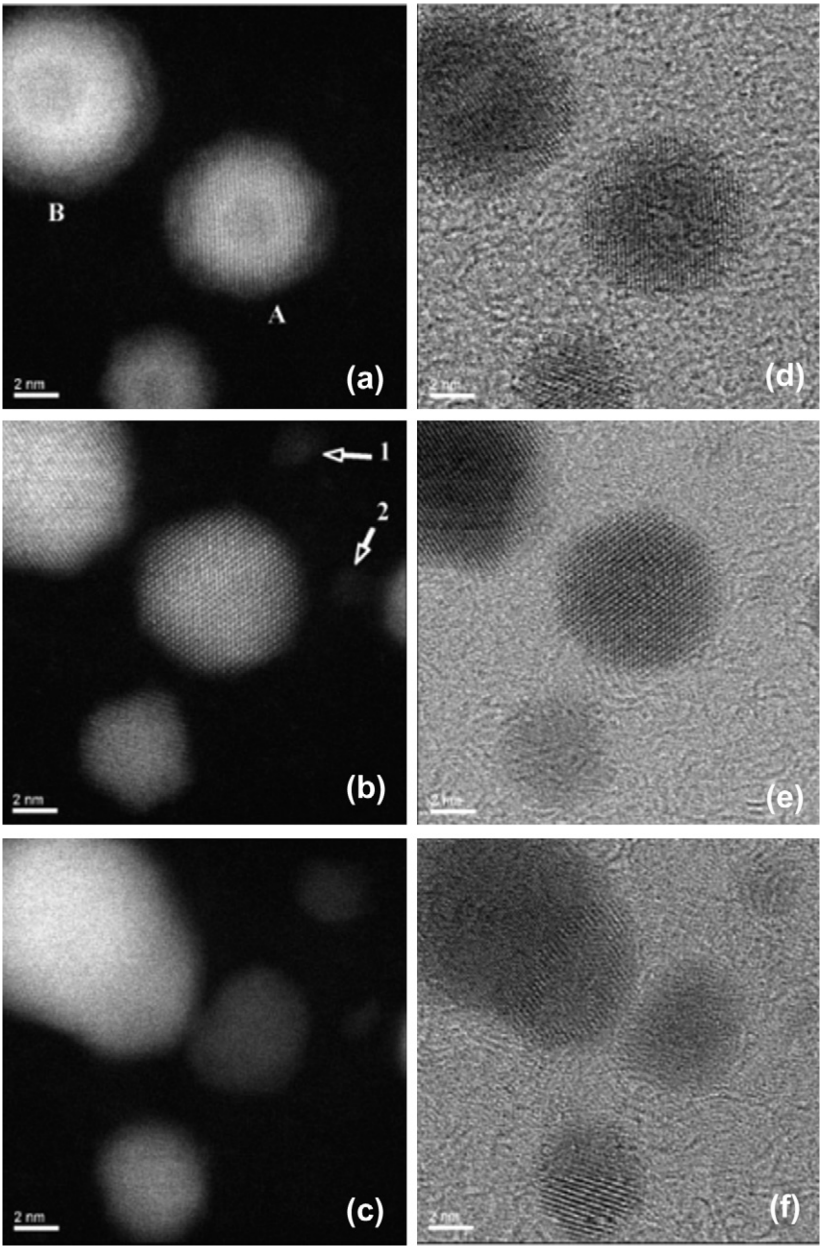
B
A
2 nm
(a)
2 nm
(d)
1
2
2 nm
(b)
2 nm
(e)
2 nm
(c)
2 nm
(f)

Figure 4.32 Series of HAADF and BF image pairs showing heating effects on three-layer Au-Pd particles at 350 °C [(a) and (d)], 550 °C [(b) and (e)], and 700 °C [(c) and (f)]. *(Reprinted with permission from Allard* et al. *(2009). Copyright (2009) Wiley).*

beginning of growth of particle B is apparent, where the new material is not at the same crystal orientation as the original particle, in which the lattice is visible. At 700 °C (Figure 4.32c), particle B shows crystal lattice fringes and is apparently two separate grains. Changes in lattice structure visible from one image to the next are largely the result of slight shifts in orientation of the particles because of the thermal effects (Allard *et al.*, 2009). In the presented example, the clear homogenization of the three-layer gold-pallidium particles was an expected result, explained by a diffusion mechanism. This suggests that a direct diffusive reconstruction of an alloy particle has been directly observed. The reasons for the unexpected failure of two primary particles to sinter but instead to show growth of one particle at the expense of the other have not been well understood. One possibility is that particles acquire some charge during the observations, thereby affecting the surface energy. The growth behavior is reminiscent of Ostwald ripening effects, although the system involves particle behavior on a uniform surface, whereas Ostwald ripening generally involves particle coarsening in solid or liquid solutions.

3.7. Multimetallic Systems

Although bimetallic systems are widely produced and studied for various applications, it may also be possible to form multimetallic nanoparticles under specific experimental conditions by careful control of the experimental parameters. A typical example is the case of multimetallic Pd-Au-FePt. Figure 4.33a and 4.33b show the TEM and HAADF-STEM images of the Pd-Au-FePt nanoparticles. The HAADF-STEM images reveal the darker palladium core and the brighter Au-FePt shells. The thickness of the individual layers themselves are core, pallidium 5 nm; shell, gold 2 nm; and shell FePt 2 nm. EDS line scans reveal the various layers present in the nanoparticle (Figure 4.33c). The EDS line scans also reveal that there is no interatomic diffusion between the gold and FePt layers, proving indeed that the structure is multilayered. The catalytic properties of such systems in the case of the oxygen reduction reaction have been studied and have been shown to have increased tremendously compared to the corresponding monometallic systems (Ding *et al.*, 2012).

3.8. Conclusions

With the advent of aberration-corrected electron microscopy the elucidation of the structure of bimetallic and even multimetallic nanoparticles down

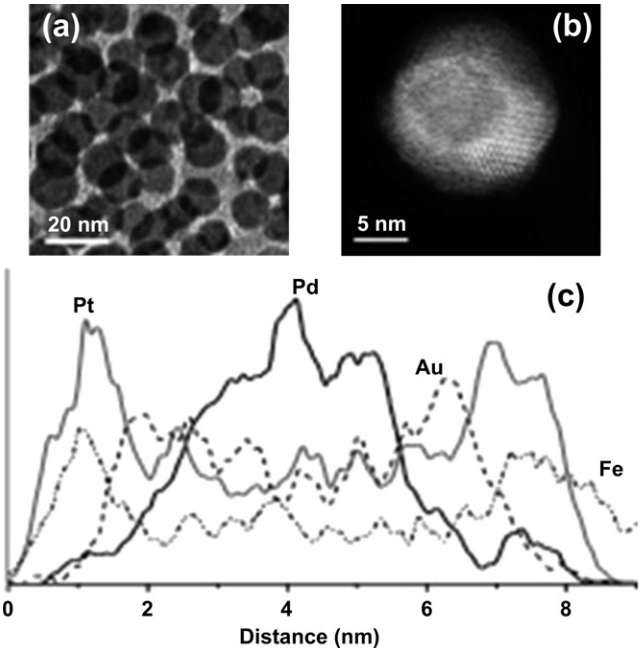

Figure 4.33 (a) TEM and (b) HAADF-STEM image of a single Pd-Au-FePt nanoparticle. (c) High-resolution line scan EDS analysis across the nanoparticle. *(Reprinted with permission from Mazumder* et al. *(2010). Copyright (2010) Wiley).*

to a single atom is now possible. Combined with spectroscopic techniques such as EDS and EELS the information obtained on the structure, stoichiometry, chemical composition, and the nature of core-shell/alloy formation of bimetallic nanoparticles is now unprecedented. More recent and exciting trends based on *in situ* dynamic experiments such as the heating stage studies, definitely promise an exciting future for the case of bimetallic nanoparticles and their enhanced understanding toward various applications including catalysis. It is hoped that with all the intricacies associated with the elucidation of various applications such as catalysis, a realistic progress in this area of research is now truly possible.

4. ELECTRON MICROSCOPY OF LAYERED MATERIALS

4.1. Introduction

Transition metal chalcogenides such as MoS_2 and WS_2 are quasi-2D compounds. Atoms within a layer are bound by strong covalent forces, whereas individual layers are held together by van der Waals interactions. Although a large number of polytypes are observed for the transition metal chalcogenides, the most notable experimentally observed polytypes for MoS_2 and WS_2 based on the stacking sequence of the layers are a hexagonal polymorph with two layers in the unit cell, 2H (P63/mmc) symmetry; rhombohedral with three molecular layers in the unit cell, 3R (R3 m) symmetry; or the less common trigonal with one layer, 1 T. For instance, MoS_2 is a widely used compound with many applications in catalysis and as solid lubricants mainly because of the weak interlayer interaction of the material (Tye and Smith, 2004; Lince, 2004; Wu *et al.*, 2010). More recent applications are hydrogen storage, as host-guest compounds, scanning tunneling microscope tips, and solid-state secondary lithium battery cathodes (Chen *et al.*, 2001; Zak *et al.*, 2002; Remskar *et al.*, 2000; Homyonfer *et al.*, 1997). The most promising and most pursued of all these applications is their use as industrial catalysts for hydrodesulfurization (HDS) of crude oil. Elimination of sulfur from petroleum feedstocks is necessary to meet the severe restrictions on the sulfur concentrations in fuels (Frey *et al.*, 1999; Babich and Moulijn, 2003). The HDS of polyaromatic sulfur compounds or deep HDS is especially difficult for heavy oils containing high concentrations of sulfur (2–3 wt%). Catalysts based on molybdenum sulfide are widely used in oil refineries for the HDS, hydrodenitrogenation (HDN), and hydrodeoxygenation (HDO) reactions of petroleum-derived feedstocks (Song, 2003; Li and Delmon, 1997; Gates, 1992). Because the stringent environmental legislation sets the sulfur level at <15 ppm, new catalysts with significantly improved catalytic performance are being developed. Sulfur compounds that are known to remain in fuels such as diesel at sulfur levels below 500 ppm include dibenzothiophene (DBT) and alkyl-substituted DBTs such as 4,6-dimethyldibenzothiophene (4,6-DMDBT) (Whitehurst *et al.*, 1998; Turaga *et al.*, 2003) and ongoing efforts using different Mo- and W-based catalysts are directed toward removing sulfur. MoS_2 is also combined with other metals, such as cobalt, nickel, and iron, for use in HDS (*Byskov et al.*, 1999).

4.2. MoS_2 Nanowire Catalysts

One of the challenges in working with catalysts is obtaining direct atomic-scale insights to understand their structure better, thereby enabling direct coordination with their activity. For MoS_2-based catalysts this has proved elusive so far since the location of the active sites and their chemical affinity to HDS reactions is poorly understood without atomic-resolution imaging techniques. A solution to this provided is provided with the use of aberration-corrected *(C_s)* STEM-HAADF imaging. HAADF-STEM imaging was performed previously for model MoS_2-based catalysts by Brorson *et al.* (2007). However, the resolution obtained in terms of imaging these catalysts was not sufficient enough (Brorson *et al.*, 2007). Hence probe aberration-corrected STEM imaging has been performed to image MoS_2 nanowire–based catalysts to better understand the atomic structure of these MoS_2–based catalysts. This technique allows the identification of direct atomic locations and hence enhances the understanding of the various catalysts, especially identifying the active sites at which catalysis occurs.

Figure 4.34a shows the HAADF-STEM image of the MoS_2 nanowire catalysts supported on alumina. The MoS_2 nanowire catalysts vary in stacking and range between one and three layers. Also noticeable is that the nanowires appear to be twirled or twisted. The figure shows the filtered image of the MoS_2 catalyst, where the bright atom contrast arises from the Mo atoms in the individual layers of the MoS_2 nanowires. The presence of the sulfur atoms, which show less contrast compared with the molybdenum atoms can be also inferred from the image. Thus the sulfur-molybdenum-sulfur chevron can be identified along the entire length of the nanowire. Measuring the distance between the molybdenum-molybdenum atoms (from the bright atom contrast) shows that they correspond to a distance of 2.7 Å (Figure 4.35b shows the line profile along the length of the entire individual MoS_2 nanowire).

Figure 4.35 shows the MoS_2 nanowires with a helical structure obtained by the twirling or twisting of the individual as well as the double or triple MoS_2 layers. Figures 4.35a and 4.35b show the HAADF-STEM image and the BF-STEM images of these helical MoS_2 catalysts. Figure 4.36c shows the filtered HAADF-STEM image of the MoS_2 catalyst. Interestingly, the catalytically inert basal planes of the nanowires are folded onto themselves to expose the highly active catalytic edge sites (surface atoms seen along the entire length of the nanowire as viewed along the *c*-axis). Figure 4.35d is the line profile corresponding to the interatomic distances of the molybdenum-molybdenum atoms (bright atom contrast), with distances of 2.7 Å between the atoms. The white arrow shows the sulfur atoms that make up the sulfur-molybdenum-sulfur chevron (Deepak *et al.*, 2011b).

Combinated with experimental insights, theoretical simulations have contributed significantly to the fundamental understanding of MoS_2-based catalysts. In the past decade, several reports have focused on the detailed edge structure, location of active sites, slab-size effects (width and thickness),

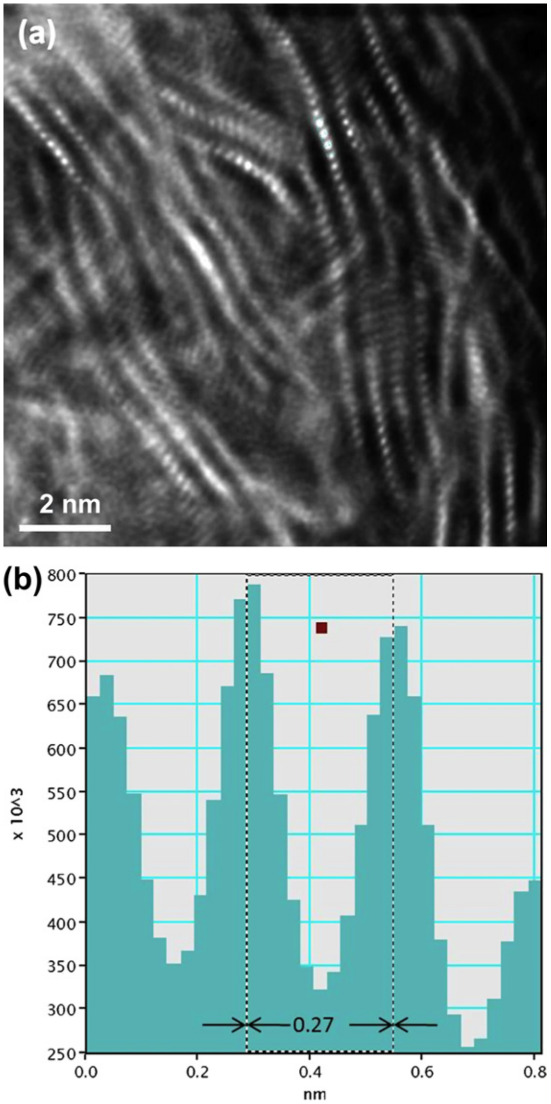

Figure 4.34 MoS_2 nanowire catalysts (on Al_2O_3 support). (a) Filtered HAADF-STEM image of the MoS_2 catalyst. (b) The line profile corresponding to the interatomic distances of the Mo–Mo atoms (bright atom contrast); the distances between the atoms are 2.7 Å. The presence of the sulfur atoms with a lesser contrast can also be seen from the image. *(Reprinted with permission from Deepak* et al. *(2011b). Copyright (2011) Springer).* (See the color plate).

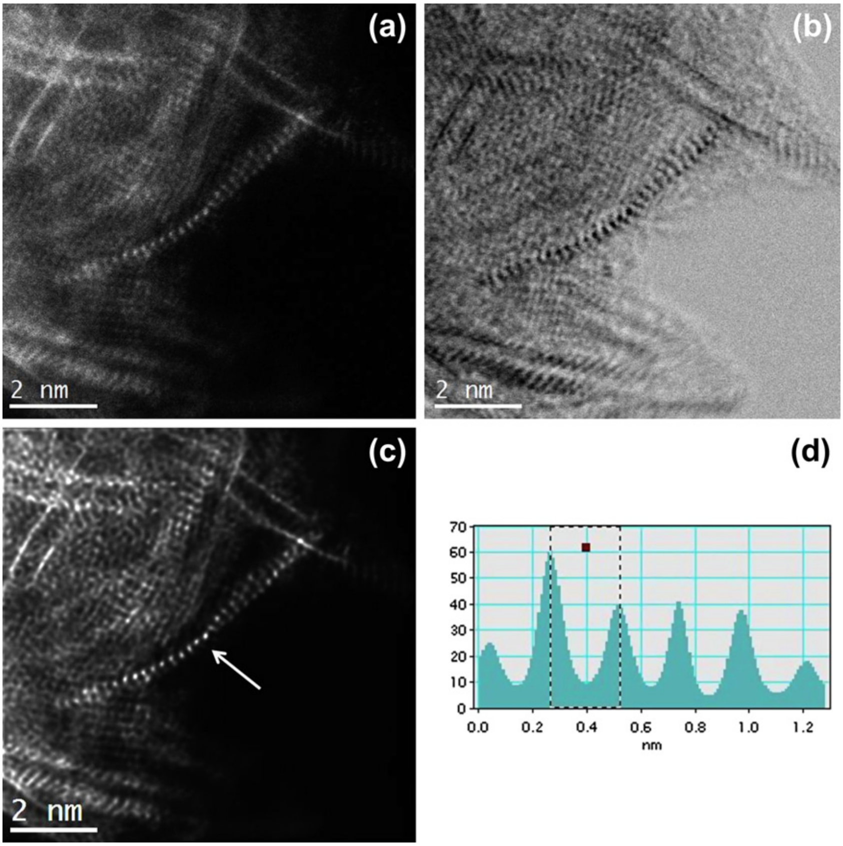

Figure 4.35 MoS_2 nanowire catalysts supported on Al_2O_3. (a) HAADF-STEM image. (b) BF-STEM image of the MoS_2 catalysts. (c) Filtered HAADF-STEM image of the MoS_2 catalyst. (d) The line profile corresponding to the interatomic distances of the Mo–Mo atoms (bright atom contrast), the distances between the atoms are 2.7 Å. The white arrow shows the sulfur atoms that make up the S–Mo–S chevron. *(Reprinted with permission from Deepak* et al. *(2011b). Copyright (2011) Springer).* (See the color plate).

the effect of the hydrogen passivation, the magnetic order edge states, and the vacancies formation (Shidpour and Manteghian, 2010; Li *et al.*, 2008; Ionescu *et al.*, 2003; Iglic *et al.*, 2005). In a majority of these studies, the MoS_2 catalyst has been modeled through MoS_2 sheets where the molybdenum appears in the forms of ions sandwiched by sulfur atoms in a trigonal prismatic coordination. Disregarding the inactive basal plane (0001), the $(10\bar{1}0)$ molybdenum edge (zigzag-terminated morphology) and $(2\bar{1}\bar{1}0)$ Mo–S edge (armchair-terminated morphology) are of particular importance because they contain the "active sites" through the existence of sulfur

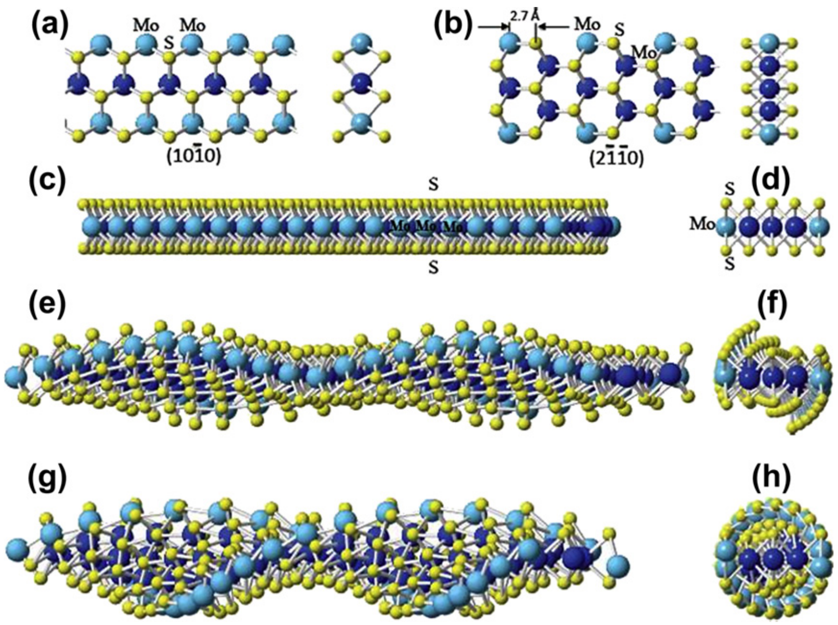

Figure 4.36 (a) and (b) show the side and transversal views of a single-sheet zigzag- and armchair-terminated MoS_2 nanowire. (c) Perspective top and transversal (d) views of an armchair-terminated MoS_2 nanowire similar to (b). (e) and (g) Perspective side views, and (f) and (h) transversal views of a rippled (helical) armchair nanowire. The Mo-edge atoms appear light-colored in the figure compared with the other Mo-atoms (dark-colored). *(Reprinted with permission from Deepak* et al. *(2011b). Copyright (2011) Springer).* (See the color plate).

vacancies. The vacancies on the edges and the intrinsic magnetic order certainly play a key role on the catalytic properties of MoS_2 clusters and nanoribbons. Armchair nanoribbons could be metallic and exhibit a magnetic moment. However, when passivated with hydrogen, they become semiconducting. Zigzag nanoribbons, on the other hand, are metallic and exhibit unusual magnetic properties regardless of their passivation (Botello-Mendez *et al.*, 2009; Shidpour and Manteghian, 2010; Li *et al.*, 2008; Ionescu *et al.*, 2003). It has been suggested that the presence of the vacancies plays a much more substantial role on the magnetization creation, while the magnetic properties can be drastically affected by the size of the nanostructures themselves. In this connection, it must also be noted that electronic properties and edge states in stacked MoS_2 multilayer nanowires and found them to exhibit metallic behavior (Iglic *et al.*, 2005). State-of-the-art simulations indicate that the existence of the metallic edge states seems to be crucial in order to raise the catalytic activity of MoS_2 nanostructures. Iglic *et al.* (2005) have proposed the possibility of MoS_2 structures with helical and twisted morphologies but did not study their electronic or magnetic properties or consider them of importance because of its unproven existence in nature so far (Kralj-Iglic *et al.*, 2004). Thus, the presence of rippled and twisted or helical morphologies of MoS_2 has not been observed previously (Iglic *et al.*, 2005; Kralj-Iglic *et al.*, 2004; Kisielowski *et al.*, 2011), and advanced electron microscopic techniques have been used until recently to image such catalyst systems with unprecedented structural details (Hansen *et al.*, 2011; Galvan *et al.*, 2011).

Based on the HAADF-STEM images, various atomic models were built to illustrate the different morphologies found in the experimentally observed MoS_2 catalysts discussed previously. Figures 4.36a and 4.36b show the side and transversal views of zizzag- and armchair-terminated MoS_2 sheets, respectively. It has been shown that the $[\bar{1}0\bar{1}0]$ edge plane is more stable than the $[2\bar{1}\bar{1}0]$ edge plane. However, according to the experimental images, the molybdenum atoms are aligned along the $[2\bar{1}\bar{1}0]$ direction, a characteristic that it is possible only for an armchair-terminated slab. For this reason, the first model corresponds to a single-layer armchair-terminated MoS_2 nanowire. Figures 4.36 a-d show different views of an armchair nanowire consisting of a five–atomic layer S–Mo–S sandwich. The relative distance between the molybdenum edge atoms in our model is 2.7 Å, very similar to the experimental value. The experimentally observed nanowires are found mostly in bundles with thicknesses ranging from two to eight single-sheet MoS_2 layers, a varying width ranging from two to six atomic layers, and a length ranging from 20 to 50 nm. The slightly distorted quasi-planar nanowire structures appear to be stabilized by the neighboring layers and are configured almost as in the bulk, with a distance between the single-sheet layers ranging from 5.3 to 6.2 Å. In some bundles the bending/tilting of some nanowires is observed, a fact that leads to a second model. Figures 4.36e and 36f show a perspective and transversal view of a rippled nanowire. These nanostructures are indeed considerably elongated and can also be found in bundles or isolated (Figure 4.36a). In contrast with the previous model, the distances between the edges of two neighboring nanowires is affected by the tilting and therefore are not uniform. Interestingly, the distance between the axes of two neighboring rippled nanowires is nearly the same as for the flat nanowires. When the bending of the nanowires is more pronounced, we observed the irregular twisting of the MoS_2 nanostructures. Figures 4.36 g and 4.36 h show a perspective and transversal view of the third experimentally observed morphology that corresponds to a helical or twisted nanowire. Indeed, some of the distorted nanowires are a mixture between the rippled and the helical ones. DFT calculations of the electronic structure of the MoS_2 spirals suggest that the twisting produces a transition from semiconductor to semimetal behavior. This effect could be attributed to a distortion produced by the rotation applied to the nanowire; due to this the MoS_2 spirals should have improved catalytic activity. The existence of this new atomic structure changes completely the landscape of the location of the catalytically active sites, opening up the possibility for new MoS_2-based nanocatalysts (Galvan *et al.*, 2011).

4.3. Co-Doped MoS_2/WS_2 Nanowire Catalysts

While unpromoted MoS_2 (WS_2) catalysts do not possess high catalytic activity, a very significant increase in their activity can be achieved by adding cobalt or nickel. The use of metal nanoparticles in HDS reactions has been studied by incorporating a variety of transition metals, such as molybdenum, nickel, Ni/Fe, Ni/W, Mo/W, and Mo/Co, which are able to hydrodesulfurize thiophene and DBT in good yields (Yoosuk *et al.*, 2008; Senevirathne *et al.*, 2007; Escalona *et al.*, 2006; Olivas *et al.*, 2006; Dhas and Suslick, 2005; Farraghher, 1979). Of particular interest is the case of Co-promoted MoS_2/WS_2–supported catalysts. Several investigations have been directed toward understanding the nature and function of the Co-promoter atoms in MoS_2/WS_2–based catalysts. The difficulty for many years was to understand in detail the catalytic properties of the different types of cobalt-molybdenum-sulfur structures since direct atom-resolved insight was not available previously. Techniques such as extended X-ray absorption fine structure and X-ray photoelectron spectroscopy have been used to obtain information on the promoter atoms (example: Ni/Co) incorporated within the catalysts previously (example: MoS_2/WS_2 on Al_2O_3). Only recently has such insight provided by scanning tunneling microscopy along with density functional theory; this has contributed greatly to improve fundamental knowledge of the MoS_2 and cobalt-molybdenum-sulfur catalyst structures (Topsøe, 2007). A direct solution to this is now provided using aberration-corrected HAADF-STEM imaging, which can be used to image individual cobalt atoms present in the lattice of MoS_2/WS_2 nanowire catalysts directly. The identification is also supported by performing atomic-resolution energy dispersive X-ray analysis (STEM-EDAX), which can provide reliable and precise chemical

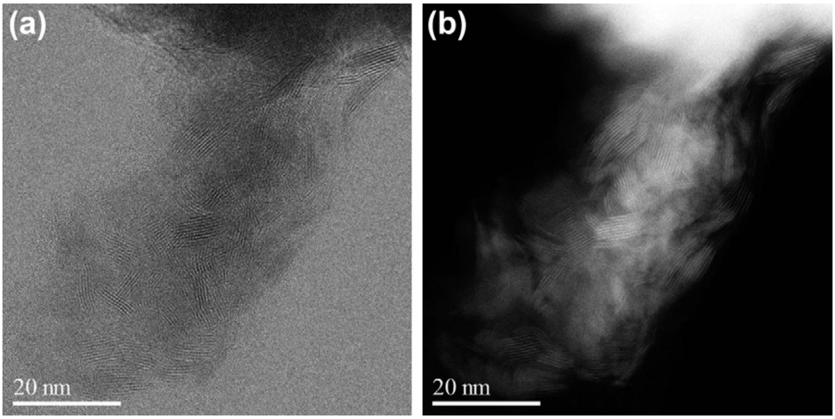

Figure 4.37 (a) and (b) show the low-magnification BF-STEM and HAADF-STEM images of the Co-doped MoS_2 nanowire catalysts. *(Reprinted with permission from Deepak* et al. *(2011b). Copyright (2011) Springer).*

information to distinguish the presence of the individual promoter/dopant atoms in the lattice of the host (Deepak *et al.*, 2011c). Figures 4.37a and 4.37b show the low-magnification BF-STEM and HAADF-STEM images of the Co-doped MoS_2 nanowire catalysts.

A closer look at the nanowires is provided by the high-resolution STEM images in Figure 4.38. Figures 4.38a and 4.38b show the BF-STEM and HAADF-STEM images of the Co-doped MoS_2 nanowires. Interesting variations in the atomic spacing are revealed from the image (Figure 4.39b) and the line profile (Figure 4.38c) drawn along the row of the bright atomic columns. The spacing between the atoms varies from 2.34 Å (±0.1 Å) to 2.7 Å (±0.1 Å) (atoms A and B vs. B and C) (bright atom contrast revealing the molybdenum-cobalt-molybdenum interatomic distances). The final molybdenum-molybdenum interatomic distance is 2.70 Å (±0.1 Å) (atoms C and D). This is indeed interesting and can be explained in terms of the substitution of cobalt into the lattice of molybdenum, occupying the molybdenum sites. In addition, the difference in the atom contrast (between molybdenum and cobalt, Figure 4.39b), which decreases upon going from the Mo → Co and subsequently increases from Co → Mo, is also notable. The interlayer distance as measured from the line profile of the individual layers is 5.84 Å. The variations on the HAADF contrast cannot be explained on the basis of thickness changes. Therefore, the most important contributions should originate from compositional variations, revealed by the difference in atomic number (Z) that exists among molybdenum (atomic number = 42) and cobalt (atomic number = 27) (HAADF intensity is

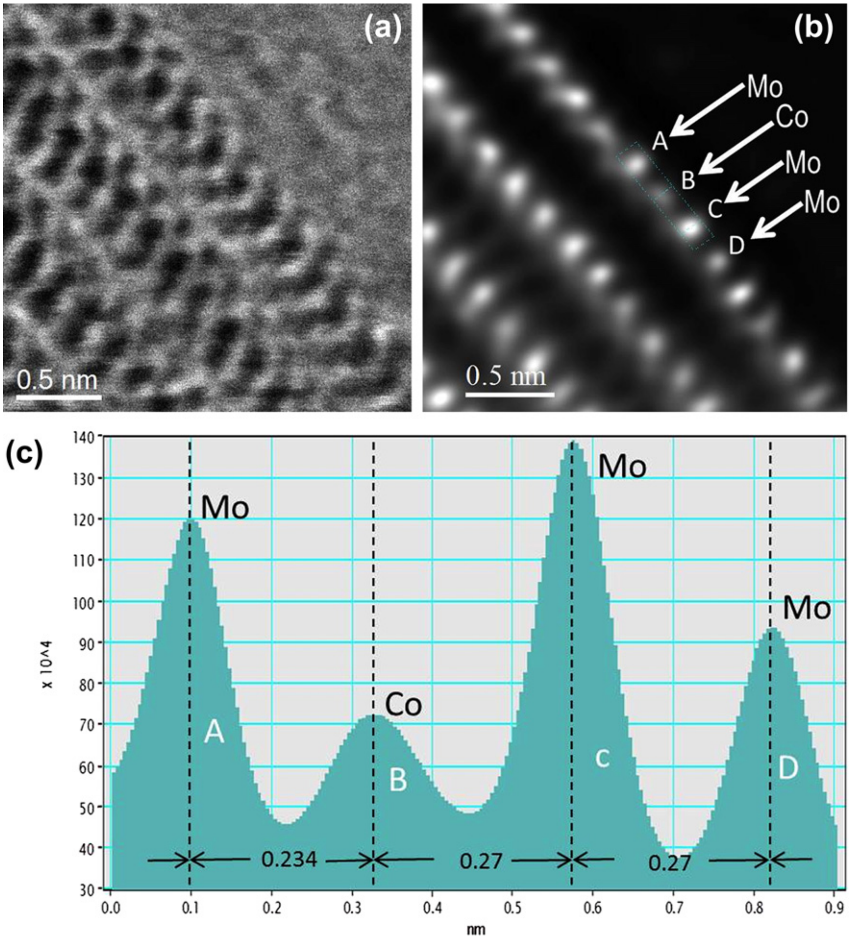

Figure 4.38 (a) and (b) BF-STEM and HAADF-STEM images of the Co-doped MoS_2 nanowire catalysts (unsupported catalyst). (c) Corresponding line profiles. The spacing between the Mo → Co → Mo → Mo atoms as revealed by the line profile is 2.34 Å ± 0.1 Å (Mo-Co); 2.7 Å ± 0.1 Å (Co-Mo); and 2.7 Å ± 0.1 Å (Mo-Mo) (atoms A-B-C-D). The cobalt atoms have a lesser intensity compared the molybdenum atoms as a consequence of the difference in their respective atomic numbers. *(Reprinted with permission from Deepak* et al. *(2011b). Copyright (2011) Springer).* (See the color plate).

considered to be proportional to $Z^{1.7}$). Finally, it should be noted that in between the layers, the presence of the sulfur atoms that make up the sulfur-molybdenum-sulfur structure can be inferred from their lighter contrast compared with the brighter Mo and Co atoms. Figures 39a and 39b shows the low-magnification BF-STEM and HAADF-STEM images of the

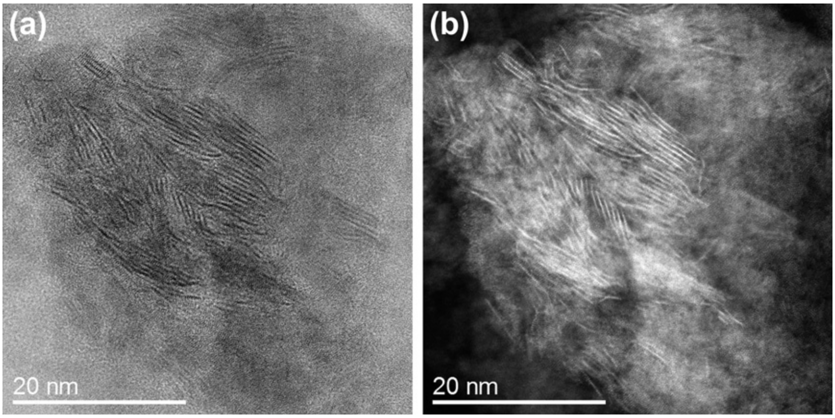

Figure 4.39 *(*a) and (b) Low-magnification BF-STEM and HAADF-STEM images of the Co-doped WS_2 nanowire catalysts supported on alumina. *(Reprinted with permission from* Deepak et al. *(2011b). Copyright (2011) Springer).*

Co-doped WS_2 nanowire catalysts supported on alumina. Large amounts of the nanowires can be clearly seen in the images.

Figure 4.40 shows the high-resolution BF-STEM and HAADF-STEM images of the Co-doped WS_2 nanowire catalyst. Variations in the interatomic spacing are observed from the image (Figure 4.40b) and the line profile (Figure 4.40c) drawn along the row of the bright atomic columns. The spacing between the atoms varies as follows: 2.24 Å (±0.1 Å for spacing A-B), −2.72 Å (±0.1 Å) for spacing B-C, −2.72 Å (±0.1 Å) for spacing C-D, and −2.24 Å (±0.1 Å) for spacing D-E.

This variation in the interatomic distances can be explained in terms of the substitution of cobalt in the lattice of tungsten (akin to the case of cobalt atoms substituting molybdenum as explained above). In addition, the difference in the atom contrast (between tungsten and cobalt (Figure 4.41b) atoms W-Co-W-Co-W [A-B-C-D-E]) can be noted. The variations are due to the difference in atomic number (Z) between tungsten (atomic number = 74) and cobalt (atomic number = 27). Also, the intensity variations in the HAADF line scans is dependent on the thickness of the atomic layers themselves (whether it is one, two, or three layers). This is also the reason that the Mo/W bright atom contrast appears elongated (two or more layers are twirled and hence produce this type of effects; see for example Figure 4.40b [for the Co:WS_2 case] and Figure 4.40b [for the Co:MoS_2 case], where this entanglement of the WS_2/MoS_2 layers can be clearly seen).

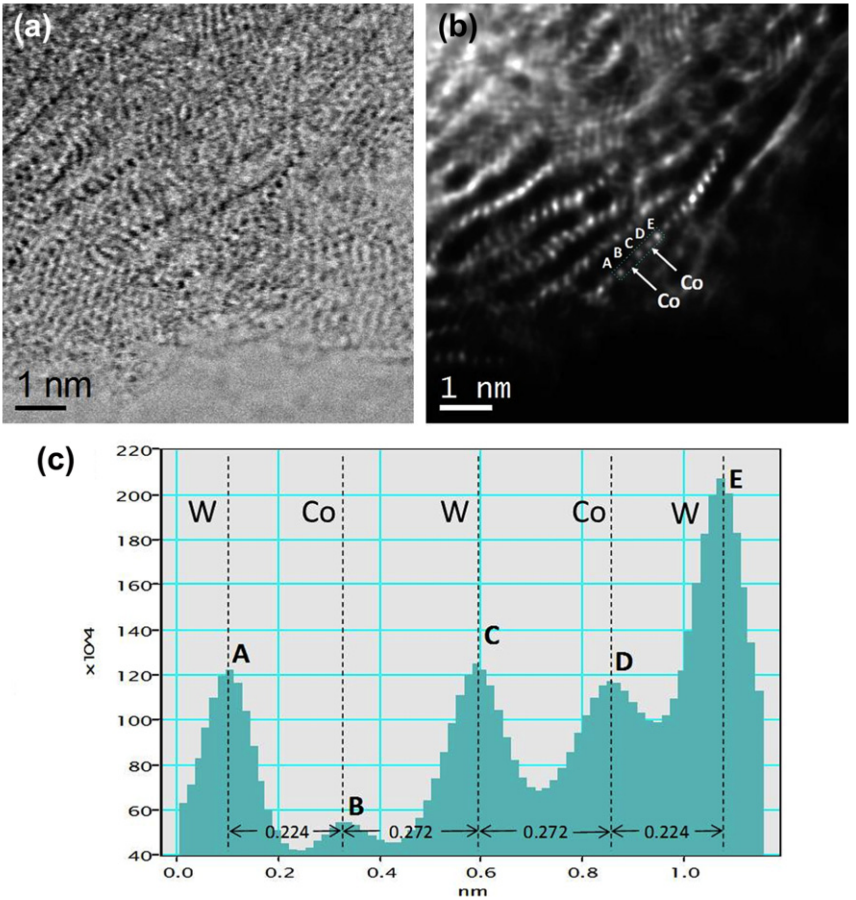

Figure 4.40 (a) and (b), BF-STEM and HAADF-STEM images of the Co-doped WS_2 nanowire catalysts (supported on Al_2O_3) and (c) corresponding line profiles. The spacing between the W-Co-W-Co-W atoms as revealed by the line profile is 2.24 ± 0.1 Å (W-Co), 2.72 ± 0.1 Å (Co-W), 2.72 ± 0.1 Å (W-Co), 2.24 ± 0.1 Å (Co-W), (atoms A → B → C → D → E). The Co atoms have a lesser intensity in comparison with the W atoms because of the difference in their respective atomic numbers. *(Reprinted with permission from Deepak* et al. *(2011b). Copyright (2011) Springer).* (See the color plate).

Figure 4.41b shows the EDAX line scan for one of the individual Co-doped WS_2 nanowires (the image is shown in Figure 4.41a). The characteristic W (M) and the Co (K) signals are obtained from the line scans indicating the presence of tungsten and cobalt in the individual WS_2 nanowire (cobalt incorporated at the tungsten sites). The EDAX spectra thus support the previous HAADF-STEM observations that cobalt is indeed present in the lattice of WS_2. The identification of cobalt present uniformly

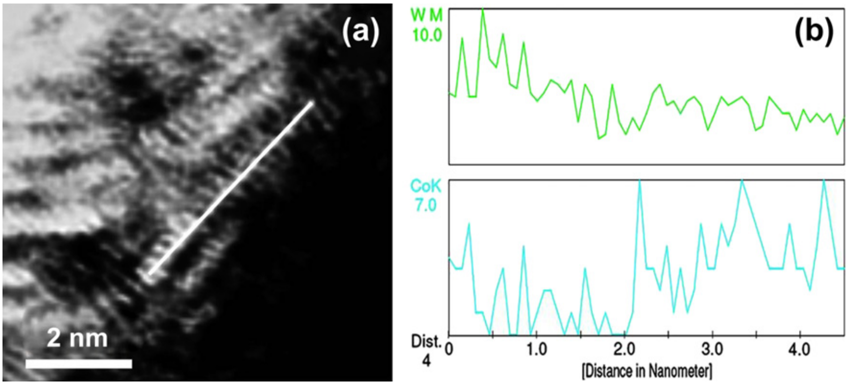

Figure 4.41 EDAX line scans carried out on an individual Co-doped WS_2 nanowire catalyst. The presence of the characteristic and distinct signals of W (M) and Co (K) have been identified from the line scan (Co present at the W-sites). *(Reprinted with permission from Deepak* et al. *(2011b). Copyright (2011) Springer).* (See the color plate).

throughout the WS_2 catalysts was ascertained by EDAX spectra and line scans over the entire catalyst in order to eliminate CoS_2 as a possible secondary phase and conclude that cobalt is indeed present only as a dopant in the MoS_2/WS_2 systems studied here.

MoS_2 is a layered material consisting of weakly bounded sulfur-molybdenum-sulfur sheets and a single layer can be terminated by two different edges: the molybdenum-terminated edge $(10\bar{1}0)$ (Mo-edge) and the sulfur-terminated $(\bar{1}010)$ edge (S-edge). The Mo-edge exposes a row of molybdenum atoms with a coordination of only four sulfur atoms. The S-edge corresponds to an edge where the Mo atoms are fully saturated with sulfur atoms. Density functional theory calculations concentrate on the adsorption of sulfur on the molybdenum-terminated edges and the formation of vacancies on the sulfur-terminated edges to investigate the nature of the catalytic properties of MoS_2 (Byskov *et al.*, 1997; Raybaud, 2000). In the past two decades, numerous configurations for the sulfulr-adsorption and the cobalt-promoter distribution at the molybdenum and sulfur active edges of MoS_2 have been intensively investigated by different theoretical and experimental groups. One of the most relevant density functional theory simulation results shows that, for typical HDS conditions, the energy of the S-edge with 100% cobalt is lower than the Mo-edge with 100% cobalt (Krebs *et al.*, 2009; Schweiger *et al.*, 2002; Byskov *et al.*, 2000; Sun *et al.*, 2004a). However, in addition to the affinity of cobalt for the S-edge under such reaction conditions, a 50% cobalt-promoter decoration of the Mo-edge reduces considerably the edge energy of the Mo-edge to a value close to the S-edge value. Such a new feature had important consequences on the morphologies considered to date and opened a new landscape of possibilities on the location and nature of active sites at the edges of the Co/Mo/S phase. In particular, density functional theory calculations showed that the 50% cobalt partial occupation with the Mo-edge covered by 25% sulfur is stable. Furthermore, the simulations also indicated the existence of two configurations with such sulfur saturation that are close in energy—namely, the alternate configuration Mo-Co-Mo-Co- and the paired configuration Mo-Mo-Co-Co. Figures 4.42a and 4.42b show a perspective view of these configurations together with their respective top views of the Mo-edge. In both cases, the Mo-edge structure exhibits mixed

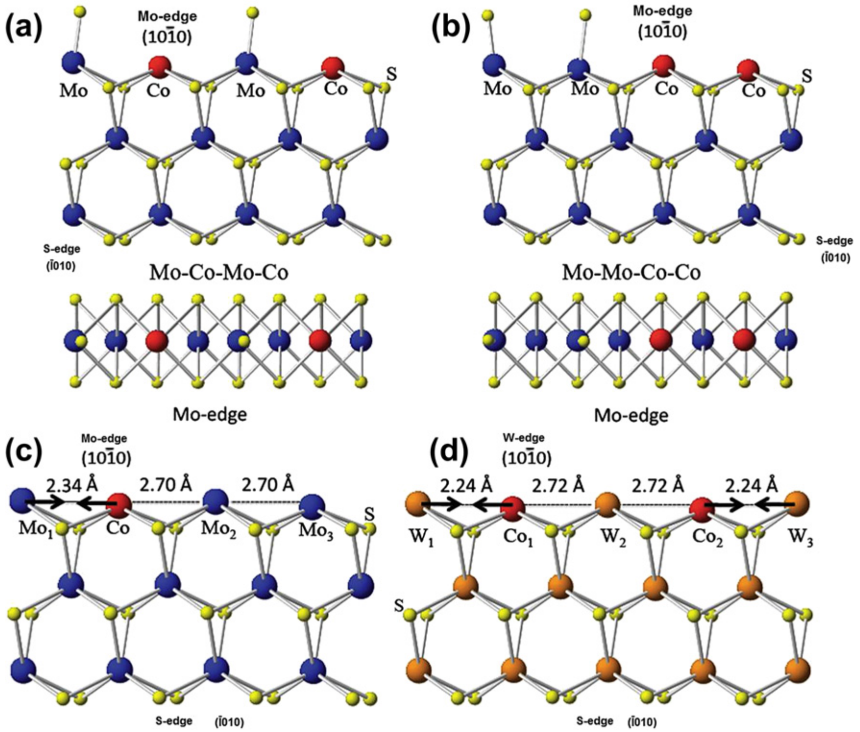
(a)
Mo-edge
$(10\bar{1}0)$
Mo
Co
Mo
Co
S
S-edge
$(\bar{1}010)$
Mo-Co-Mo-Co
Mo-edge
(b)
Mo-edge
$(10\bar{1}0)$
Mo
Mo
Co
Co
S
S-edge
$(\bar{1}010)$
Mo-Mo-Co-Co
Mo-edge
(c)
Mo-edge
$(10\bar{1}0)$
2.34 Å
2.70 Å
2.70 Å
Mo_1
Co
Mo_2
Mo_3
S
S-edge $(\bar{1}010)$
(d)
W-edge
$(10\bar{1}0)$
2.24 Å
2.72 Å
2.72 Å
2.24 Å
W_1
Co_1
W_2
Co_2
W_3
S
S-edge $(\bar{1}010)$

Figure 4.42 Perspective and top views of (a) Mo-edge with 50% cobalt in an alternate position and 25% sulfur. (b) Mo-edge with 50% cobalt in a pairing configuration and 25% sulfur. (c) and (d) Perspective views of CoMoS (CoWS) structure for the experimentally observed Mo-Co-Mo-Mo (W-Co-W-Co-W) sequence at the Mo/W-edge. Molybdenum atoms are in blue, tungsten ornaments are in orange, and sulfur atoms are in yellow. *(Reprinted with permission from Deepak* et al. *(2011b). Copyright (2011) Springer).* (See the color plate).

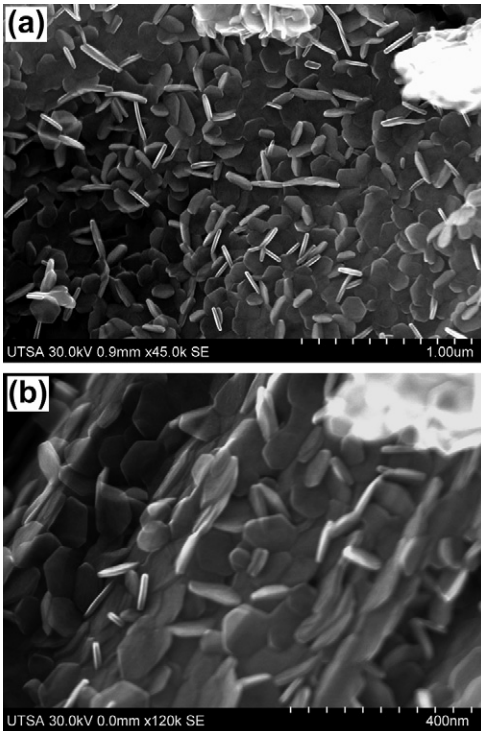

Figure 4.43 SEM micrographs of the MoS_2 plates. *(Reprinted with permission from Castro-Gerrero* et al. *(2011). Copyright (2011) Royal Society of Chemistry).*

Co-Mo sites while the sulfur atom is located at the top of the molybdenum atoms. Nevertheless, it was also found that sulfur atoms might also be located in bridging positions, which indicated that the mobility of sulfur atoms on the Mo-edge is high (Krebs *et al.*, 2009; Schweiger *et al.*, 2002). To illustrate the experimentally observed morphologies, two models for the cobalt-molybdenum-sulfur and cobalt-tungsten-sulfur catalysts were built (see Figures 4.42c and 4.42d). Figure 4.42c shows the atomic model for the MoS_2 doped with cobalt for the experimentally found –Mo-Co-Mo-Mo- sequence indicated previously in Figure 4.39b. In contrast to the simulations, where the optimized local cobalt-molybdenum distances are comprised between 2.74 Å and 2.84 Å, the pairing of the Mo_1- and Co_1-edge atoms (2.34 Å) is observed, followed by a 2.70-Å separation for both Co_1-Mo_2 and Mo_2-Mo_3 atoms. Interestingly, this structure appears to be a combination of the alternate and paired configuration, which are both very close in energy. The 100% cobalt–50% sulfur and 100% cobalt–62.5% sulfur configuration at the S-edge (not shown) were not experimentally observed. Figure 4.42d shows the atomic model for the cobalt-tungsten-sulfur catalysts for the W-Co-W-Co-W sequence presented in Figure 4.40. This model supports the idea that the cobalt-promoter atoms incorporate into the MoS_2 structure by substituting Mo-edge atoms in an alternating configuration as previously mentioned. Previous density functional theory calculations indicate that under reaction conditions, 50% S coverage on the promoted W-edge and S-edge are the most energetically stable configurations. In contrast to the CoMoS model, the sulfur atoms are located at the bridging positions according to Sun *et al.* (2004b). Additional density functional theory calculations are desirable to reveal in detail the sulfur-saturation configuration at the W-edge. In general, the exact location of the sulfur atoms, and as a consequence the location of the active edges, remains an issue at the experimental level since it is not yet possible to distinguish between 25% or 50% of sulfur saturation at the Mo-edge when sulfur atoms are located on top of the Mo-edge atoms.

4.4. MoS_2 Nanoplates

Of the various morphologies of MoS_2 explored for its catalytic applications, an interesting morphology is the platelike structure. Nanohexagonal plates are particularly exciting because of the hexagonal shape and nanometric scale, which make them an ideal material in catalysis due to their high surface area. Figure 4.44 shows the SEM micrographs of the MoS_2 plates synthesized at 700 °C and further annealed at 900 °C and 1000 °C. Both images show the presence of hexagonal plates with nanometric size in the sample. The size of the plates is approximately 30–35 nm in diameter. The agglomerates consist of individual plates stacked together.

Figure 4.44a presents an ultra–high-resolution BF-STEM image of a single MoS_2 nanoplate. The Mo–Mo distances in the a_1, a_2, and a_3 directions are measured as 2.76 Å, 2.8 Å, and 2.87 Å (the line profile is shown in the inset); these distances correspond to the Mo–Mo interatomic distances (bright atom contrast arising from the molybdenum atoms). Figure 4.44b shows the electron diffraction pattern revealing the a_1, a_2, and a_3 directions as well as the hexagonal structure of the MoS_2.

Figure 4.45 shows a moiré pattern formed by the superimposition of the individual plates of MoS_2. The upper inset in the figure shows an HR-TEM micrograph wherein a moiré pattern of a moiré lattice is observed. The lower inset shows the fast Fourier transform (FFT) of the plates: Three sets of hexagonal spots can be seen, corresponding to the three individual plates.

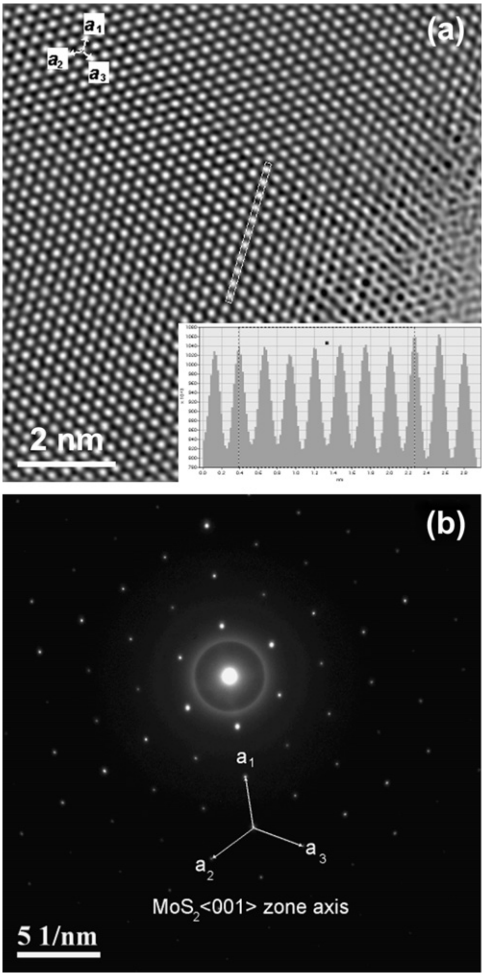

Figure 4.44 (a) BF-STEM image of a MoS_2 plate (bright atom contrast shows the molybdenum atoms). The insets show the a_1, a_2, and a_3 directions in the sixfold zone axis as well as the measurements of the Mo–Mo interatomic distances. (b) Selected area electron diffraction pattern of the MoS_2 plates showing the hexagonal symmetry in the <001> direction. *(Reprinted with permission from Castro-Gerrero et al. (2011). Copyright (2011) Royal Society of Chemistry).*

The angles measured between the plates correspond to 19° between the first two plates and 16° between the next two plates; these are the rotational angles of the plates. A moiré pattern is observed with the superimposition of the three plates. Moiré patterns of three plates (see the boxed area, plate 3) and two plates (plate 2) are seen in the figure.

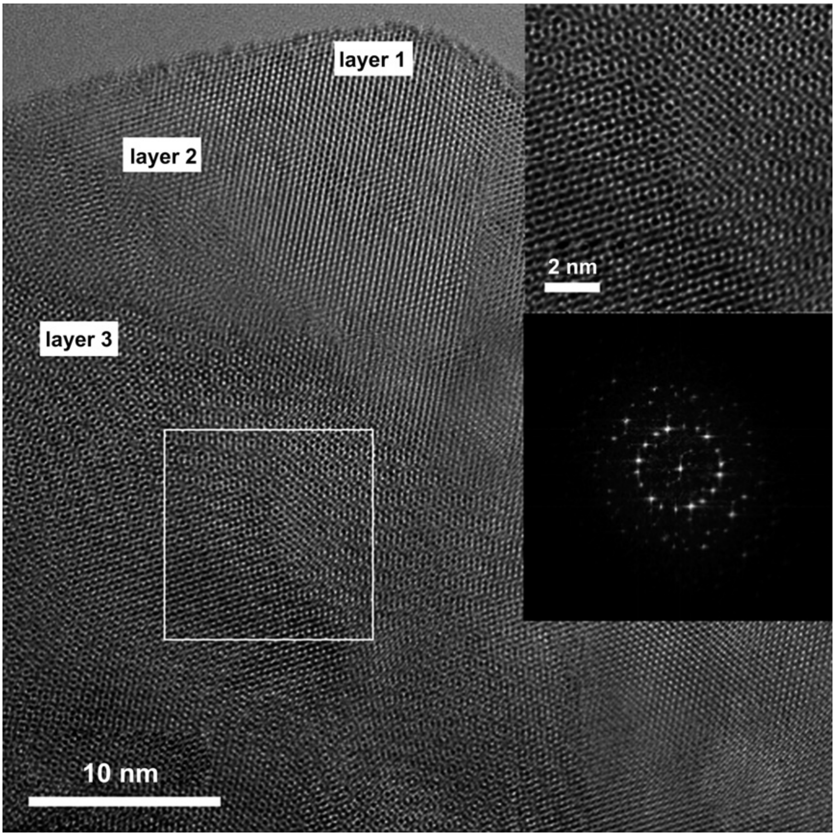

Figure 4.45 Image showing the superimposition of three plates of MoS_2 and the formation of a moiré pattern. The upper inset shows moiré lattice. The lower inset shows the fast Fouriter transform pattern with three sets of spots corresponding to the three plates, the angles between the plates being 19° and 16°. *(Reprinted with permission from* Castro-Gerrero et al. *(2011). Copyright (2011) Royal Society of Chemistry).*

Figure 4.46 shows an HR-TEM micrograph of a MoS_2 plate showing a lateral view. The left inset shows the diffraction pattern revealing the direction of the crystal, which is [000*n*], where *n* is even. The right inset shows an amplification of the boxed area in the main image. It Several bands of different sizes can be observed; the broad lines are molybdenum (as it has a high atomic number and a high atomic weight), whereas the thin lines are sulfur. The lines are regular and consist of alternating sulfur-molybdenum-sulfur layers forming a sandwich. These sulfur-molybdenum-sulfur layers form the unit cell in MoS_2 (seen in the inset). The distance measured

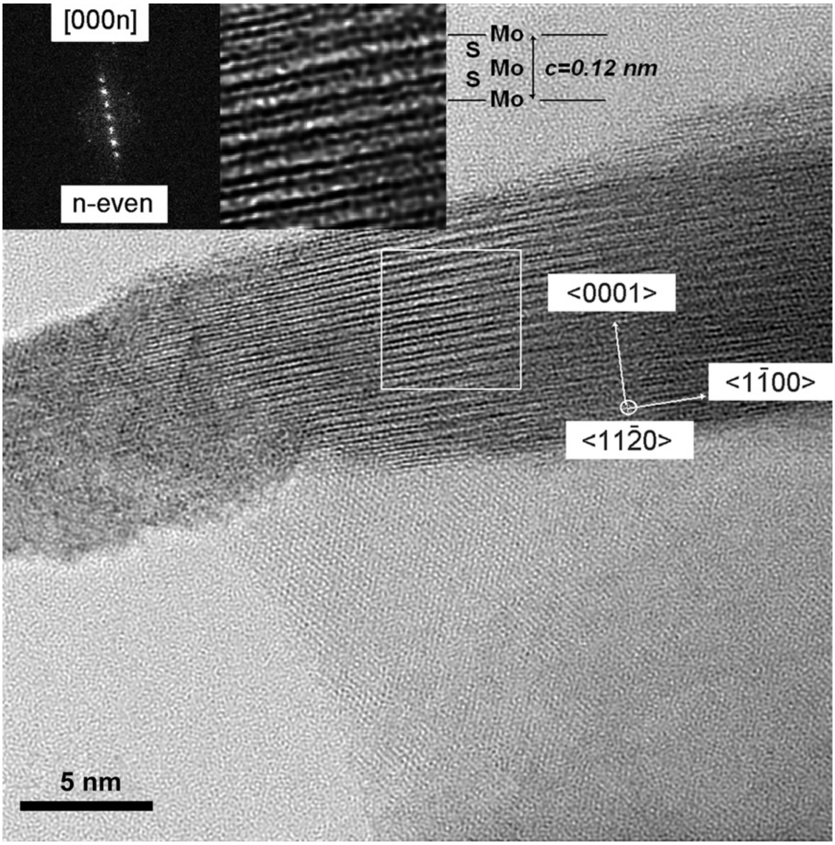

Figure 4.46 BF-STEM image of a plate showing the individual molybdenum and sulfur layers in MoS_2. The left inset shows the fast Fourier transform in the <11-20> zone axis, whereas the right inset shows a magnified view of the unit cell (c = 1.2 Å). The individual stripes are the stacks of molybdenum and sulfur. *(Reprinted with permission from Castro-Gerrero* et al. *(2011). Copyright (2011) Royal Society of Chemistry).*

between three atoms of molybdenum forming the cell unit shows c = 1.2 Å, which agrees with the values obtained with X-ray diffraction (reported value of c/2 = 6.53 Å).

4.5. Conclusions

Elucidation of the structure and properties associated with a truly industrial catalyst such as MoS_2 based on the recent advances in advanced electron microscopy promises to open new avenues in this ever-expanding area of catalysis of layered materials. Having overcome the shortcomings of the lack of understanding of structure and catalytic active sites associated with such catalysts before such techniques were available, the future seems quite promising in this area. Indeed, the challenges associated with solving environmental issues based on catalysis are more realistic and closer than ever before.

ACKNOWLEDGMENTS

This work was supported by grants from the National Center for Research Resources (grant No. 5 G12RR013646-12) and the National Institute on Minority Health and Health Disparities from the National Institutes of Health (grant No. G12MD007591). The authors would also like to acknowledge National Science Foundation support (DMR grant No. 1103730, "Alloys at the Nanoscale: The Case of Nanoparticles, Second Phase" and PREM grant No. 0934218, "Oxide and Metal Nanoparticles—The Interface Between Life Sciences and Physical Sciences". In addition, the authors would like to acknowledge the support of the Welch Foundation (grant No. AX-1615, "Controlling the Shape and Particles Using Wet Chemistry Methods: The Case of Bimetallic Nanoparticles", an international collaboration grant from University of California Institute for Mexico and the United States (UC MEXUS), and the Consejo Nacional de Ciencia y Tecnología (CONACYT, grant CIAM 148967). In addition, authors want to thank to Dr. Gabriela Diaz from Institute of Physics-UNAM for provide the samples Au/Ir/TiO2 included in the present Chapter.

REFERENCES

Ahmed, F., Alam, M. K., Suzuki, A., Koyama, M., Tsuboi, H., Hatakeyama, N., Endou, A., Takaba, H., Del Carpio, C. A., Kubo, M., et al. (2009). Dynamics of hydrogen spillover on Pt/γ-Al_2O_3 catalyst surface: a quantum chemical molecular dynamics study. *Journal of Physical Chemistry C, 113*(35), 15676–15683.

Allard, L. F., Bigelow, W. C., Jose-Yacaman, M., et al. (2009). A new MEMS-based system for ultra-high-resolution imaging at elevated temperatures. *Microscopy Research and Technique, 72*, 208–215.

Babich, I. V., & Moulijn, J. A. (2003). Science and technology of novel processes for deep desulfurization of oil refinery streams: a review. *Fuel, 82*(6), 607–631.

Botello-Mendez, A. R., Lopez-Urias, F., Terrones, M., et al. (2009). Metallic and ferromagnetic edges in molybdenum disulfide nanoribbons. *Nanotechnology, 20*(32), 1–6.

Brorson, M., Carlsson, A., & Topsoe, H. (2007). The morphology of MoS_2, WS_2, Co–Mo–S, Ni–Mo–S and Ni–W–S nanoclusters in hydrodesulfurization catalysts revealed by HAADF-STEM. *Catalysis Today, 123*(1-4), 31–36.

Byskov, L. S., Hammer, B., Nørskov, J. L., et al. (1997). Sulfur bonding in MoS_2 and Co-Mo-S structures. *Catalysis Letters, 47*(3-4), 177–182.

Byskov, L. S., Nørskov, J. K., Clausen, B. S., et al. (1999). DFT calculations of unpromoted and promoted MoS_2-based hydrodesulfurization catalysts. *Journal of Catalysis, 187*(1), 109–122.

Byskov, L. S., Nørskov, J. K., Clausen, B. S., et al. (2000). Edge termination of MoS_2 and CoMoS catalyst particles. *Catalysis Letters, 64*(2-4), 95–99.

Carter, C. B., & Williams, D. B. (2009). *Transmission Electron Microscopy: A Textbook for Materials Science*. New York: Springer.

Castro-Guerrero, C. F., Deepak, F. L., Ponce, A., et al. (2011). Structure and catalytic properties of hexagonal molybdenum disulfide nanoplates. *Catalysis Science & Technology, 1*, 1024–1031.

Chen, J., Kuriyama, N., Yuan, H., et al. (2001). Electrochemical hydrogen storage in MoS_2 nanotubes. *Journal of the American Chemical Society, 123*(47), 11813–11814.

Corthey, G., Giovanetti, L. J., Ramallo-López, J. M., et al. (2010). Synthesis and characterization of gold at gold(i)−thiomalate core at shell nanoparticles. *ACS Nano, 4*, 3413–3421.

Deepak, F. L., Casillas-Garcia, G., Esparza, R., et al. (2011a). New insights into the structure of Pd–Au nanoparticles as revealed by aberration-corrected STEM. *Journal of Crystal Growth, 325*(1), 60–67.

Deepak, F. L., Esparza, R., & Borges, B. (2011b). Rippled and helical MoS_2 nanowire catalysts: an aberration corrected STEM study. *Catalysis Letters, 141*(4), 518–524.

Deepak, F. L., Esparza, R., Borges, B., et al. (2011c). Direct imaging and identification of individual dopant atoms in MoS_2 and WS_2 catalysts by aberration corrected. Scanning transmission electron microscopy. *ACS Catalysis, 1*(5), 537–543.

Dhas, N. A., & Suslick, K. S. (2005). Sonochemical preparation of hollow nanospheres and hollow nanocrystals. *Journal of American Chemical Society, 127*(8), 2368–2369.

Diebol, U. (2003). The surface science of titanium dioxide. *Surface Science Reports, 48*(5), 53–229.

Ding, Y., Fan, F., Tian, Z., et al. (2010). Atomic structure of Au-Pd bimetallic alloyed nanoparticles. *Journal of American Chemical Society, 132*(35), 12480–12486.

Ding, Y., Sun, X., Wang, Z. L., et al. (2012). Misfit dislocations in multimetallic core-shelled nanoparticles. *Applied Physics Letters, 100*(11), 111603.

Escalona, E. E., Pereira-Almao, P. R., Castillo, J., et al. (2006). Nanometric bimetallic sulfides prepared via thermal decomposition of Ni and Fe heteropolymolybdate emulsions. *Catalysis Letters, 112*(3-4), 227–230.

Farraghher, A. L. (1979). Surface vacancies in close packed crystal structures. *Advances in Colloid and Interface Science, 11*(1), 3–41.

Ferrer, D., Blom, D. A., Allard, L. F., et al. (2008). Atomic structure of three-layer Au/Pd nanoparticles revealed by aberration-corrected scanning transmission electron microscopy. *Journal of Materials Chemistry, 18*, 2442–2446.

Ferrer, D. A., Diaz-Torres, L. A., Wu, S., et al. (2009). Crystalline order of silver–gold nanocatalysts with hollow-core and alloyed-shell. *Catalysis Today, 147*(3), 211–216.

Frenkel, A. I., Hills, C. W., & Nuzzo, R. G. (2001). A view from the inside: complexity in the atomic scale ordering of supported metal nanoparticles. *Journal of Physical Chemistry B, 105*(51). 15689–12703.

Frey, G. L., Tenne, R., Matthews, M. J., et al. (1999). Raman and resonance Raman investigation of MoS_2 nanoparticles. *Physical Review B, 60*, 2883–2892.

Friel, J. J., & Lyman, C. E. (2006). Tutorial review: X-ray mapping in electron-beam instruments. *Microscopy and Microanalysis, 12*(1), 2–25.

Galvan, D. H., Deepak, F. L., Esparza, R., et al. (2011). Experimental and theoretical properties of S-Mo-Co-S clusters. *Applied Catalysis A: General, 397*(1), 46–53.

Gates, B. C. (1992). *Catalytic Chemistry*. New York: Wiley.

Hansen, L. P., Ramasse, Q. M., Kisielowski, C., et al. (2011). Atomic-scale edge structures on industrial-style mos_2 nanocatalysts. *Angewandte Chemie International Edition, 50*(43), 10153–10156.

Harada, H., Asakura, K., & Toshima, N. (1993). Catalytic Activity and Structural Analysis of Polymer-Protected Au/Pd Bimetallic Clusters Prepared by the Successive Reduction of HAuC14 and PdCl2. *Journal of Physical Chemistry, 97*(19), 5103–5114.

He, J., Ichinose, I., Kunitake, T., et al. (2003). Facile fabrication of Ag−Pd bimetallic nanoparticles in ultrathin TiO_2-gel films: nanoparticle morphology and catalytic activity. *Journal of the American Chemical Society, 125*(36), 11034–11040.

Homyonfer, M., Alperson, B., Rosenberg, Y., et al. (1997). Intercalation of inorganic fullerene-like structures yields photosensitive films and new tips for scanning probe microscopy. *Journal of American Chemical Society, 119*(11), 2693–2698.

Iglic, A., Tzaphlidou, M., Remskar, M., et al. (2005). Stable shapes of thin anisotropic nanostrips. *Fullerenes Nanotubes Carbon Nanostructures, 13*(3), 183–192.

Ionescu, A., Allouche, A., Aycard, J. P., et al. (2003). Study of γ-alumina-supported hydrotreating catalyst: I. Adsorption of bare MoS_2 sheets on γ-alumina surfaces. *Journal of Physical Chemistry B, 107*(33), 8490–8497.

Jang, Y. B., Kim, T. H., Sun, M. H., et al. (2009). Preparation of iridium catalyst and its catalytic activity over hydrazine hydrate decomposition for hydrogen production and storage. *Catalysis Today, 146*, 196–201.

Kisielowski, C., Ramasse, Q. M., Hansen, L. P., et al. (2011). Imaging MoS_2 nanocatalysts with single-atom sensitivity. *Angewandte Chemie International Edition, 49*(15), 2708–2710.

Koch, C. T. (2002). *Determination of core structure periodicity and point defect density along dislocations. ProQuest Dissertations and Theses; Ph.D. thesis*. Arizona State University.

Kotaka, Y. (2010). Essential experimental parameters for quantitative structure analysis using spherical aberration-corrected HAADF-STEM. *Ultramicroscopy, 110*(5), 555–562.

Kralj-Iglic, V., Remskar, M., & Iglic, A. (2004). *Horizons in World Physics*. New York: Nova Science Publishers. 111–156.

Krebs, E., Daudin, A., & Raybaud, P. (2009). A DFT study of CoMoS and NiMoS catalysts: from nano-crystallite morphology to selective hydrodesulfurization. *Oil & Gas Science and Technology, 64*(6), 707–718.

Li, Y., Zhou, Z., Zhang, S., et al. (2008). MoS_2 Nanoribbons: High Stability and Unusual Electronic and Magnetic Properties. *Journal of the American Chemical Society, 130*, 16739–16744.

Li, Y. W., & Delmon, B. (1997). Modelling of hydrotreating catalysis based on the remote control: HYD and HDS. *Journal of Molecular Catalysis A: Chemical, 127*(1-3), 163–190.

Lince, J. R. (2004). Tribology of Co-sputtered nanocomposite Au/MoS_2 solid lubricant films over a wide contact stress range. *Tribology Letters, 17*(3), 419–428.

Longo, R. C., & Gallego, L. J. (2006). Structures of 13-atom clusters of fcc transition metals by ab initio and semiempirical calculation. *Physical Review B, 74*, 193409.

Mayoral, A., Barron, H., Estrada-Salas, R., et al. (2010). Nanoparticle stability from the nano to the meso interval. *Nanoscale, 2*, 335–342.

Mayoral, A., Esparza, R., Deepak, F. L., et al. (2011). Study of nanoparticles at UTSA: one year of using the first JEM-ARM200F installed in USA. *JEOL News, 46*, 1–5.

Mazumder, V., Chi, M., More, K. L., et al. (2010). Synthesis and characterization of multimetallic Pd/Au and Pd/Au/FePt core/shell nanoparticles. *Angewandte Chemie International Edition, 49*(49), 9368–9372.

Mejia-Rosales, S., Fernandez-Navarro, C., Perez-Tijerina, E., et al. (2006). Molecular dynamics runs to simulate the melting transition of bimetallic cuboctahedral nanoparticles of gold palladium. *Journal of Physical Chemistry B, 110*(26), 12884–12889.

Mizukoshi, Y., Fujimoto, T., Nagata, Y., et al. (2000). Characterization and catalytic activity of core-shell structured gold/palladium bimetallic nanoparticles synthesized by the sonochemical method. *Journal of Physical Chemistry B, 104*(25), 6028–6032.

Olivas, A., Alonso, G., & Fuentes, S. (2006). The catalytic activity of Ni/W bimetallic sulfide nanostructured catalysts in the hydrodesulfurization of dibenzothiophene. *Topics in Catalysis, 39*(3-4), 175–179.

Pennycook, S. (1989). Z-contrast STEM for materials science. *Ultramicroscopy, 30*, 58–69.

Pennycook, S. J., & Boatner, L. A. (1998). Chemically sensitive structure-imaging with a scanning transmission electron microscope. *Nature, 336*, 565–567.

Perez-Tijerina, E., Mejia-Rosales, S., Inada, H., et al. (2010). Effect of temperature on AuPd nanoparticles produced by inert gas condensation. *Journal of Physical Chemistry C, 114*(15), 6999–7003.

Perez-Tijerina, E., Pinilla, G. M., Mejia-Rosales, S., et al. (2008). Highly size-controlled synthesis of Au/Pd nanoparticles by inert-gas condensation. *Faraday Discussions, 138*, 353–362.

Raybaud, P., Hafner, J., Kresse, G., et al. (2000). Structure, energetics, and electronic properties of the surface of a promoted MoS_2 catalyst: an ab initio local density functional study. *Journal of Catalysis, 190*(1), 128–143.

Recnik, A., Möbus, G., & Sturm, S. (2005). IMAGE-WARP: a real-space restoration method for high-resolution STEM images using quantitative HRTEM analysis. *Ultramicroscopy, 103*(4), 285–301.

Reimer, L., & Kohl, H. (2008). *Transmission Electron Microscopy: Physics of Image Formation*. New York: Springer.

Remskar, M., Skraba, Z., Stadelmann, P., et al. (2000). Structural stabilization of new compounds: MoS_2 and WS_2 micro- and nanotubes alloyed with gold and silver. *Advanced Materials, 12*(11), 814–818.

Rioux, R. M., Song, H., Grass, M., et al. (2006). Monodisperse platinum nanoparticles of well-defined shape: synthesis, characterization, catalytic properties and future prospects. *Topics in Catalysis, 39*(3), 167–174.

Rose, H. (1990). Outline of a spherically corrected semiaplanatic medium-voltage transmission electron microscope. *Optik, 85*, 19–24.

Schweiger, H., Raybaud, P., & Toulhoat, H. (2002). Promoter sensitive shapes of Co(Ni) MoS nanocatalysts in sulfo-reductive conditions. *Journal of Catalysis, 212*(1), 33–38.

Senevirathne, K., Burns, A. W., Bussell, M. E., et al. (2007). Synthesis and characterization of discrete nickel phosphide nanoparticles: effect of surface ligation chemistry on catalytic hydrodesulfurization of thiophene. *Advanced Functional Materials, 17*(18), 3933–3939.

Shidpour, R., & Manteghian, M. (2010). A density functional study of strong local magnetism creation on MoS_2 nanoribbon by sulfur vacancy. *Nanoscale, 2*(8), 1429–1435.

Sinfelt, J. H. (1983). *Bimetallic Catalyst: Discoveries, Concepts and Applications*. New York: Wiley.

Song, C. (2003). An overview of new approaches to deep desulfurization for ultra-clean gasoline, diesel fuel and jet fuel. *Catalysis Today, 86*(1-4), 211–263.

Srnová-Šloufová, I., Lednický, F., Gemperle, A., & Gemperlová, J. (2000). Core-shell (Ag) Au bimetallic nanoparticles: analysis of transmission electron microscopy images. *Langmuir, 16*(25), 9928–9935.

Stamenkovic, V. R., Fowler, B., Mun, B. S., et al. (2007). Improved oxygen reduction activity on Pt3Ni(111) via increased surface site availability. *Science, 315*(5811), 493–497.

Stroppa, D. G., Zagonel, L. F., Montoro, L. A., et al. (2012). High-resolution scanning transmission electron microscopy (HRSTEM) techniques: high-resolution imaging and spectroscopy side by side. *ChemPhysChem, 13*(2), 437–443.

Sun, M., Nelson, A. E., & Adjaye, J. (2004a). On the incorporation of nickel and cobalt into MoS_2-edge structures. *Journal of Catalysis, 226*(1), 32–40.

Sun, M., Nelson, A. E., & Adjaye, J., J. (2004b). A DFT study of WS_2, NiWS, and CoWS hydrotreating catalysts: energetics and surface structures. *Journal of Catalysis, 226*(1), 41–53.

Topsøe, H. (2007). The role of Co–Mo–S type structures in hydrotreating catalysts. *Applied Catalysis A, General, 322*, 3–8.

Toshima, N. (1996). Fine Particles Science and Technology: From Micro to Nanoparticles. In E. Pellizzetti (Ed.), *Colloidal Dispersion of Bimetallic Nanoparticles: Preparation, Structure and Catalysis* (pp. 371–383). Dordrecht: Kluwer.

Turaga, U. T., Ma, X., & Song, C. S. (2003). Influence of nitrogen compounds on deep hydrodesulfurization of 4,6-dimethyldibenzothiophene over Al_2O_3- and MCM-41-supported Co-Mo sulfide catalysts. *Catalysis Today, 86*(1-4), 265–275.

Tye, C. T., & Smith, K. J. (2004). Catalytic activity of exfoliated MoS_2 in hydrodesulfurization, hydrodenitrogenation and hydrogenation reactions. *Topics in Catalysis, 37*(2-4), 129–135.

Wall, J., Langmore, J., Isaacson, M., et al. (1974). Scanning transmission electron microscopy at high resolution. *Proceedings of the National Academy of Sciences, 71*, 1–5.

Whitehurst, D. D., Isoda, T., & Mochida, I. (1998). Present state of the art and future challenges in the hydrodesulfurization of polyaromatic sulfur compounds. *Advances in Catalysis, 42*, 345–471.

Wu, Z., Wang, D., Liang, X., et al. (2010). Novel hexagonal MoS_2 nanoplates formed by solid-state assembly of nanosheets. *Journal of Crystal Growth, 312*(12-13), 1973–1976.

Yoosuk, B., Kim, J. H., Song, C., et al. (2008). Highly active MoS_2, $CoMoS_2$ and $NiMoS_2$ unsupported catalysts prepared by hydrothermal synthesis for hydrodesulfurization of 4,6-dimethyldibenzothiophene. *Catalysis Today, 130*(1), 14–23.

Zak, Z., Feldman, Y., Lyakhovitskaya, V., et al. (2002). Alkali metal intercalated fullerene-like MS_2 ($M = W$, Mo) nanoparticles and their properties. *Journal of the American Chemical Society, 124*(17), 4747–4758.

Zuo, J. M. (2008). *JProbe*. Available at. http://cbed.matse.illinois.edu/.

INDEX

Note: Page numbers followed by “f” and “t” indicate figures and tables, respectively

A

Aberrations, 195–196, 287–290
  contrast transfer function (CTF), 287
  optical aberrations, 196–197
Absolute convergence, 63–64
Accelerator system, 262
ADF. *See* Annular dark-field
Adjoint dilation, 92
Adjoint erosion, 92
Adjoint signal dilation, 128
Adjoint signal erosion, 127
Adjunction, 52–53, 92
  flat erosion, 94
  Minkowski flat dilation, 94
  Minkowski set dilation, 93
  Minkowski set erosion, 94
  Minkowski weighted erosion, 95
  properties, 93
  real-valued functions, 94
  supremal convolution, 95
Algebraic decomposition, 72
  algebraic complement, 72
  linear space, 72
Algebraic isomorphism, 71
Alternating sequential filter (ASF), 108–109
Amoeba filters, 97
Annular dark-field (ADF), 283, 285–286
Anti-isomorphism. *See* Dual isomorphism
Antitone. *See* Decreasing operators
Area filters
  area opening, 104–105
  attribute openings, 105–106
ASF. *See* Alternating sequential filter
Atom, 82

B

Banach space, 63
Bas (ψ), 157
Benzécri algorithm, 17. *See also* Two-dimensional algorithm (2D algorithm)
  image size, 18
  Pseudo-code, 18f
Benzécri HAC. *See* Benzécri hierarchical ascendant classification
Benzécri hierarchical ascendant classification (Benzécri HAC), 14–15
  hierarchy
    dissimilarity index, 16
    parts and levels, 15
    property, 15
    using remarks, 16
    segmentations, 15
    stratified hierarchy, 16
  image segmentation, 15
  using 2D algorithm, 15
  2D images, 17
  ultrametrics, 16
    circle’s diameter, 17
    properties, 16–17
    ultra metric, 17
    ultrametrical space, 17
BF images. *See* Bright-field images
Bimetallic nanoparticles, 304
  using advanced electron microscopic techniques
    aberration-corrected STEM images, 307f
    Au_1Pd_4 nanoparticle, 312, 313f
    BF-STEM images, 312–314, 314f
    characterization, 308, 308f
    chemical maps, 309f
    clusters of opalladium-iridium, 315–316, 315f
    EDAX, 307–308
    EELS map, 309, 310f
    factors, 306–307
    four-layer Au/Pd nanoparticles, 309–311, 311f
    gold-palladium, 306–307
    HAADF and BF-STEM images, 314, 315f
    HAADF images, 306f

Bimetallic nanoparticles (*Continued*)
        using HR-TEM, 305
        NBD, 311–312, 312f
        palladium core, 307–308
        structures, 305, 305f
        three-layer nanoparticle, 309, 310f
    in situ heating experiments, 316
        HAADF and BF image pairs, 317f
        Ostwald ripening effects, 316–318
        palladium-gold-palladium nanoparticles, 316–318
Boolean algebra. *See* Boolean lattices
Boolean filter, 162–163
Boolean functions
    binary filter, 163
    binary indicator function, 162–163
    binary signal, 163–164
    increasing functions, 162
    minimal true and maximal false vector, 162, 164
    representation theory, 161–162
    stack filters, 164
Boolean lattices, 83
    Boolean algebra, 83
    Boolean functions, 84
    field of sets, 83
    finite, 83
    n-dimensional Boolean vectors, 83–84
Boolean operator. *See* Boolean filter
Bounded linear operators space, 69–70
Bright-field images (BF images), 283
British Thomson Houston Co. (BTH), 191

C

Cambridge high-voltage microscope project
    accelerator system, 262
    acceptance tests and delivery, 263–264
        bulky item cases, 264
        forming process, 265–266
        high-voltage set, 267
        Minkner and Bach, 266–267
        Reinhold report, 264
    Cavendish, 245–246
    Cockcroft–Walton generator, 247–248
    construction work, 247
    Cosslett's plan, 247
    departure from Cavendish
        EM group, 270–271
        HVEM, 269–270
        Professor Ratcliffe, 268–269
        ramifications, 269
        reminiscences, 271
        William Du Bois Duddell Medal, 271f
    electron lenses, 263
    first test report, 267–268
        micrographs, 269f
    using forklift trolley, 252–253
    freighter aircraft, 248
    Haefely equipment, 250
    high-voltage generator, 247
    high-voltage room
        aluminum panels, 259
        annual garden party, 262
        finished and fully operational, 265f
        Millpool, 261–262
        normal tea-room hum conversation, 261
        Ray Dolby, 259–261
        Ron Pryor and Richard Donoghay polishing, 260f
    injector system, 262
    microscope complex, 254f
    operating an electron microscope, 246
    Paul Instrument Fund Committee, 249
    radiation protection, 253
    repairs to Whitegates, 250–251
        CEGB, 251
        high-voltage set, 251f
        after removing cable and rethatching, 252f
        showing electricity cable strung, 252f
    structural alterations
        emergency exit, 256f
        establishment, 258–259
        face-to-face meeting, 255
        high-voltage power transmission, 256–257
        installing earthing rods, 255f
        magnetic shielding, 257
        sightseeing, 257–258
        university estate management service, 254–255
        vibration-isolating block, 253–254
    vibration transmission, 253

  X-ray microscope, 249–250
Cambridge Western, 274
Carbon fullerene onion (CNO), 299
Catalyst characterization
  bimetallic nanoparticles, 304
    using advanced electron microscopic techniques, 305–316
    structure, 305–316
  clusters, 304
  metal catalysts
    on γ-Al_2O_2, 301–304
    on crystalline substrate, 294–299
    on noncrystalline substrate, 299–301
  multimetallic systems, 318–319
  in situ heating experiments
    bimetallic nanoparticles, 316
    clusters, 316–318
Catalytic systems, 280
Cauchy sequence, 63
Cauchy-Schwarz inequality, 64
CBED. *See* Convergent beam electronic diffraction
Chain, 78, 81
Chapman, A. H., 213
Charles Oatley, EM at Cambridge University. *See also* Ellis Cosslett, EM at Cambridge University
  applications, 219–220
    etched germanium surface, 220f
    plastic scintillator, 221
    PPRIC, 222
    sailing, 223–224
    silver azide crystals, 222–223
    silver azide needle, 223f
    spruce wood fiber, 222f
    TEM, 220–221
  informal contacts
    conversation, 203
    sanatron, 204
  personal affairs, 205
    at Cambridge, 205–206
    fairwell to crew, 206–207
    Sheila, motorcycling, 205f
    time for music, 208–209
  personal interlude, 230–231
    Alvis Speed 20, 230f
    announcement, 232
    Cambridge in one day's driving, 236–237
    journey, 231
    magical experience, 234
    old fisherman posing, 235f
    Peggy McLean, 234–236, 235f
    Pru Woodman, 233, 233f
    stomach-churning experience, 231
    SU carburetors, 231f
  problems with microscope, 209
    electron beam, 210–211
    elementary error cost, 211
    frustrating experience, 210
    Oliver Wells and author confer, 211f
    SEM, 214
    SEM3, 213–214
    stigmator, 210
    wireless receivers, 212
  scanning electron microscope
    detector system, 197
    electron optical projects, 200–201
    electron spot, 196
    electron trajectory tracer, 203
    Ellis Cosslett's electron microscopy, 202f
    improvement in efficiency, 199
    limitation, 194–195
    magnification, 196
    McMullan's original incarnation, 198f
    practical electronics work, 198
    principles, 195–196
    proceedings, 202
    schematic diagram, 195f
    Sheila Smith at controls, 201f
    technical problems, 199
    TEM invention, 193–194
    transmission microscope, 193
    visual acuity, 202
  SEM1, 224–225, 225f
  SEM2, 225
  SEM3, 226, 228f
    AEI, 226
    construction, 228–230
    cross section, 229f
    electromagnetic lenses, 226
    EM4, 226–227
    Everhart–Thornley detector, 227–228

Charles Oatley, EM at Cambridge University (*Continued*)
    - for export to Canada, 237
    - "KCA passed this way," 238f
    - preparation and manipulation, 227
    - sumptuous first-class fare, 237–239
  - specimen chamber, 214–215, 216f
    - applications, 216
    - Glasgow conference, 217
    - Oliver in diving gear, 218f
    - point-contact rectifiers, 215
    - publication, 216
    - SEM, 217
    - testing, 215–216
    - weather, 219

Clodum, 56–57, 110
  - bounded lattice-ordered group, 113–114
  - dual addition, 112
  - dual multiplication, 112
  - lattice arithmetic algebraic structure, 112–113
  - nonlinear spaces, 114–119
    - complete weighted lattices of function, 118–119
    - general algebraic structure, 114–116
    - sup/inf span, independence, basis, dimension, 116–117
  - self-conjugate element, 114

Clusters, 304
  - *in situ* heating experiments, 316
    - HAADF and BF image pairs, 317f
    - Ostwald ripening effects, 316–318
    - palladium-gold-palladium nanoparticles, 316–318
  - of opalladium-iridium, 315–316, 315f

CNO. *See* Carbon fullerene onion

CNR. *See* French National Centre for Scientific Research

Co-doped MoS_2/WS_2 nanowire catalysts, 326–327
  - BF-STEM and HAADF-STEM images, 327f, 328f
  - density functional theory calculations, 331–334
  - EDAX line scans, 330–331, 331f
  - high-resolution, 329, 330f
  - low-magnification, 327–329, 329f
  - perspective and top views, 332f
  - SEM micrographs, 333f

Cockcroft–Walton generator, 247–248

Complete weighted lattice space (CWL space), 114–115
  - image operators on, 119
  - signal translations, 123

Complex linear space. *See* Hilbert space; Real linear space

Computational theory, 49

Condenser system, 194

Connected filters, 104

Continuous functions, 67

Contrast transfer function (CTF), 287

Conventional electron microscope, 194

Conventional transmission electron microscopy (CTEM), 283

Convergence
  - continuity on topological image spaces, 98
    - hit-miss topology, 98
    - image signal space, 99
    - set sequence, 98–99
    - u.s.c., 99
  - order convergence
    - continuity on lattices, 99
    - erosions and dilations, 101
    - limsup and liminf combinations, 100
    - minimax inequality, 100
    - monotonic convergence, 100
    - order continuity, 100
  - sequence, 63

Convergent beam electronic diffraction (CBED), 293

Convex analysis and optimization, 54
  - digital geometry, 54
  - Legendre–Fenchel conjugate transform, 54

Convolution adjunctions, scalar dilations, 127

Cosslett, Ellis
  - AEI EM7 lenses, 273
  - EM7, 272
  - Institute of Electron Optics, 272–273
  - John Catto's contribution, 273–274
  - start-up companies, 274
    - Cambridge Western, 274

    - Granta Electronics, 274
    - SDI, 275
    - synoptics origins, 275
  - Whitegates again, 276
- Coventry City boundary, 191
- CTEM. *See* Conventional transmission electron microscopy
- CTF. *See* Contrast transfer function
- CWL space. *See* Complete weighted lattice space

D

- Dark-field mode (DF mode), 283
- DBT. *See* Dibenzothiophene
- Decreasing operators, 90
  - class, 92
    - anti-dilations, 92
    - anti-erosions, 92
    - dilations, 92
    - erosions, 92
  - complete lattices, 91
  - dual homomorphisms, 90
  - dual isomorphism, 91
  - grey-level images, 91
  - signal operators, 91
  - thresholding operators, 91
- DEDS. *See* Discrete-event systems control
- Definite matrix, 144
- Detector system, 197
- DF mode. *See* Dark-field mode
- DFT. *See* Discrete Fourier transform
- Dibenzothiophene (DBT), 319–320
- Digital geometry, 54
- Digital image processing, 49
- Dilation translation-invariant system (DTI system), 126
- Dilation V-translation invariant operator (DVI operator), 122
- Dilations, 48
- 4,6-Dimethyldibenzothiophene (4, 6-DMDBT), 319–320
- Discrete Fourier transform (DFT), 298–299
- Discrete linear filter, 167
- Discrete space. *See* Euclidean space
- Discrete version. *See* Euclidean domain
- Discrete-event systems control (DEDS), 55
- Dissimilarity index, 16
- Distance transform, 54
- Distributive lattice, 79–80
- 4,6-DMDBT. *See* 4,6-Dimethyldibenzothiophene
- DTI system. *See* Dilation translation-invariant system
- Dual atoms, 82
- Dual automorphism, 79
- Dual isomorphism, 91
- Dual poset, 78
- Dual semi-atoms, 82
- Duality principle, 78
- DVI operator. *See* Dilation V-translation invariant operator

E

- ED. *See* Electron diffraction
- EDAX. *See* Energy dispersive analysis of X-ray
- EDS. *See* Energy-dispersive spectroscopy
- EDX spectroscopy. *See* Energy-dispersive X-ray spectroscopy
- EELS. *See* Electron energy-loss spectroscopy
- Eigennode, 144
- Eigenvalue, 144
- Eigenvectors, 144–145
- Electron diffraction (ED), 283
- Electron energy-loss spectroscopy (EELS), 283
- Electron lenses, 263
- Electron microscope 3 (EM3), 213–214
- Electron microscope 7 (EM7), 272
- Electron trajectory tracer, 203
- Ellis Cosslett, EM at Cambridge University with
  - Cambridge high-voltage microscope project, 245–246
    - acceptance tests and delivery, 263–268
    - departure from Cavendish, 268–271
    - design concepts, 252–253
    - electron lenses, 263
    - first test report, 267–268
    - high-voltage room, 259–262
    - injector and accelerator system, 262
    - repairs to Whitegates, 250–251
    - structural alterations, 253–259
  - post in Cavendish laboratory, 239

Ellis Cosslett, EM at Cambridge University with (*Continued*)
  arrangements, 239–240
  British Airways Vickers Viscount turboprop, 239
  cash transaction, 242
  commercial side, 245
  convenience and flexibility, 240
  double garage, 241
  encyclopedia, 244
  entrance to Whitegates, 240–241
  image intensifiers, 243
  interim measure, 244
  modern microscopy, 243
  Tiplady's, 245
EM3. *See* Electron microscope 3
EM7. *See* Electron microscope 7
Emile Haefely & Co., 255–256
Energy dispersive analysis of X-ray (EDAX), 307–308
Energy-dispersive spectroscopy (EDS), 285–286
Energy-dispersive X-ray spectroscopy (EDX spectroscopy), 283
Erosion translation-invariant system (ETI system), 126
Erosions, 48
ETI system. *See* Erosion translation-invariant system
Euclidean distance, 19
Euclidean domain, 59
Euclidean metric, classical, 33
Euclidean morphological operators. *See* Minkowski operators
Euclidean space, 60
Euclidean topology, 99
Everhart–Thornley detector, 227–228

F

Fast Fourier transform (FFT), 334–335
FEG. *See* Field emission gun
FFT. *See* Fast Fourier transform
Field emission gun (FEG), 282–283
Finite impulse response filters (FIR filters), 156, 165–166
Finite-dimensional image spaces
  continuous domain, 66–67
  discrete domain, 65–66
Finite-dimensional linear spaces, 57, 62, 68
Finite-dimensional nonlinear vector spaces, 119
Finite-dimensional spaces, 65
Finite-dimensional vector spaces, 62
  linear operators on
    matrix representation of, 74–75
    spectral representation of, 76–78
  weighted minimax spaces, 139–142
FIR filters. *See* Finite impulse response filters
Flat operators
  grey-level median, 161
  set generator, 161
  signal operator, 159–160
  stack filters, 161
Forming process, 265–266
French National Centre for Scientific Research (CNR), 247–248
Function lattice, 84–85
  pointwise partial ordering, 84
  power lattice, 84–85
  signal lattices, 85
  vector lattices, 85
Fuzzy dilation, 134–135
Fuzzy norms, 131–132
  dual-translated dual impulses, 133–134
  fuzzy convolutions, 133
  fuzzy operations, 136, 137f
  image analysis, 138–139
  intersection norm, 133
  lattice image processing, 131–132
  lattice-fuzzy openings and closings, 135–136
  mathematical morphology, 132
  morphological flat dilation and erosion, 136–138, 138f
  t-conorms, 132
  t-norms, 132, 135
  union norm, 133

G

Gold
  nanoparticles, STEM micrographs, 291f
  nanostructure, HR-TEM simulations, 288f
Gold-iridium alloy, 298–299
Gold-palladium nanoparticles, 304, 306–308

- core-shell structures, 312–314
- energy dispersive analysis, 308
- intercalation, 307f

Gold-palladium-gold nanoparticles, 311–312, 316–318
- orientation, 312

Granta Electronics, 274

Graphispot chart recorder, 264–265

Gravitational clustering, 25
- adaptation
  - aggregation, 26–27
  - gravitational interaction, 25f
  - grey-level image, 26
  - histogram, 26
  - to image processing, 25–26
  - LIP framework, 26
- implementation
  - algorithm, 27
  - grey-level axis, 27f
  - heart, 28–30
  - initialization, 27–28
  - SM algorithm, 27
- metrics selection
  - applications, 34
  - classical Euclidean metric, 33
  - logarithmic metric, 33
  - SM and OA algorithms, 33
- notations, 25
- principle, 25
- results, 34, 35f, 37f
- RGB components, 36–37

Grey-level area opening, 104–105, 105f

Grey-level images, 50–52

Grey-level median, 161

H

HAADF detector. *See* High-angle annular dark-field detector

HAADF-STEM. *See* High-angle annular dark-field scanning transmission electron microscopy

HAC. *See* Hierarchical ascendant classification

Hamel basis, 62, 117

HCP structure. *See* Hexagonal close-packed structure

HDN. *See* Hydrodenitrogenation

HDO. *See* Hydrodeoxygenation

HDS. *See* Hydrodesulfurization

Heijman's monograph, 57

Hexagonal close-packed structure (HCP structure), 311–312

Hierarchical ascendant classification (HAC), 2–3
- Benzécri algorithm, 17–18
- Benzécri HAC, 14–15
  - hierarchy, 15–16
  - ultrametrics, 16–17
- building steps
  - with Euclidean metric, 20f
  - with logarithmic metric, 20f
- classical quad tree decomposition, 24f
- color, 22f, 23f
- comparison, 23f
- dendrogram representation, 20f
- grey-level, 21f, 22f
- initial image values, 19f
- intermetric comparison, 23f
- random color LUT, 22f, 24f
- results and examples, 21–24
- specific approach, 19–21
- 2D images, 17

High-angle annular dark-field detector (HAADF detector), 280–281, 285–286

High-angle annular dark-field scanning transmission electron microscopy (HAADF-STEM), 285–286

High resolution electron microscope (HREM), 272–273

High-resolution transmission electron microscopy (HR-TEM), 281

High-voltage electron microscope (HVEM), 245–246

High-voltage power transmission, 256–257

Hilbert space, 64, 73

Hit-miss transformation, 90, 155

Hölder inequality, 66

Homomorphisms, 88–89

HR-TEM. *See* High-resolution transmission electron microscopy

HREM. *See* High Resolution Electron Microscope

- HVEM. *See* High-voltage electron microscope
- Hydrodenitrogenation (HDN), 319–320
- Hydrodeoxygenation (HDO), 319–320
- Hydrodesulfurization (HDS), 319–320

I

- ILTI operator. *See* Increasing linear translation-invariant operator
- Image algebra, 54–55
- Image function model, 65
- Image lattices
  - distributive lattices, 85–86
  - grey-level image signals, 86
  - l.s.c. functions, 86
  - set lattice, 85–86
  - shapes and images, 85
  - spatiotemporal image signals, 85
  - u.s.c. functions, 86
  - vector-valued images, 86
- Image operators, 119
  - on CLW, 119
  - image signals, 119
  - matrix representations
    - basis vectors, 140
    - CWL, 139
    - dual vector representation, 140–141
    - finite-dimensional function lattice, 139
    - linear vector space, 141
    - *min-***matrix* product, $\boxed{\star}$, 141
    - pulse vectors, 140
    - V-translations, 139
  - semi-atoms, 119–120
  - V-translations, 120
- Increasing linear translation-invariant operator (ILTI operator), 166
- Increasing operators, 88–89
  - automorphisms, 89
  - hit-miss transformation, 90
  - homomorphisms, 88–89
  - lattice-based image analysis, 89
  - structuring element, 90
- Infimal convolution, 54
- Infimum, 78
- Infinite-dimensional image spaces
  - continuous-domain, 66–67
  - discrete-domain, 65–66
- Infinite-dimensional linear spaces, 57, 62, 68
- Injector system, 262
- Invariance domain, 102
- Isometry isomorphism, 71
- Isomorphic linear spaces, 68
- Isomorphism, 71. *See also* Dual automorphism
  - algebraic isomorphism, 71
  - isometry isomorphism, 71
  - topological isomorphism, 71
  - unitary operator, 71
- Isotone. *See* Increasing operators

J

- Janus structure, 305f
- Jet propulsion Laboratory, 275
- Jolly Miller pub, 261–262

K

- K-means algorithm. *See also* Multithresholding; Region growing method
  - comments, 6–7
  - Köhler's approach, 4
  - La Rochelle port, 6f
  - Nuées dynamiques, 4
  - principle, 4–6
- Kernel, adaptive, 97
- Kernel elements
  - translation invariant operators, 146
    - Bas (ψ), 157
    - denoising, 157–158
    - dual set operator, 147
    - Hamel basis, 62, 158–159
    - increasing set operators, 146
    - kernel property, 146
    - minimal kernel elements, 147–148
    - minimal subcollection, 149
    - morphological basis, 159
    - non-flat, 159
    - nondegenerate operators, 146
    - set dilation, 146
    - set erosion operator, 146
    - set operator bases, 150
    - signal operator, 156–157
    - TI filters, 158
    - u.s.c. function, 148–149

    - weighted erosions and dilations, 157
- Kernel operators, 145–146
- Kernel representation theory, 145, 156
- Köhler's approach, 3–4
- *k*th rank set operator, 152
  - closed formula, 153
  - dual set operator, 153
  - 5-pixel discrete rhombus, 152–153, 153f

L

- l.s.c. function. *See* Lower semi-continuous function
- Lattice, 78–79
  - adjunctions, 57–58
  - atomic, 82
  - chain, 81
  - distributive, 79–80
  - isomorphism, 88–89
  - linear space, 81
  - modular, 80
  - morphology, 52
  - operations, 79t
  - operators, 57–58
  - power set, 81
  - projections, 57–58
  - ring of sets, 81
- Lattice automorphism. *See* Lattice—isomorphism
- Lattice spaces, 78
  - adjoint dilation, 92
  - adjoint erosion, 92
  - adjunction, 92
  - Boolean lattices, 83
  - convergence, 98
  - duality in lattices, 79
  - duality principle, 78
  - function lattices, 84
  - image lattices, 85
  - isomorphism, 79
  - monotone lattice operators, 88
  - order projections, 101
  - partial ordering, 78
  - properties, 79
  - semilattices, 80
  - shift-varying operators, 95
  - signal operators, 87
  - sublattices, 80
  - sup-generators, 82
- Layered material electron microscopy, 319–320
  - co-doped MoS_2/WS_2 nanowire catalysts, 326–327
    - BF-STEM images, 327f, 328f
    - density functional theory calculations, 331–334
    - EDAX line scans, 330–331, 331f
    - HAADF-STEM images, 327f, 328f
    - high-resolution, 329, 330f
    - low-magnification, 327–329, 329f
    - perspective and top views, 332f
    - SEM micrographs, 333f
  - MoS_2 nanoplates
    - FFT plates, 334–335
    - HR-TEM micrograph, 336–337, 337f
    - nanohexagonal plates, 334
    - superimposition, 336f
    - ultra–high-resolution BF-STEM image, 334, 335f
  - MoS_2 nanowire catalysts, 320–321
    - HAADF-STEM image, 321, 322f
    - helical structure, 321
    - side and transversal views, 324f
    - slab-size effects, 321–325
    - supported on Al_2O_3, 323f
    - zizzag-and armchair-terminated MoS_2 sheets, 325–326
  - transition metal chalcogenides, 319–320
- Left adjoint. *See* Adjoint erosion
- Legendre–Fenchel conjugate transform, 54
- Levelings
  - object-oriented filters, 109
  - self-dual reconstruction filter, 109–110
- Linear convolution, 76
- Linear isometry. *See* Isometry isomorphism
- Linear operators
  - algebraic definitions, 68
  - isomorphism, 71, 79
  - normed spaces, 69
    - bounded, 69
    - continuous linear maps, 69
    - infinite linear superposition principle, 69
  - representation, 74
    - finite-dimensional vector spaces, 74

Linear operators (*Continued*)
    - linear combination, 74
    - ring of linear operators, 75
  - Riesz representation theorem and linear convolution, 75
  - self-adjoint operator, 70
  - spectral representation, 76

Linear projections
  - algebraic decomposition, 72
    - algebraic complement, 72
    - linear space, 72
  - orthogonal projections, 72–73
    - least square approximation, 73–74
    - orthogonal complement, 72–73
    - properties, 73

Linear shift-invariant filter (LSI filter), 165

Linear signal processing, 57

Linear spaces, 81
  - algebraic structure, 61
    - conditions, 61–62
    - finite and infinite dimensional, 62
    - linear combination of points, 62
    - linear subspace, 62
    - linearly independent, 62
    - theorem, 62
  - continuous functions, 67
  - finite-dimensional spaces, 65
  - geometric structure
    - inner product linear spaces, 64
    - orthogonal, 64
    - properties, 64
    - Pythagorean theorem, 64
  - infinite-dimensional image spaces
    - continuous-domain, 66–67
    - discrete-domain, 65–66
  - linear operators
    - algebraic definitions, 68
    - isomorphisms, 71
    - normed spaces, 69
    - self-adjoint operator, 70
  - linear projections
    - algebraic decomposition, 72
    - orthogonal projections, 72–74
  - topological structure
    - Cauchy test, 63–64
    - convergent sequence, 63
    - equivalent metrics, 63
    - metric space, 63
    - norm, 63
  - viewpoints, 61

LIP model. *See* Logarithmic image processing model

Lipschitz continuous functions, 67, 87

Logarithmic image processing model (LIP model), 3, 7
  - digitized images, 2
  - grey-scale digitization, 2
  - HAC, 2–3
  - homogeneity or texture, 2
  - image segmentation, 2
  - reflections
    - grey-level images, 40
    - optical vector space, 41
    - using remarks, 42
    - transmittance law, 40
    - transmittances formula, 41

Logarithmic metrics, 33

Lower semi-continuous function (l.s.c. function), 86

LSI filter. *See* Linear shift-invariant filter

M

Matrix rank, 143

Max-$\star$ dependent combination, 117

Max-$\star$ independent combination, 117

Max-plus algebra, 55. *See also* Minimax algebra; Nonlinear matrix algebra

Max-plus convolution, 54

Max-plus image operators, 129
  - kernel, 130
  - max-plus case, 130
  - shift invariance, 130

Max-plus matrix algebra, 142
  - conjugate matrix, 142
  - definite and metric matrix, 144
  - eigenvalue, 144
  - eigenvectors, 144–145
  - graph of matrix, 143–144
  - matrix rank, 143
  - optimization problem, 142–143

Max-product image operators, 130–131
  - isomorphism, 131
  - sup-product convolution, 130–131

Mean squared error (MSE), 73–74

Median, 152
  adaptive, 170–171
Metal catalysts
  on γ-Al_2O_2, 301–304
    metal-TiO_2, 304
    Pt/γ-Al_2O_3 catalyst, 303f
  on crystalline substrate, 294–295
    Au/Ir alloy support in TiO_2, 298f
    Au/TiO_2 catalyst image, 297f
    EELS analysis, 298–299
    signal-to-noise ratio, 296–298
    STEM-HAADF image, 296f
  on noncrystalline substrate, 299
    aberration corrected TEM, 302f
    CNO, 299
    DF and BF, 301f
    iridium support on Vulcan carbon, 300f
    Z-contrast images, 300–301
Metric matrix, 144
Minimal kernel elements, 147–148
Minimax algebra, 55, 110
  clodum, 110
  lattice-ordered monoids, 111
    lattice-ordered group, 111
    lattice-ordered monoid, 111–112
    poset, 111
    semilattice-ordered monoid, 111
  max-plus mathematical morphology, 110
  nonlinear space, 110
Minkowski operators, 50–52, 90
Minkowski set dilation, 93
Minkowski set erosion, 94
Minkowski weighted erosion, 95
Modular lattice, 80
Monotone lattice operators
  decreasing operators
    complete lattices, 91
    dual homomorphisms, 90
    dual isomorphism, 91
    grey-level images, 91
    signal operators, 91
    thresholding operators, 91
  increasing operators, 88–89
    automorphisms, 89
    hit-miss transformation, 90
    homomorphisms, 88–89
    lattice-based image analysis, 89
    structuring element, 90
  lattice structures, 88
Morphological filters, 101
Morphological operators
  developments, 50–52
    algebraic structure, 52–53
    classic mathematical morphology, 50–52
    clodum, 56–57
    convex analysis and optimization, 54
    finite-dimensional case, 55–56
    image algebra, 54–55
    image analysis applications, 52
    lattice framework, 53
    lattice operators, 52
    minimax algebra, 55
    nonlinear dynamical systems, 53–54
  linear spaces, 61
  minimax algebra, 110
  notation, 60
  representation theory, 47
Morphological set operators, 150
  constraints, 166
  discrete linear filter, 167
  erosions supremum, 166–167
  *k*th rank set operator, 152
    closed formula, 153
    dual set operator, 153
    5-pixel discrete rhombus, 152–153, 153f
  median, 152
  Minkowski closing, 150–151
  Minkowski dilation, 150
  Minkowski erosion, 150
  Minkowski opening, 150–151
  moving average filter, 167
  opening and closing basis sets, 151, 152f
  upper support, 166
  window transformations, 153
Morphology, adaptive, 97–98
Morrison air-raid shelter, 191–192
MoS_2 catalysts, 319–320
  nanoplates
    FFT plates, 334–335
    HR-TEM micrograph, 336–337, 337f
    nanohexagonal plates, 334

MoS_2 catalysts (*Continued*)
        superimposition, 336f
        ultra–high-resolution BF-STEM image, 334, 335f
    nanowire catalysts, 320–321
        armchair-terminated MoS_2 sheets, 325–326
        HAADF-STEM image, 321, 322f
        helical structure, 321
        side and transversal views, 324f
        slab-size effects, 321–325
        supported on Al_2O_3, 323f
        zizzag- terminated MoS_2 sheets, 325–326
MSE. *See* Mean squared error
Multimetallic systems, 318–319
Multithresholding, 3. *See also* K-means algorithm
    contrast curve, 4
    Köhler’s approach, 3–4, 5f
    techniques, 3

N
Nanobeam electron diffraction (NBD), 311–312
Nanoribbons, 280
National Autonomous University of Mexico (UNAM), 294–295
NBD. *See* Nanobeam electron diffraction
Neighborhoods, adaptive, 97–98
Nonlinear functional analysis, 50
Nonlinear matrix algebra, 55
Nonlinear spaces
    algebraic structure, 114
        clodum, 114
        CWL space, 116
        WL, 114–115
    complete weighted lattices functions
        CWL space, 118
        pointwise functions, 118
        self-conjugate element, 119
    sup-⋆ combination, 116–117
        Hamel basis, 117
        max-⋆ and min-⋆'combination, 117
Normed spaces, 69
    bounded, 69
    continuous linear maps, 69
    infinite linear superposition, 69
Notation
    image domain, 60
    image operators, 60–61
    linear operators, 60
    morphological operators, 60
Null element, 78–79
Null space, 68

O
Optimized automated algorithm (OA algorithm), 31, 36f. *See also* Sampling of mechanical model algorithm (SM algorithm)
    acceptable solutions, 32
    amalgamation, 31–32
    flowchart, 32f
    initialization, 31
    moving bodies, 32–33
Order continuity, 100
Order projections, 101
    alternating sequential filters, 108–109
    lattice theoretic properties, 101
        extensive and anti-extensive operators, 102
        openings and closings, 102–103
    levelings, 109
Orthogonal projections, 72–73
    least squares approximation, 73–74
    orthogonal complement, 72–73
    properties, 73
Ostwald ripening effects, 316–318

P
Palladium-gold-palladium nanoparticles, 311–312
Partial differential equation (PDE), 53–54
Partial ordering, 78
Parts hierarchy, 15
PDE. *See* Partial differential equation
Peppers image, 21
Planar set operators, 170
Polyvinylpyrrolidone (PVP), 304
POS. *See* Product-of-sum
Power lattice. *See* Function lattice
Power set, 81
PPRIC. *See* Pulp and Paper Research Institute of Canada

Prime implicant, 161–162
Product-of-sum (POS), 161–162
Pseudonorm. *See* Seminorm
Pulp and Paper Research Institute of Canada (PPRIC), 222
PVP. *See* Polyvinylpyrrolidone

Q

Quantization error effects, 99

R

Radial openings, 103–104, 104f
Real linear space, 62
Reconstruction
  closing
    grey-level reconstruction filterings, 108f
    image simplification, 107–108
  opening, 106
    conditional dilation, 106, 107f
    grey-level reconstruction opening, 107
    marker, 107
Red-green-blue image (RGB image), 6–7
Reflection microscope, 193
Region growing method. *See also* K-means algorithm
  classical
    aggregation process, 8
    equivalence relation, 8
    grey-level distribution, 11
    using pixels, 8
    using remarks, 9
    single linkage effects, 9, 11f
    3D image segmentation, 9–11
    transitivity saturation, 9
  LIP version
    using commands, 12
    efficiency, 11
    using formula, 11–12
    logarithmic single linkage, 12f
    objectives, 13
    3D region growing segmentation, 12f
  notations
    grey-level image, 7
    LIP model, 7
    multiplication calculation, 8
    space of images, 7–8
  systolic approach, 14f
    classical version, 13
    using remarks, 13–14
    Revol's approach, 13
    seed's exclusion, 14
Representation theory, 47
  computational theory, 49
  digital image processing, 49
  dilations and erosions, 48
  finite-dimensional case, 58–59
  image operators, 47–48
  image representations, 47
  image-processing tasks, 50
  lattice adjunctions, 57–58
  lattice structure, 58
  linear and morphological image simplification, 51f
  linear signal processing, 57
  minimal kernel elements collection, 59
  Minkowski openings, 60
  morphological filterings, 50
  morphological operators, 48–49
    theory, 57
  nonlinear functional analysis, 50
  non-monotone TI operator, 59
  signal algebra, 58
Research Department, 192
Revol's approach, 13
RGB image. *See* Red-green-blue image
RHS. See Right-hand side
Riesz's representation theorem, 57
  discrete-time linear convolution, 76
  impulse response, 76
  linear convolution, 76
  linear transformation, 75
  time signals, 75
Right adjoint. *See* Adjoint dilation
Ring of sets, 81
Rolls-Royce Merlin engines, 192
Ronchigram, 293
  calculated, 294f
  for different focus conditions, 295f
  experimental, 294f
  focus spot, 293

S

Sailing, 223–224
Sampling of mechanical model algorithm (SM algorithm), 27, 34–36, 34f. *See also* Optimized automated algorithm (OA algorithm)
  flow chart, 27, 29f
  gravitational clustering, 27, 39f
  initialization
    integer positions, 27
    optimal number search, 32f
  merging trees, 38f, 39f
  steps, 28–30
    using cases, 30–31
    using loop equations, 30
    movement quantity normalization, 29–30
    velocities and positions, 30
Sanatron, 204
Sash window, 254–255
Scale parameter, 51f
Scanning electron microscope (SEM), 193–194. *See also* Transmission electron microscope (TEM)
  detector system, 197
  electron optical projects, 200–201
  electron spot, 196
  electron trajectory tracer, 203
  Ellis Cosslett's electron microscopy, 202f
  imaging, 280–281
  improvement in efficiency, 199
  limitation, 194–195
  magnification, 196
  McMullan's original incarnation, 198f
  practical electronics work, 198
  principles, 195–196
  proceedings, 202
  schematic diagram, 195f
  Sheila Smith at controls, 201f
  technical problems, 199
  transmission microscope, 193
  visual acuity, 202
Scanning transmission electron microscopy (STEM), 221, 280–281
  aberrations, 287
    correction, 288
    CTF, 287
    gold particles, 290, 291f
    HR-TEM simulations, 288f
    using image metal nanoparticles, 290
    intensity profiles, 290f
    Scherzer defocus, 287–288
    simulation TEM micrographs calculation, 289f
    Z-contrast technique, 288–290
  bimetallic gold-palladium nanoparticles, 281f
  EDS spectrum detector, 286f
  HAADF-STEM, 285–286
  information transfer, in phase-contrast imaging, 281
  operational modes, 281, 282f
  optical arrangement, 282
  practical guide, 291
    electron beam sketches, 291–292, 292f
    electron beam trajectories, 293f
    focus conditions, 295f
    in-focus and underfocus, 293
    resolution, 291
    ronchigram, 293, 294f
    spot size and aperture, 292–293
  principles
    BF images, 283
    BF-CTEM, 283
    FEG, 282–283
    Fourier transform, 285
    high-resolution electron microscopy, 284
    operation modes, 283
    relativistic Dirac equation, 284–285
Scherzer condition, 287
Scientific Digital Imaging plc (SDI), 275
Self-adjoint operator, 70
  examples, 70–71
  properties, 70
Self-compositions, 88
SEM. *See* Scanning electron microscope; Structuring element map
Semi-atom, 82
Semi-graphitic carbon, 280
Semilattices, 80
Seminorm, 63
Set generator, 159–160

Shift-varying operators, 95–97
  adaptive morphology, 97–98
    adaptive neighborhoods, 97–98
    amoeba filters, 97
    geometry adaptive filters, 97
    SV operators, kernel and basis representation for, 98
  SEM, 95–96
    adjoint erosion, 96
    grey-level image functions, 96
Shockley partial dislocation (SPD), 312–314
Signal operators, 87
SM algorithm. *See* Sampling of mechanical model algorithm
SMI. *See* Strongly max-plus independent
Smith, Sheila Vernon, 201
  at Cambridge, 205–206
  Coach's prow, 207f
  Fairwell to crew, 206–207
  motorcycling, 205f
  time for music, 208–209
SOP. *See* Sum-of-products
Spatially varying operators (SV operators), 95
  adaptive median, 170–171
  erosions, 168
  image operators, 168
  increasing operator, 169
  planar set operators, 170
  polar coordinates, 170
  representations, 168
  SEM, 168–170
  SV kernel, 169
Spatially varying operators. *See* Shift-varying operators
SPD. *See* Shockley partial dislocation
Spectral representation
  eigenvalues, 77
  finite-dimensional vector spaces on, 76
  resolution of the identity, 77
Spruce wood fiber, 222f
Stack filters
  basis representation, 164–165
  grey-level output signal, 164
Standards Room, 192
State-of-the-art simulations, 321–325
STEM. *See* Scanning transmission electron microscopy
Stratified hierarchy, 16
Strongly max-plus independent (SMI), 143
Structuring element, 90
Structuring element map (SEM), 95–96
  adjoint erosion, 96
  grey-level image functions, 96
    adaptive kernel, 97
    adaptive window, 96
Structuring function. *See also* Structuring element map (SEM)
Subbasis, 177–178
Sublattice, 80
  sup-closed lattice, 80–81
  underlattice, 80
Sum-of-products (SOP), 161–162
Sup-★combination, 116–117
  Hamel basis, 117
  max-★ and min-★'combination, 117
Sup-closed lattice, 80–81
Sup-generators, 82
  atom, 82
  dual atom, 82
  dual semi-atoms, 82
  semi-atom, 82
Sup-semilattice, 80
Suphomomorphism, 88–89
Supremal convolution, 54, 95
Supremum norm, 66–67, 78
SV operators. *See* Spatially varying operators
Systolic approach, 14f
  classical version, 13
  using remarks, 13–14
  Revol's approach, 13
  seed's exclusion, 14

T

TEM. *See* Transmission electron microscope
Testing motorcycles, 190
Thorne, Ken, 208
Three-dimensional image segmentation (3D image segmentation), 9–11
Three-layer nanoparticle, 309, 310f
TI. *See* Translation-invariant
Tiplady's, 245
Topological isomorphism, 71

Transition metal chalcogenides, 319–320
Translation-invariant (TI), 50–52
  Bas (ψ), 157
  denoising, 157–158
  dual set operator, 147
  dual subbasis, 178
  flat area opening, 179, 179f
  Hamel basis, 158–159
  increasing operators
    adjoint erosions, 176
    adjunction, 175
    CWL, 174–175
    dual kernel, 176
    kernel, 175
    semi-atom, 175
    T-invariant dilation, 176
  increasing set operators, 146
  kernel property, 146
  minimal kernel elements, 147–148
  minimal subcollection, 149
  morphological basis, 159
  non-flat, 159
  non-increasing operators
    closed interval, 171
    hit-miss operations, 173–174
    inf-generating operator, 172
    inf-separable, 173
    kernel maximal closed intervals, 174
    sup-generating operator, 171–172
    sup-separable, 173
    TI set operator, 172
  nondegenerate operators, 146
  openings and closings, 177
  set dilation, 146
  set erosion operator, 146
  set operator bases, 150
  signal operator, 156–157
  subbasis, 177–178
  TI filters, 158
  u.s.c., 148–149
  weighted erosions and dilations, 157
Translations
  CWL signal space, 126
  horizontal and vertical translations, 125
  impulse, 125–126
  monoid of signal erosions, 125
  polar motions, 124
Transmission electron microscope (TEM), 193–194. *See also* Scanning electron microscope (SEM)
  aberrations, 287
    correction, 288
    CTF, 287
    gold particles, 290, 291f
    HR-TEM simulations, 288f
    using image metal nanoparticles, 290
    intensity profiles, 290f
    Scherzer defocus, 287–288
    simulation TEM micrographs calculation, 289f
    Z-contrast technique, 288–290
  bimetallic gold-palladium nanoparticles, 281f
  EDS spectrum detector, 286f
  HAADF-STEM, 285–286
  imaging, 280–281
  information transfer in phase-contrast imaging, 281
  operational modes, 281, 282f
  optical arrangement, 282
  practical guide, 291
    electron beam sketches, 291–292, 292f
    electron beam trajectories, 293f
    focus conditions, 295f
    in-focus and underfocus, 293
    resolution, 291
    ronchigram, 293, 294f
    spot size and aperture, 292–293
  principles
    BF images, 283
    BF-CTEM, 283
    FEG, 282–283
    Fourier transform, 285
    high-resolution electron microscopy, 284
    operation modes, 283
    relativistic Dirac equation, 284–285
Transmittance law, 40
Triumph Twin Motorbike, 205
Two-dimensional algorithm (2D algorithm), 15. *See also* Benzécri algorithm
  aggregation index, 18

- image grey scale, 18
- pseudo-code, 18f
- time-consuming part, 18

Two-dimensional Gaussian function (2D Gaussian function), 50

U

u.s.c. function. *See* Upper semi-continuous function
Ultrametrics, 16–17
Umbra function, 54
UNAM. *See* National Autonomous University of Mexico
Unconditional convergence, 63–64
Underlattice, 80
Uniform convergence, 66–67
Unitary operator, 71
Upper semi-continuous function (u.s.c. function), 86

V

Vectors. *See also* Linear spaces
Vertical translations (V-translations), 119–120
- function dilations, 120–121
- impulse response map, 122–123
- invariant function, 121
- linear superposition, 122
- nonlinear superposition principle, 122
- scalar erosions, 122

W

WBDF technique. *See* Weak-beam dark-field technique
Weak-beam dark-field technique (WBDF technique), 311–312
Weighted lattice (WL), 114–115
Window, adaptive, 96
Window transformations, 153
- application area, 156
- comparison, 154–155
- discrete set operator, 153
- finite union of erosions, 155
- grey-level image processing, 155–156
- hit-miss transformation, 155
- increasing window operator, 155
- locally defined operator, 154
- matched filter, 154
- one-to-one correspondence, 154
- shape collection, 153–154

WL. *See* Weighted lattice
WS_2 catalyst, 319–320
- nanowire catalysts, 326–334

X

X-ray detector, 285–286
X-ray photoelectron spectroscopy, 326–327

Y

Yarmouth, 205
Yorkshire, 217–219

Z

Z-contrast technique, 288–290
Zigzag nanoribbons, 321–325

This page intentionally left blank

Contents of Volumes 151-176

Volume 151[1]

Claas Bontus and Thomas Köhler, Reconstruction algorithms for computed tomography

Laurent Busin, Nicolas Vandenbroucke and Ludovic Macaire, Color spaces and image segmentation

Glenn R. Easley and Flavia Colonna, Generalized discrete Radon transforms and applications to image processing

Tomáš Radlička, Lie agebraic methods in charged particle optics

Valerie Randle, Recent developments in electron backscatter diffraction

Volume 152

Nina S.T. Hirata, Stack filters: from definition to design algorithms

Sameen Ahmed Khan, The Foldy–Wouthuysen transformation technique in optics

Saverio Morfu, Patrick Marquié, Brice Nofiélé and Dominique Ginhac, Nonlinear systems for image processing

Tohru Nitta, Complex-valued neural network and complex-valued backpropagation learning algorithm

Jérôme Bobin, Jean-Luc Starck, Y. Moudden and M.J. Fadili, Blind source separation: the sparsity revoloution

Ray L. Withers, "Disorder": structured diffuse scattering and local crystal chemistry

Volume 153

Aberration-corrected Electron Microscopy

Harald Rose, History of direct aberration correction

Maximilian Haider, Heiko Müller and Stephan Uhlemann, Present and future hexapole aberration correctors for high-resolution electron microscopy

Ondrej L. Krivanek, Niklas Dellby, Robert J. Kyse, Matthew F. Murfitt, Christopher S. Own and Zoltan S. Szilagyi, Advances in aberration-corrected scanning transmission electron microscopy and electron energy-loss spectroscopy

Philip E. Batson, First results using the Nion third-order scanning transmission electron microscope corrector

Andrew L. Bleloch, Scanning transmission electron microscopy and electron energy loss spectroscopy: mapping materials atom by atom

Florent Houdellier, Martin Hÿtch, Florian Hüe and Etienne Snoeck, Aberration correction with the SACTEM-Toulouse: from imaging to diffraction

Bernd Kabius and Harald Rose, Novel aberration correction concepts

Angus I. Kirkland, Peter D Nellist, Lan-yun Chang and Sarah J. Haigh, Aberration-corrected imaging in conventional transmission electron microscopy and scanning transmission electron microscopy

Stephen J Pennycook, M.F. Chisholm, A.R. Lupini, M. Varela, K. van Benthem, A.Y. Borisevich, M.P. Oxley, W. Luo and S.T. Pantelides, Materials applications of aberration-corrected scanning transmission electron microscopy

Nobuo Tanaka, Spherical aberration-corrected transmission electron microscopy for nanomaterials

Knut Urban, Lothar Houben, Chun-lin Jia, Markus Lentzen, Shao-bo Mi, Andreas Thust and Karsten Tillmann, Atomic-resolution aberration-corrected transmission electron microscopy

Yimei Zhu and Joe Wall, Aberration-corrected electron microscopes at Brookhaven National Laboratory

---

[1] Lists of the contents of volumes 100–149 are to be found in volume 150; the entire series can be searched on ScienceDirect.com

Volume 154

Henning F. Harmuth and Beate Meffert, Dirac's Difference Equation and the Physics of Finite Differences

Volume 155

Dmitry Greenfield and Mikhail Monastyrskiy, Selected Problems of Computational Charged Particle Optics

Volume 156

Vasileios Argyriou and Maria Petrou, Photometric stereo: an overview

Fred Brackx, Nele de Schepper and Frank Sommen, The Fourier transform in Clifford analysis

Niels de Jonge, Carbon nanotube electron sources for electron microscopes

Erasmo Recami and Michel Zamboni-Rached, Localized waves: a review

Volume 157

Mikhail I. Yavor, Optics of charged particle analyzers

Volume 158

Péter Dombi, Surface plasmon-enhanced photoemission and electron acceleration with ultrashort laser pulses

Brian J. Ford, Did physics matter to the pioneers of microscopy?

Jérôme Gilles, Image decomposition: theory, numerical schemes, and performance evaluation

Stina Svensson, The reverse fuzzy distance transform and its use when studying the shape of macromolecules from cryo-electron tomographic data

Marc van Droogenbroeck, Anchors of morphological operators and algebraic openings

Dong Yang, Shiva Kumar and Hao Wang, Temporal filtering technique using time lenses for optical transmission systems

Volume 159

Cold Field Emission and the Scanning Transmission Electron Microscope

Albert Victor Crewe, The work of Albert Victor Crewe on the scanning transmission electron microscope and related topics

Lyn W. Swanson and Gregory A. Schwind, A review of the cold-field electron cathode

Joseph S. Wall, Martha N. Simon and JamesF. Hainfeld, History of the STEM at Brookhaven National Laboratory

Hiromi Inada, Hiroshi Kakibayashi, Shigeto Isakozawa, Takahito Hashimoto, Toshie Yaguchi and Kuniyasu Nakamura, Hitachi's development of cold-field emission scanning transmission electron microscopes

Peter W. Hawkes, Two commercial STEMs: the Siemens ST100F and the AEI STEM-1

Ian R.M. Wardell and Peter E. Bovey, A history of Vacuum Generators' 100-kV STEM

H. Sebastian von Harrach, Development of the 300-kV Vacuum Generators STEM (1985–1996)

Bernard Jouffrey, On the high-voltage STEM project in Toulouse (MEBATH)

Andreas Engel, Scanning transmission electron microscopy: biological applications

Kenneth C.A. Smith, STEM at Cambridge University: reminiscences and reflections from the 1950s and 1960s

Volume 160

Zofia Baranczuk, Joachim Giesen, Klaus Simon and Peter Zolliker, Gamut mapping

Adrian N. Evans, Color area morphology scale-spaces

Ye Pu, Chia-lung Hsieh, Rachel Grange and Demetri Psaltis, Harmonic holography

Gerhard X. Ritter and Gonzalo Urcid, Lattice algebra approach to endmember determination in hyperspectral imagery

Reinhold Rüdenberg, Origin and background of the invention of the electron microscope

H. Gunther Rudenberg and Paul G. Rudenberg, Origin and background of the invention of the electron microscope: commentary and expanded notes on Memoir of Reinhold Rüdenberg

Volume 161

Marian Mankos, Vassil Spasov and Eric Munro, Principles of dual-beam low-energy electron microscopy

Jorge D. Mendiola-Santibañez, Iván R. Terol-Villalobos and Israel M. Santillán-Méndez, Determination of adequate parameters for connected morphological contrast mappings through morphological contrast measures

Ignacio Moreno and Carlos Ferreira, Fractional Fourier transforms and geometrical optics

Vladan Velisavlevic, Martin Vetterli, Baltasar Berufell-Lozano and Pier Luigi Dragotti, Sparse image representation by directionlets

Michael H.F. Wilkinson and Georgios K. Ouzounis, Advances in connectivity and connected attribute filters

Volume 162

Kiyotaka Asakura, Hironobu Niimi and Makoto Kato, Energy-filtered x-ray photoemission electron microscopy (EXPEEM)

Eireann C. Cosgriff, Peter D. Nellist, Adrian J. d'Alfonso, Scott D. Findlay, Gavin Behan, Peng Wang, Leslie J. Allen and Angus I. Kirkland, Image contrast in aberration-corrected scanning confocal electron microscopy

Christopher J. Edgcombe, New dimensions for field emission: effects of structure in the emitting surface

Archontis Giannakidis and Maria Petrou, Conductivity imaging and generalised Radon transform: a review

Olivier Losson, Ludovic Macaire and Yanqin Yang, Comparison of color demosaicing methods

Volume 163

Wolfgang S. Bacsa, Optical interference near surfaces and its application in subwavelength microscopy

Ruy H.A. Farias and Erasmo Recami, Introduction of a quantum of time ("chronon"), and its consequences for the electron in quantum and classical physics

Andrew Neice, Methods and limitations of subwavelength imaging

A.Sever Škapin and P. Ropret, Identification of historical pigments in wall layers by combination of optical and scanning electron microscopy coupled with energy-dispersive spectroscopy

Markus E. Testorf and Michael A. Fiddy, Superresolution imaging–revisited

Volume 164

Amos Bardea and Ron Naaman, Magneto-lithography: from the bottom-up route to high throughput

Román Castañeda, The optics of spatial coherence wavelets

Junchang Li, Yanmei Wu and Yan Li, Common diffraction integral calculation based on a fast Fourier transform algorithm

Marcel Teschke and Stefan Sinzinger, A generalized approach to describe the interference contrast and phase contrast method

Dokkyu Yi and Booyong Choi, Nonlinear partial differential equations for noise problems

Henning F. Harmuth, Harmuth corrigenda

Volume 165

Natalie Baddour, Two-dimensional Fourier transforms in polar coordinates

Neil V. Budko, Superluminal, subluminal, and negative velocities in free-space electromagnetic propagation

Rowan Leary and Rik Brydson, Chromatic aberration correction: the next step in electron microscopy

Michele Marrocco, Methods for vectorial analysis and imaging in high-resolution laser microscopy

Tomoya Sakai, Masaki Narita, Takuto Komazaki, Haruhiko Nishiguchi and Atsushi Imiya, Image hierarchy in Gaussian scale space

Yusuf Ziya Umul, The theory of the boundary diffraction wave

Emil Wolf, History and solution of the phase problem in the theory of structure determination of crystals from x-ray diffraction measurements

Volume 166

Valeriy Syrovoy, Theory of Intense Beams of Charged Particles

Volume 167

Emmanuel de Chambost, A history of Cameca (1954–2009)
Johan Debayle and Jean-Charles Pinoli, Theory and applications of general adaptive neighborhood image processing
Mohamed ben Haj Rhouma, Mohamed Ali Khabou and Lotfi Hermi, Shape recognition based on eigenvalues of the Laplacian
Nicolas Loménie and Georges Stamon, Point set analysis
Leonid P. Yaroslavsky, Image recovery from sparse samples, discrete sampling theorem, and sharply bounded band-limited discrete signals

Volume 168

Luca Geretti and Antonio Abramo, The synthesis of a stochastic artificial neural network application using a genetic algorithm approach
Michel Jourlin, Josselin Breugnot, Frédéric Itthirad, Mohammed Bouabdellah and Brigitte Closs, Logarithmic image processing for color images
Rainer A. Leitgeb, Current technologies for high-speed and functional imaging with optical coherence tomography
Sergej A. Nepijko and Gerd Schönhense, Analysis of optical systems, contrast depth, and measurement of electric and magnetic field distribution on the object's surface in mirror electron microscopy
Chad M. Parish, Multivariate statistics applications in scanning transmission electron microscopy
Hidetaka Sawada, Fumio Hosokawa, Takeo Sasaki, Toshikatsu Kaneyama, Yukihito Kondo and Kazutomo Suenaga, Aberration correctors developed under the Triple C project
Tobias Schulz, Martin Albrecht and Klaus Irmscher, Spatially resolved thermoluminescence in a scanning electron microscope

Volume 169

Erchan Aptoula and Sébastien Lefèvre, Morphological texture description of grayscale and color images
Vera Guarrera and Herwig Ott, Electron microscopy of ultracold gases
Konstantinos Konstantinidis, Ioannis Andreadis and Georgios Ch. Sirakoulis, Application of artificial intelligence to content-based image retrieval
Xingwei Yang, Daniel B. Szyld and Longin Jan Latecki, Diffusion on a tensor product graph for semi-supervised learning and interactive image segmentation
S.A. Nepijko and G. Schönhense, Electron holography for electric and magnetic field measurement and its application for nanophysics

Volume 170

A.S. Eggeman and P.A. Midgley, Precession electron diffraction
Ray Hill, John A. Notte and Larry Scipione, Scanning helium ion microscopy
Hone-Ene Hwang and Pin Han, Signal reconstruction algorithm based on a single intensity in the Fresnel domain
Kazuhisa Sato, Toyohiko J. Konno and Yoshihiko Hirotsu, Electron microscpy studies on magnetic $L1_0$ FePd nanoparticles
D.A. Zanin, H. Cabrera, L. de Pietro, M. Pikulski, M. Goldmann, U. Ramsperger, D. Pescia and John P. Xanthakis, Fundamental aspects of near-field emission scanning electron microcopy

Volume 171

Gregor Esser, Wolfgang Becken, Werner Müller, Peter Baumbach, Josep Arasa and Dietmar Uttenweiler, Derivation of the reflection equations for higher order aberrations of local wavefronts by oblique incidence
Lila Iznita Izhar and Maria Petrou, Thermal imaging in medicine
Jean-Michel Tualle, Derivation of the radiative transfer equation in a medium with a spatially varying refractive index: a review
Kamlesh Shrivas and Mitsutoshi Setou, Imaging mass spectrometry. Sample preparation, instrumentation and applications
Robert T. Thompson and Steven A. Cummer, Transformation optics

Tobias Klein, Egbert Buhr and Carl Georg Frase, TSEM – a review of scanning electron microscopy in transmission mode and its applications

Michel Jourlin, Maxime Carré, Josselin Breugnot and Mohamed Bouabdellah, Logarithmic image procesing: additive contrast, multiplicative contrast and associated metrics

Volume 172

Jay Theodore Cremer, Neutron and x-ray microscopy, Part 1

Volume 173

Jay Theodore Cremer, Neutron and x-ray microscopy, Part 2

Volume 174

Silicon-based Millimeter-wave Technology. Measurement, Modeling and Applications

M. Jamal Deen and Ognian Marinov, Measurement techniques and issues

Guennadi A. Kouzaev, M. Jamal Deen and Natalia K. Nikolova, Transmission lines and passive components

Mohamed H. Bakr and Mohamed H. Negm, Modeling and design of high-frequency structures using artificial neural networks and space mapping

Oana Moldovan, Antonio Lázaro, François Danneville, Rodrigo Picos, Bogdan Nae, Benjamin Iniguez and M. Jamal Deen, Nanoscale FETs

M. Daneshmand and R.R. Mansour, RF MEMS switches and switch matrices

Natalia K. Nikolova, Maryam Ravan and Reza K. Amineh, Substrate-integrated antennas on silicon

Volume 175

Jay Theodore Cremer, Small Angle Scatter with Correlation, Scatter and Intermediate Functions

Jay Theodore Cremer, Nuclear Scatter of Neutron Spin States

Christian Dwyer, Atomic-Resolution Core-Level Spectroscopy in the Scanning Transmission Electron Microscope

Partha Pratim Mondal and Alberto Diaspro, Point Spread Function Engineering for Super Resolution Single- Photon and Multi Photon Fluorescence Microscopy

P. Murray and S. Marshall, A Review of Recent Advances in the Hit-or-Miss Transform

Stephen J. Sangwine, Perspectives on Colour Images Processing by Linear Vector Methods using Projective Geometric Transformations

Volume 176

Katsushige Tsuno, Damaschin Ioanoviciu, Early History of Wien Filters

Damaschin Ioanoviciu, Katsushige Tsuno, Aberration Theory of the Wien Filter

Katsushige Tsuno, Damaschin Ioanoviciu, Wien Filter Instrumentation

Katsushige Tsuno, Damaschin Ioanoviciu, Simulation of Multipole Wien Filters

Damaschin Ioanoviciu, Katsushige Tsuno, Wien Filter Applications to Ions

Katsushige Tsuno, Damaschin Ioanoviciu, Application of Wien Filters to Electrons

This page intentionally left blank

COLOR PLATES

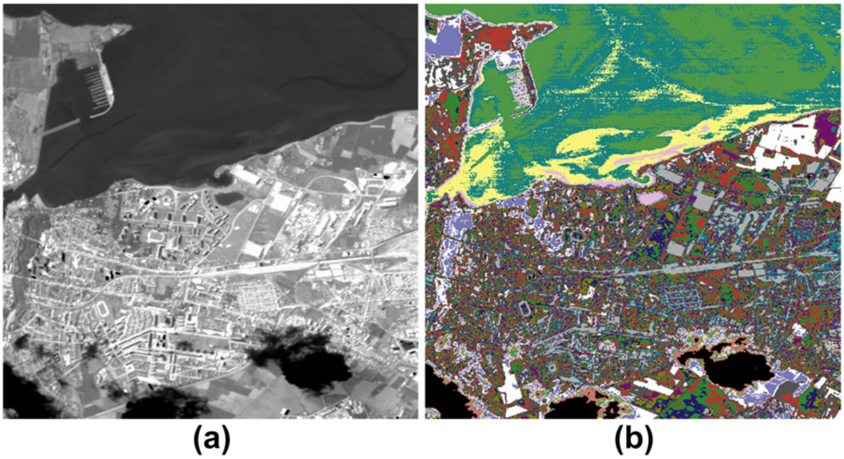

PLATE 2b (Figure 2b on page 6 of this volume)

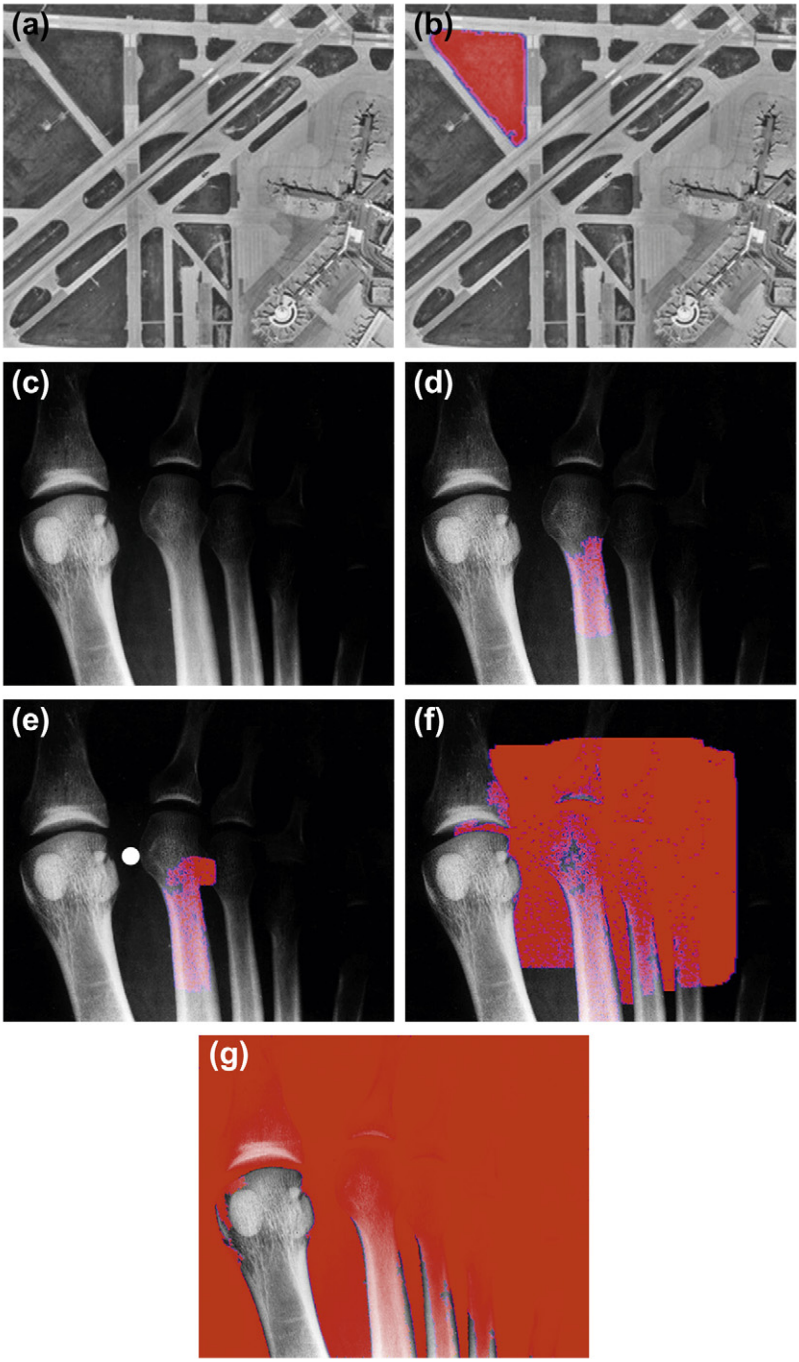

PLATE 3 (Figure 3 on page 10 of this volume)

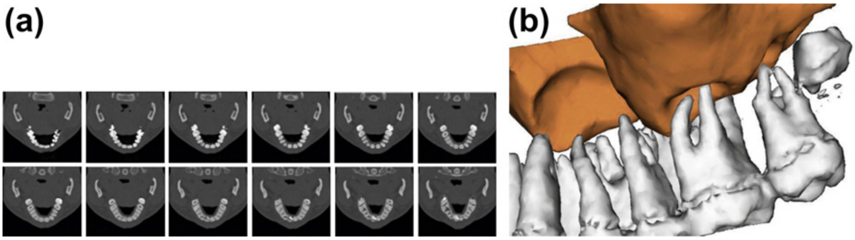

PLATE 4b (Figure 4b on page 12 of this volume)

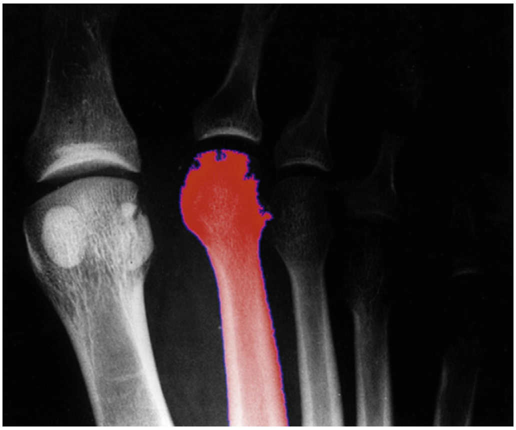

PLATE 5 (Figure 5 on page 12 of this volume)

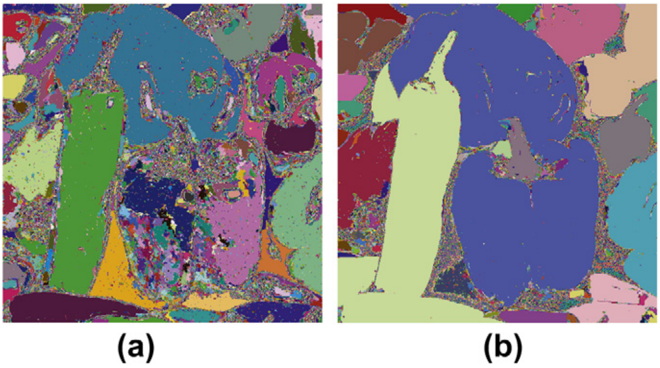

PLATE 15 (Figure 15 on page 22 of this volume)

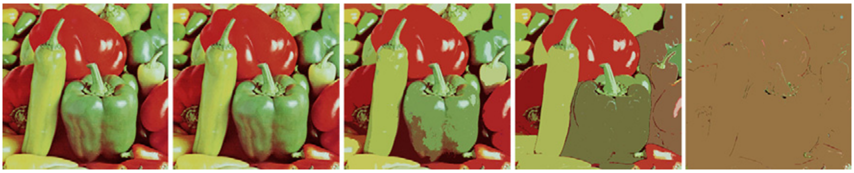

PLATE 16 (Figure 16 on page 22 of this volume)

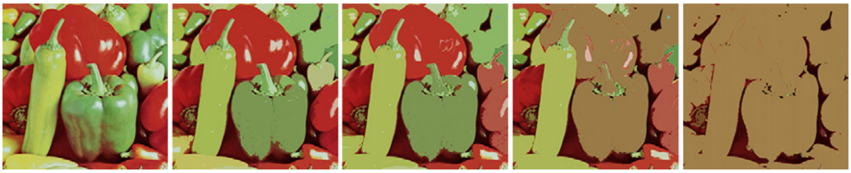

PLATE 17 (Figure 17 on page 23 of this volume)

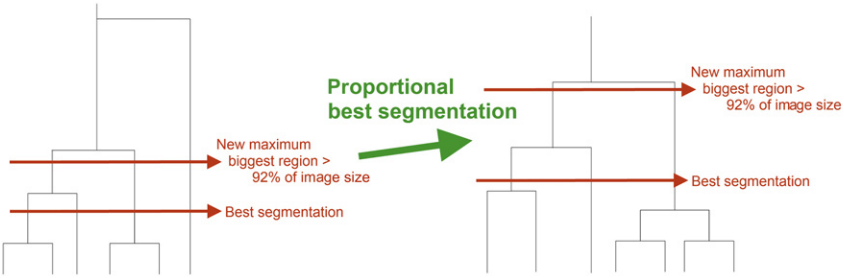
Proportional
best segmentation
New maximum
biggest region >
92% of image size
Best segmentation
New maximum
biggest region >
92% of image size
Best segmentation

PLATE 18 (Figure 18 on page 23 of this volume)

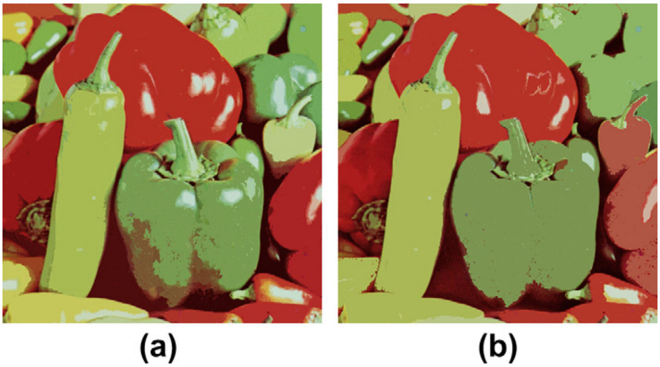

PLATE 19 (Figure 19 on page 23 of this volume)

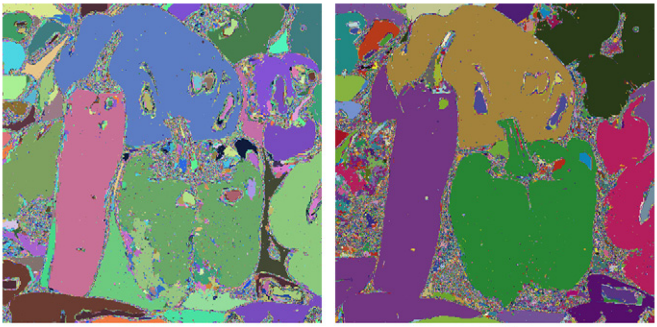

PLATE 20 (Figure 20 on page 24 of this volume)

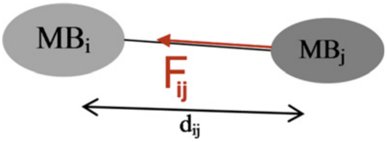
MB$_i$
MB$_j$
F$_{ij}$
d$_{ij}$

PLATE 22 (Figure 22 on page 25 of this volume)

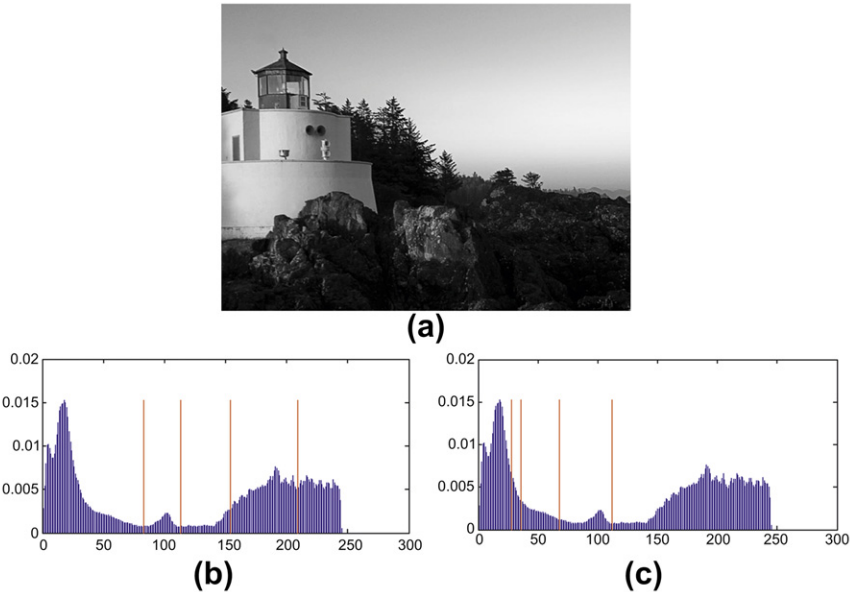

PLATE 27 (Figure 27 on page 34 of this volume)

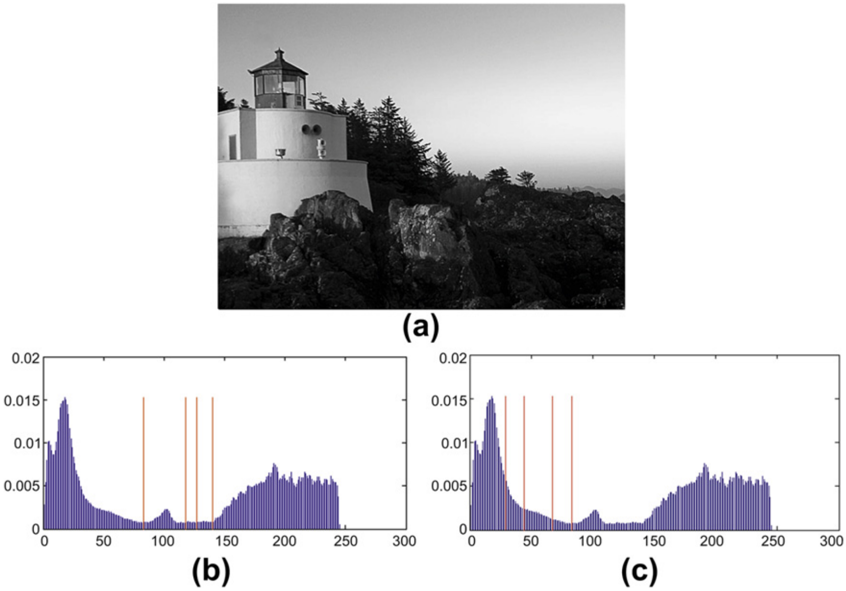

PLATE 29 (Figure 29 on page 36 of this volume)

PLATE 33 (Figure 33 on page 39 of this volume)

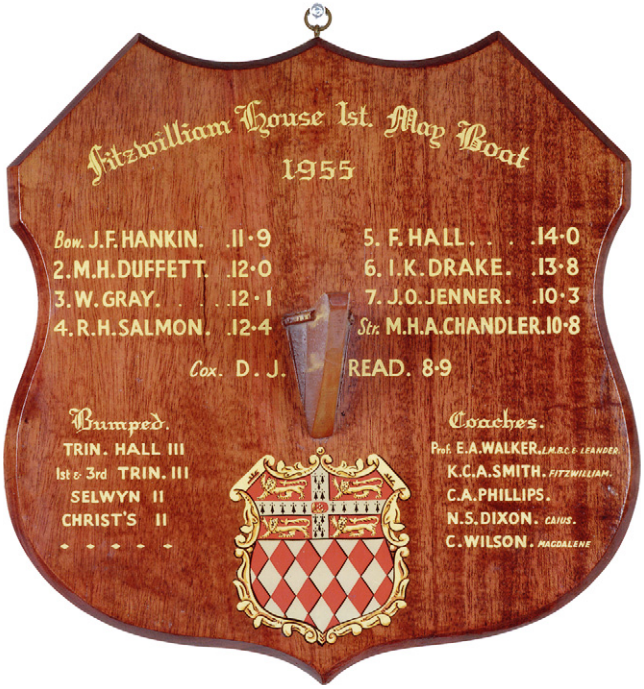
Fitzwilliam House 1st. May Boat
1955
Bow. J.F.HANKIN. .11·9
2.M.H.DUFFETT. .12·0
3.W.GRAY. . . . .12·1
4.R.H.SALMON. .12·4
5. F.HALL. . . .14·0
6. I.K.DRAKE. .13·8
7. J.O.JENNER. .10·3
Str. M.H.A.CHANDLER.10·8
Cox. D. J. READ. 8·9
Bumped.
TRIN. HALL III
1st & 3rd TRIN. III
SELWYN II
CHRIST'S II
Coaches.
Prof. E.A.WALKER. L.M.B.C. & LEANDER.
K.C.A.SMITH. FITZWILLIAM.
C.A.PHILLIPS.
N.S.DIXON. CAIUS.
C.WILSON. MAGDALENE

PLATE 6 (Figure 6 on page 207 of this volume)

PLATE 16 (Figure 16 on page 230 of this volume)

PLATE 18 (Figure 18 on page 233 of this volume)

PLATE 19 (Figure 19 on page 235 of this volume)

PLATE 20 (Figure 20 on page 235 of this volume)

PLATE 21 (Figure 21 on page 236 of this volume)

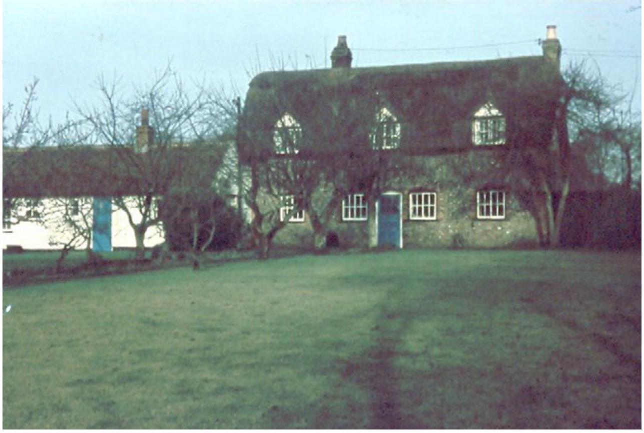

PLATE 24 (Figure 24 on page 252 of this volume)

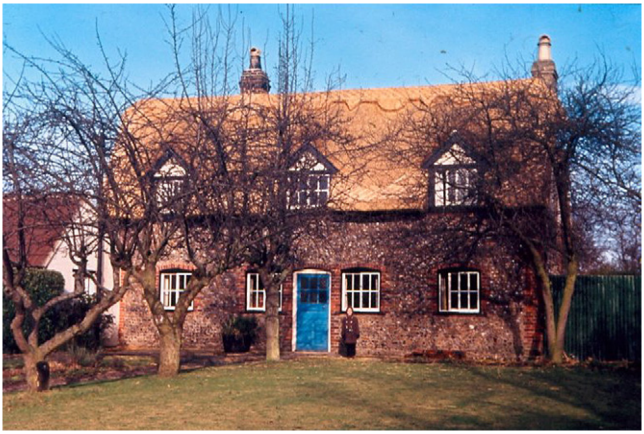

PLATE 25 (Figure 25 on page 252 of this volume)

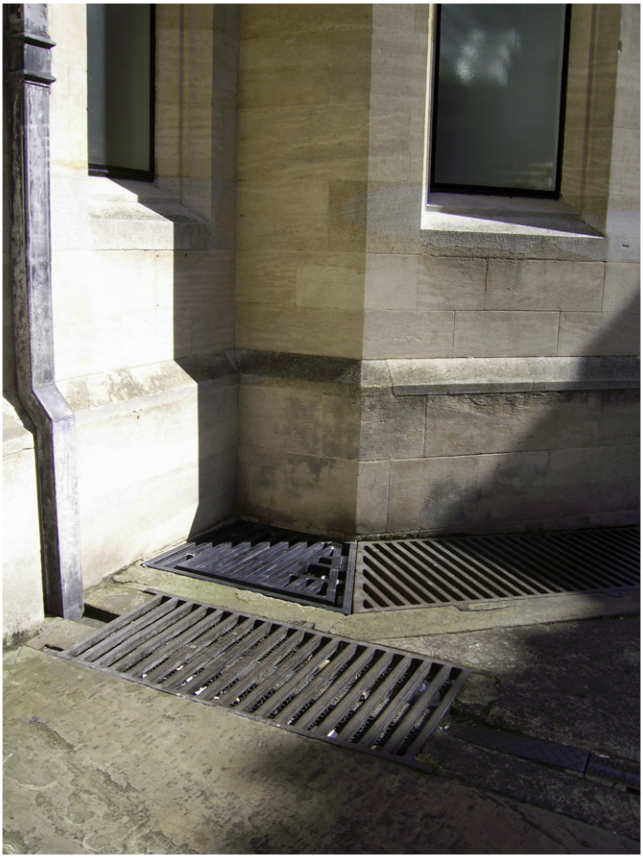

PLATE 28 (Figure 28 on page 256 of this volume)

PLATE 29 (Figure 29 on page 260 of this volume)

WILLIAM DU BOIS DUDDELL
MDCCCL
XXII
M.G. Gillick 1922
MCMXVII

PLATE 32 (Figure 32 on page 271 of this volume)

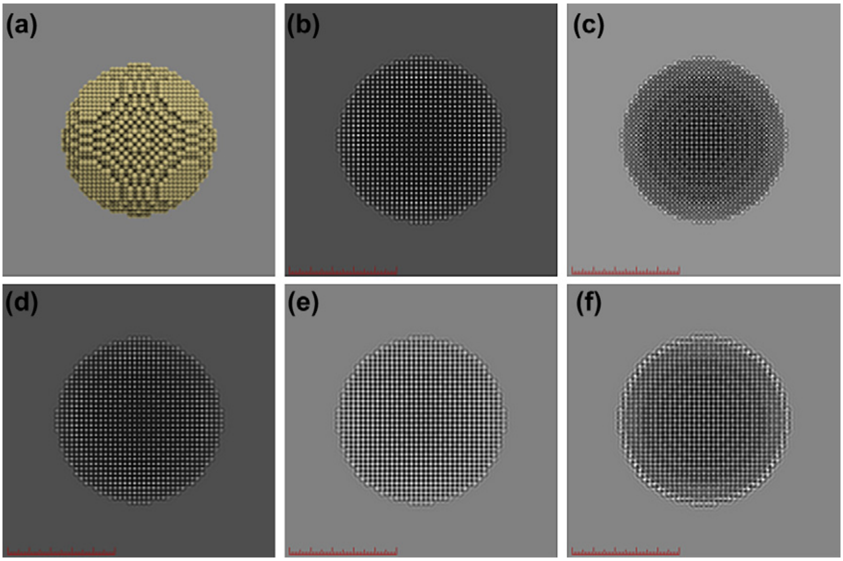

PLATE 4 (Figure 4 on page 288 of this volume)

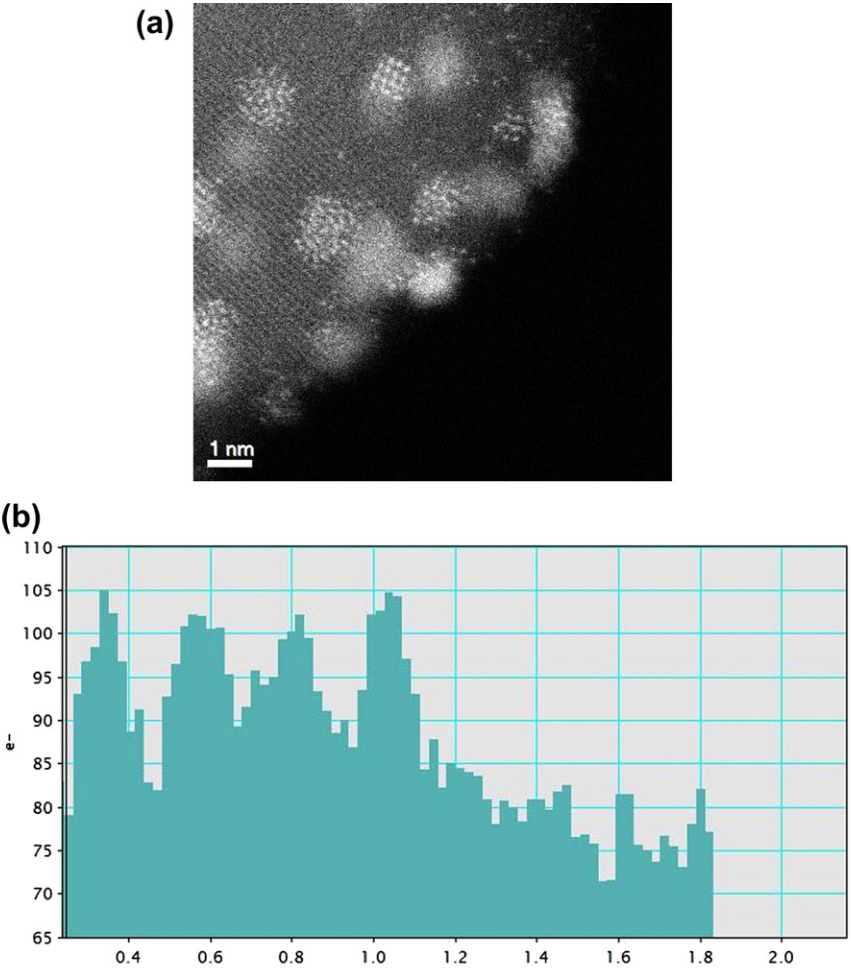

PLATE 12b (Figure 12b on page 296 of this volume)

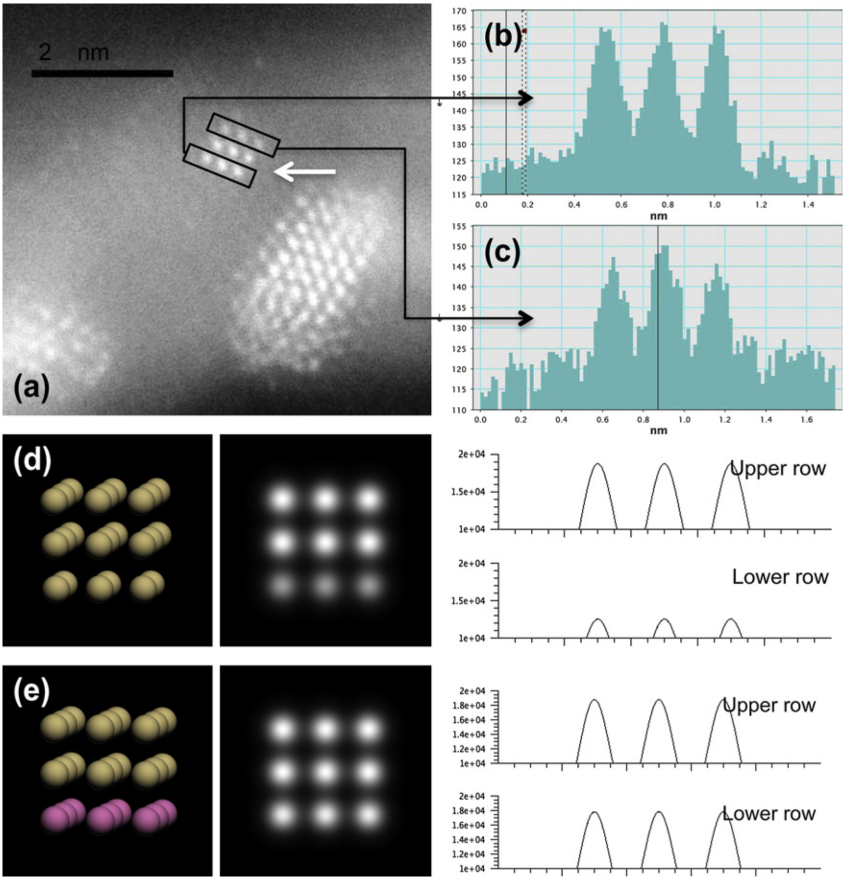

PLATE 14 (Figure 14 on page 298 of this volume)

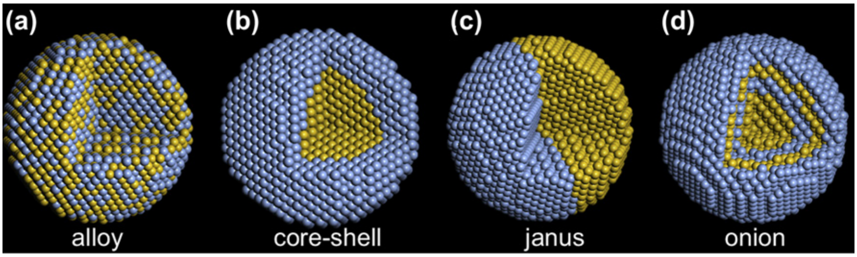

(a)
(b)
(c)
(d)
alloy
core-shell
janus
onion

PLATE 19 (Figure 19 on page 305 of this volume)

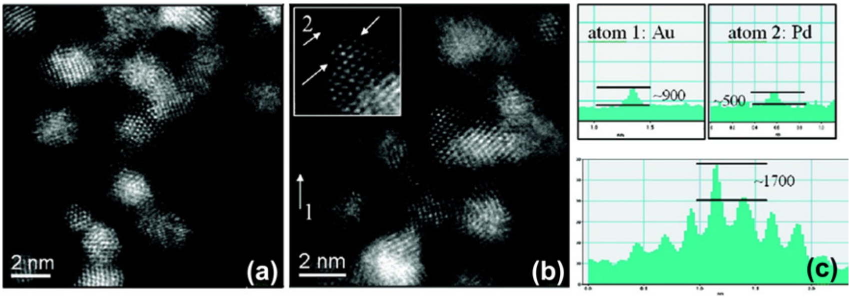

PLATE 20 (Figure 20 on page 306 of this volume)

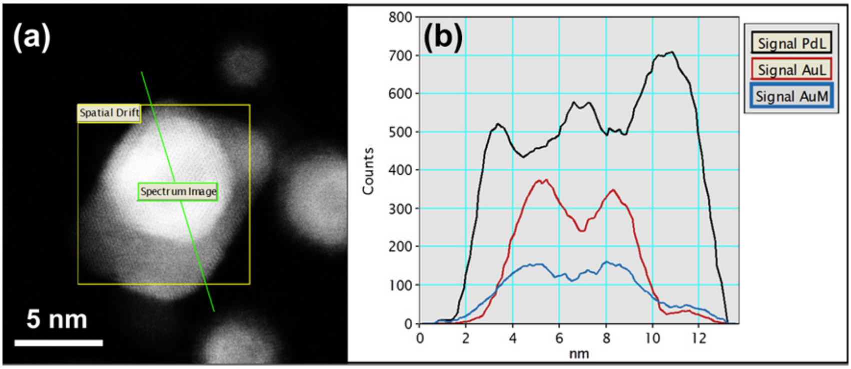

PLATE 22 (Figure 22 on page 308 of this volume)

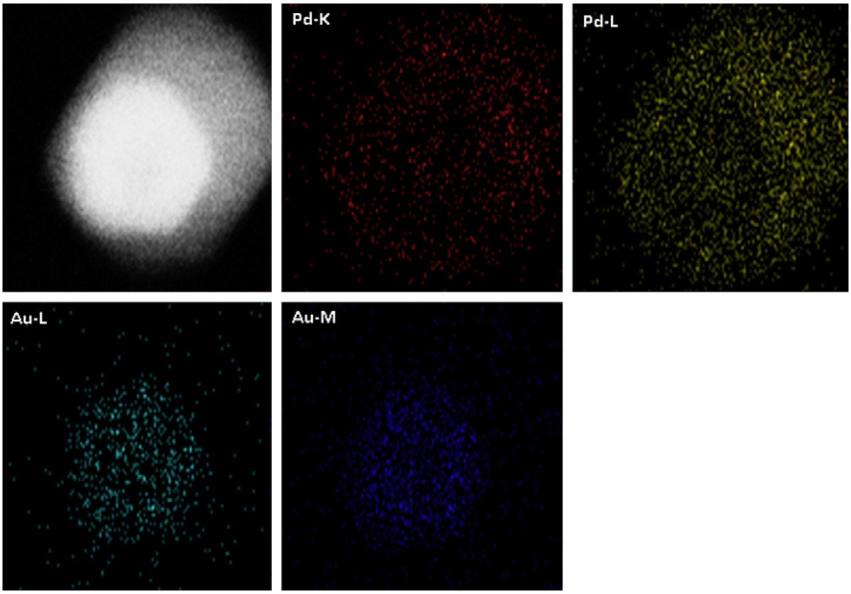
Pd-K
Pd-L
Au-L
Au-M

PLATE 23 (Figure 23 on page 309 of this volume)

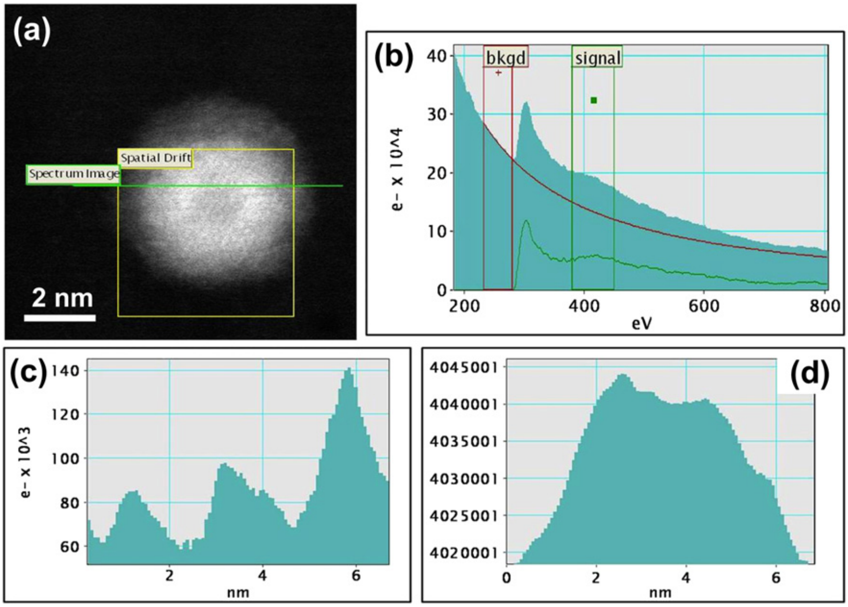

PLATE 24 (Figure 24 on page 310 of this volume)

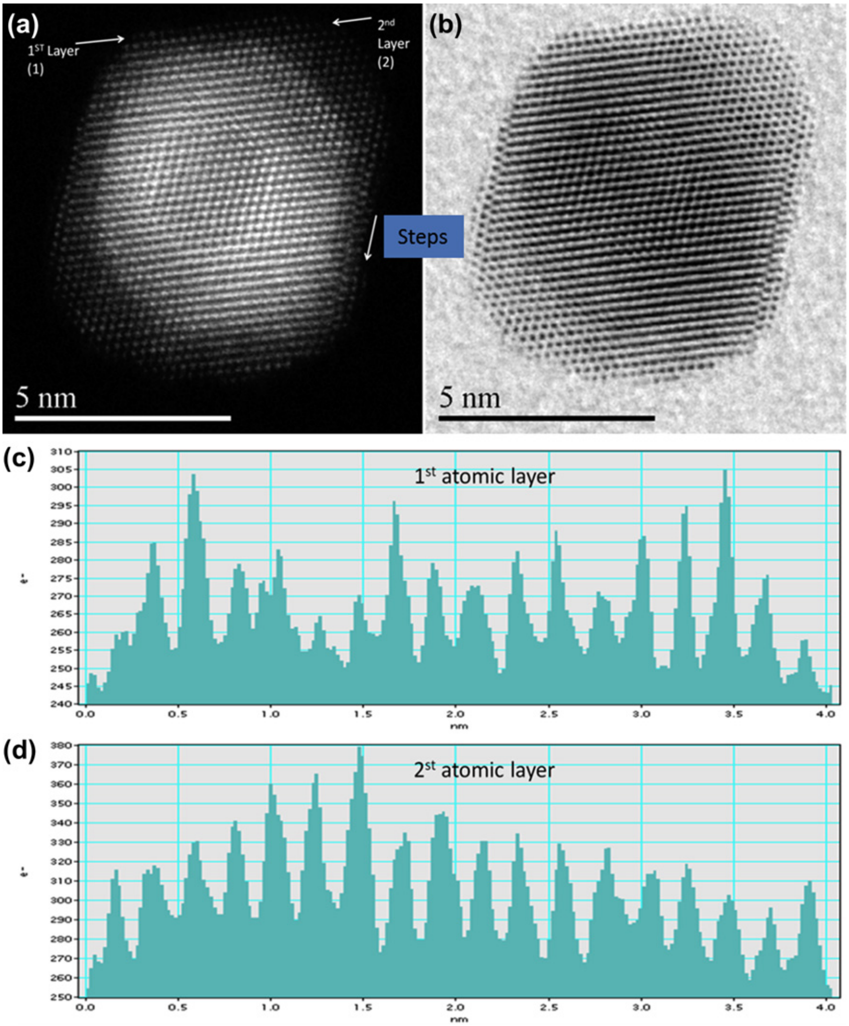
(a)
1ST Layer (1)
2nd Layer (2)
Steps
5 nm
(b)
5 nm
(c)
1st atomic layer
310 305 300 295 290 285 280 275 270 265 260 255 250 245 240
0.0 0.5 1.0 1.5 2.0 2.5 3.0 3.5 4.0
nm
(d)
2st atomic layer
380 370 360 350 340 330 320 310 300 290 280 270 260 250
0.0 0.5 1.0 1.5 2.0 2.5 3.0 3.5 4.0
nm

PLATE 28 (Figure 28 on page 313 of this volume)

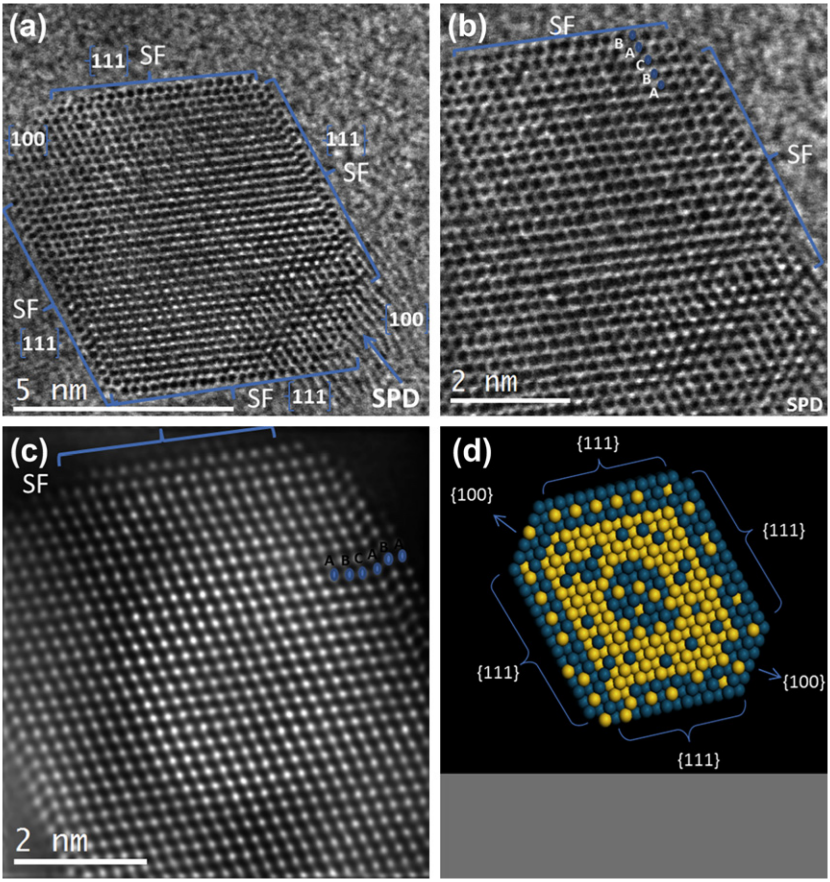
(a)
111
SF
100
111
SF
SF
111
100
5 nm
SF
111
SPD
(b)
SF
B
A
C
B
A
SF
2 nm
SPD
(c)
SF
A
B
C
A
B
A
2 nm
(d)
{111}
{100}
{111}
{111}
{100}
{111}

PLATE 29 (Figure 29 on page 314 of this volume)

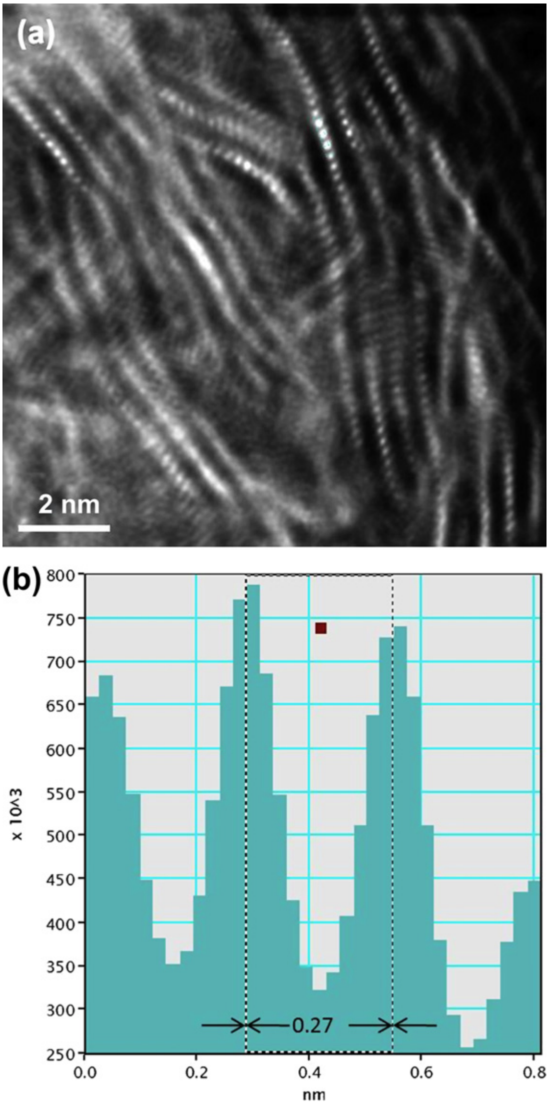

PLATE 34 (Figure 34 on page 322 of this volume)

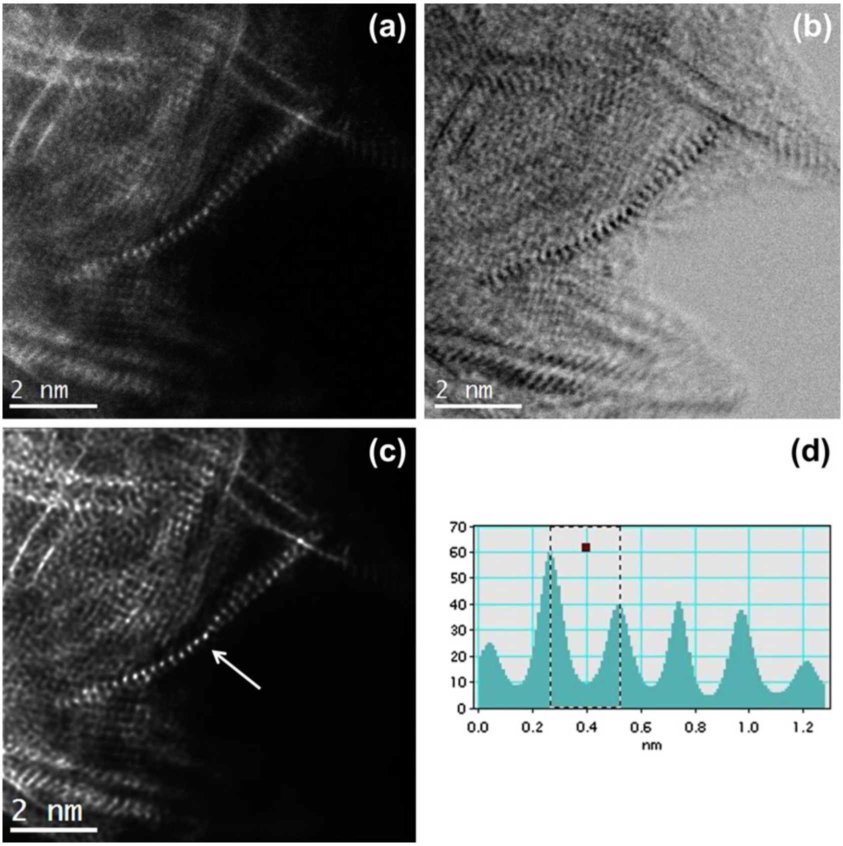

PLATE 35 (Figure 35 on page 323 of this volume)

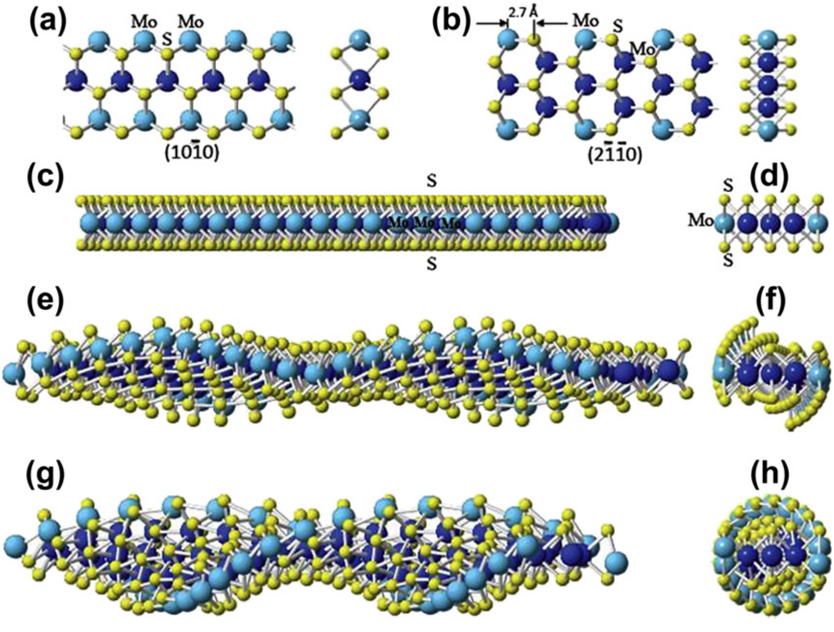
(a)
Mo
Mo
S
(10$\bar{1}$0)
(b)
2.7 Å
Mo
S
Mo
(2$\bar{1}\bar{1}$0)
(c)
S
Mo Mo Mo
S
(d)
S
Mo
S
(e)
(f)
(g)
(h)

PLATE 36 (Figure 36 on page 324 of this volume)

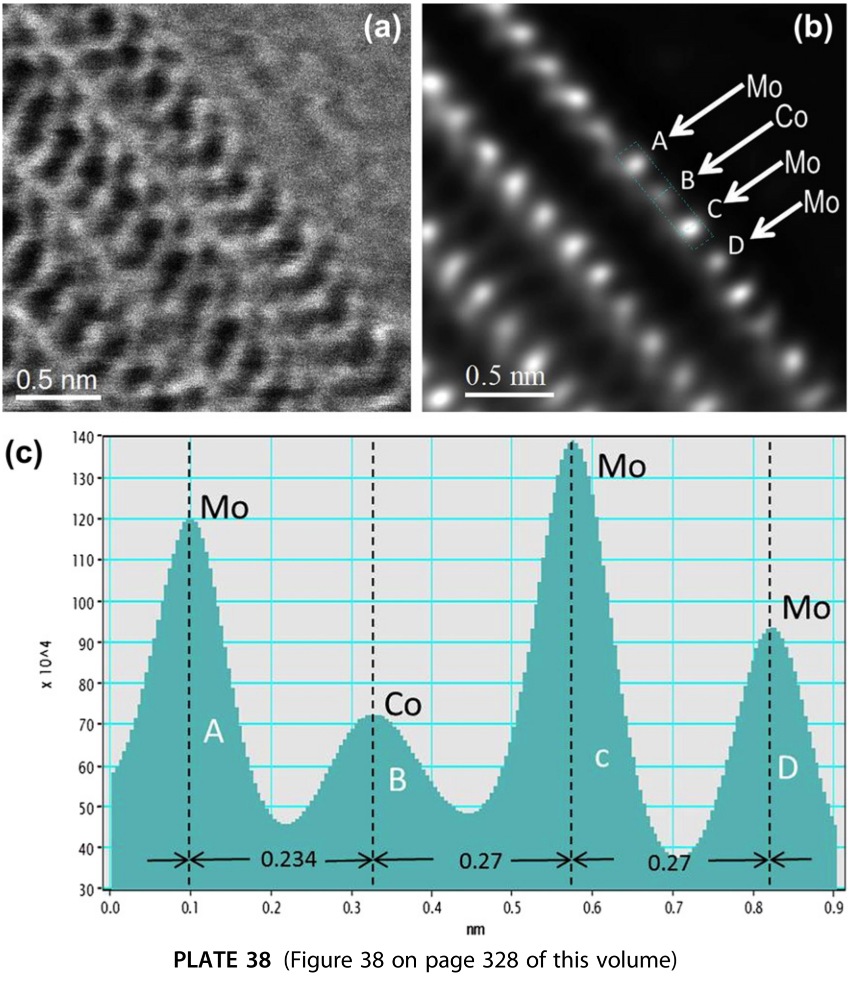
(a)
0.5 nm
(b)
Mo
A
Co
B
Mo
C
Mo
D
0.5 nm
(c)
140
130
120
110
100
90
80
70
60
50
40
30
x 10^4
Mo
Co
Mo
Mo
A
B
c
D
0.234
0.27
0.27
0.0
0.1
0.2
0.3
0.4
0.5
0.6
0.7
0.8
0.9
nm

PLATE 38 (Figure 38 on page 328 of this volume)

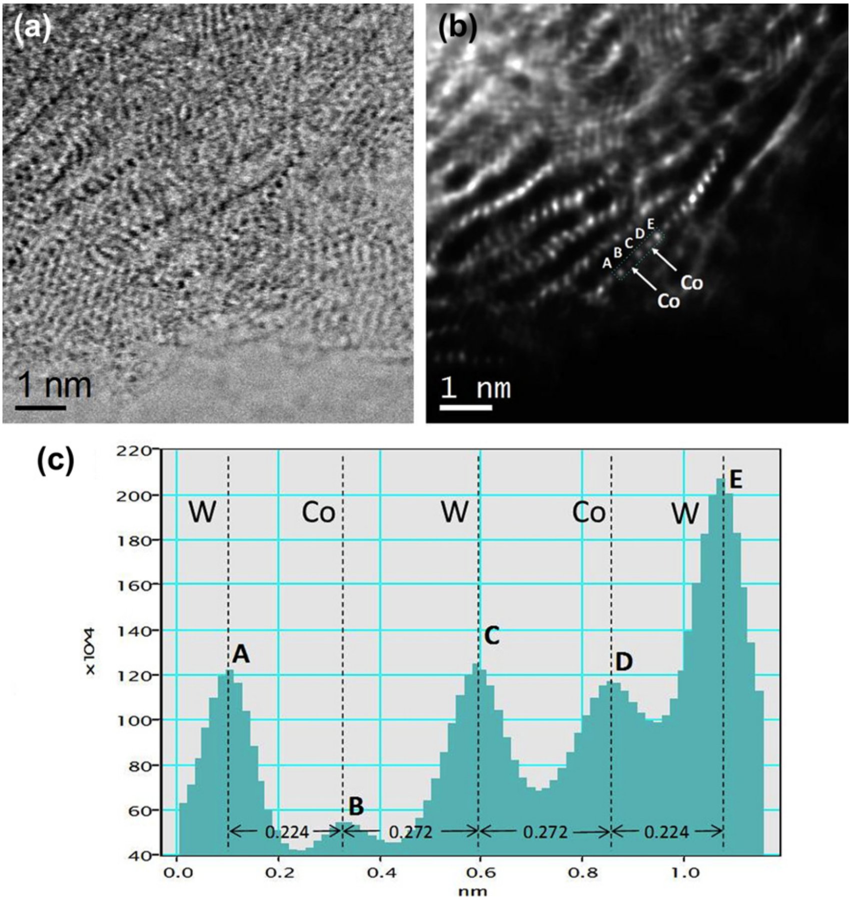

PLATE 40 (Figure 40 on page 330 of this volume)

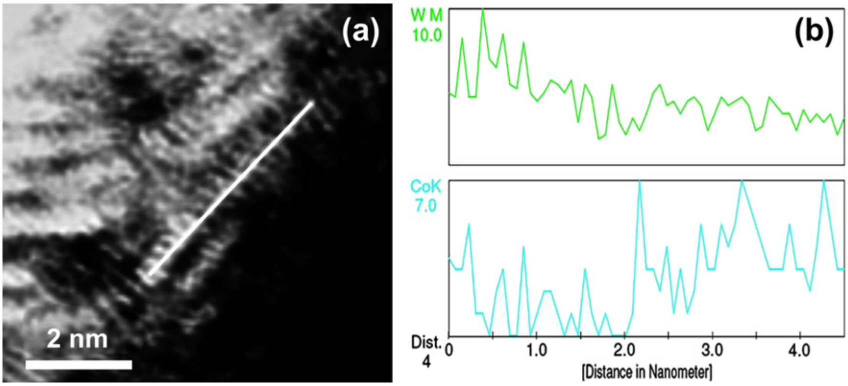

PLATE 41 (Figure 41 on page 331 of this volume)

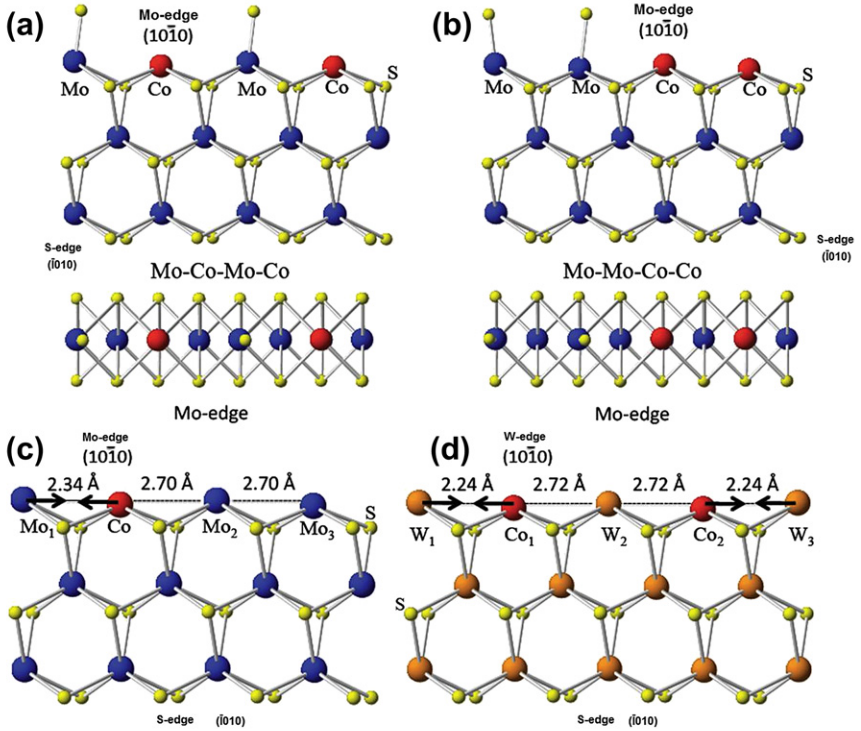
(a)
Mo-edge
(10$\bar{1}$0)
Mo
Co
Mo
Co
S
S-edge
($\bar{1}$010)
Mo-Co-Mo-Co
Mo-edge
(b)
Mo-edge
(10$\bar{1}$0)
Mo
Mo
Co
Co
S
S-edge
($\bar{1}$010)
Mo-Mo-Co-Co
Mo-edge
(c)
Mo-edge
(10$\bar{1}$0)
2.34 Å
2.70 Å
2.70 Å
Mo_1
Co
Mo_2
Mo_3
S
S-edge
($\bar{1}$010)
(d)
W-edge
(10$\bar{1}$0)
2.24 Å
2.72 Å
2.72 Å
2.24 Å
W_1
Co_1
W_2
Co_2
W_3
S
S-edge
($\bar{1}$010)

PLATE 42 (Figure 42 on page 332 of this volume)